CFD ANALYSES OF FLOW STRUCTURES IN AIR-INGRESS AND ROD BUNDLE PROBLEMS

A Dissertation

by

HONG-CHAN WEI

Submitted to the Office of Graduate Studies of
Texas A&M University
in partial fulfillment of the requirements for the degree of

DOCTOR OF PHILOSOPHY

Approved by:

Chair of Committee,	Yassin A. Hassan
Committee Members,	William H. Marlow
	Hamn-Ching Chen
	Kalyan Annamalai
Head of Department,	Yassin A. Hassan

December 2012

Major Subject: Nuclear Engineering

ABSTRACT

Two topics from nuclear engineering field are included in this dissertation. One study is the air-ingress phenomenon during a loss of coolant accident (LOCA) scenario, and the other is a 5-by-5 bundle assembly with a PWR design. The objectives were to investigate the Kelvin-Helmholtz instability of the gravity-driven stratified flows inside a coaxial pipe and the effects caused by two types of spacers at the downstream of the rod bundle. Richardson extrapolation was used for the grid independent study. The simulation results show good agreements with the experiments. Wavelet analysis and Proper Orthogonal Decomposition (POD) were used to study the flow behaviors and flow patterns.

For the air-ingress phenomenon, Brunt-Vaisala frequency, or buoyancy frequency, predicts a frequency of 2.34 Hz; this is confirmed by the dominant frequency of 2.4 Hz obtained from the wavelet analysis between times 1.2 s and 1.85 s. For the rod bundle study, the dominant frequency at the center of the subchannel was determined to be 2.4 Hz with a secondary dominant frequency of 4 Hz and a much minor frequency of 6 Hz. Generally, wavelet analysis has much better performance than POD, in the air-ingress phenomenon, for a strongly transient scenario; they are both appropriate for the rod bundle study. Based on this study, when the fluid pair in a real condition is used, the time which air intrudes into the reactor is predictable.

DEDICATION

To my mother, Pao-Hao Chen

ACKNOWLEDGEMENTS

I would like to thank Dr. Hassan, Dr. Annamalai, Dr. Chen, and Dr. Marlow because of their guidance of this study.

I would like to acknowledge Dr. Amini and Dr. Kang for their patience and assistance in this study. Texas A&M Supercomputer Facility is greatly appreciated for their services in accomplishing this research.

Many thanks also go to my friends, colleagues, the department faculty, and staff for making my time at Texas A&M University a great experience.

Finally, thanks to my parents for their endless love, support, and encouragement.

TABLE OF CONTENTS

Page

Page

Page

LIST OF FIGURES

Page

Page

Page

Page

Page

Page

LIST OF TABLES

Page

CHAPTER I

INTRODUCTION AND LITERATURE REVIEW

1.1 Motivation

Global energy demand has greatly increased in recent decades. Since burning fossil fuels emits remarkable amounts of greenhouse gases into the atmosphere, in order to prevent global warming from becoming worse and to reduce emissions of greenhouse gases, clean energy such as solar, wind, and tidal sources is the only solution. However, the efficiencies of these clean energy sources are insufficient to support growing electricity demand, and the costs of the clean energies are very expensive nowadays. Nuclear power plants seem to be the second best solution compared to other energies because of high efficiency, clean energy, and cheap costs. Nuclear reactor designs have been under development for many decades starting from the first generation the nuclear power plants, the research Light Water Reactors (LWRs). The second generation of the nuclear plants is then regarded as commercial LWRs. The pressurized water reactors (PWRs) and the boiling water reactors (BWRs) are the most common designs using the LWR concept. Since light water which is used as the coolant in LWRs is economical and easily obtained, the third and the third-plus generations are focused on improving the performance of the LWRs. The latest nuclear reactor designs, known as High Temperature Gas-cooled Reactors (HTGRs), are motivated by Next Generation Nuclear Plant (NGNP) that encourages researchers in materials and high efficiencies [0-3]. A new configuration that provides additionally passive cooling capability has been

designed to HTGRs. Although more cooling configurations and emergency cooling systems are implemented in nuclear plants, the maximum thermal power cannot reach the same level of the fossil plants. Unlike fossil fuel power plants, the maximum heat flux in the nuclear power plants (LWRs and HTGRs) is limited due to the restrictions of material properties, such as boiling point, melting point and thermal conductivity. An enormous heat flux that is even small compared to combustion power plants can fail the fuel cladding structure and cause fuel melting problems, which the releases fission gases [4]. When dealing with light water as the coolant, the large heat fluxes require higher order of attention for the design calculations in order to prevent critical heat flux (CHF) in BWRs or phase changing in PWRs. The CHF condition in BWR is coolant film dryout failure around the fuel rods. After the coolant dries, the zirconium cladding is overheated immediately and starts to react with light water. This accident will finally release hydrogen gas and induces hydrogen explosions because of high temperature and oxygen. Since HTGRs use gas as the coolants, phase changed is not considered. However, the failures in the fuel rods (fuel and cladding) are still restricted by the heat fluxes. In other words, the thermal hydraulics study of nuclear power plants is essential in developing new nuclear reactor concepts with alternative coolant, moderator, or fuel. In addition, the study of the simulations for the accident predictions helps understand the design concepts more.

1.2 Section 1 – Air Ingress Phenomenon

1.2.1 Background

Operating nuclear reactors require designs containing comprehensive cooling systems and external power supplies during accidents, such as emergency cavity cooling system and external electricity generators. The external power generators are used to maintain pumps working in the primary cooling loop during the reactor shutdown. Unlike fossil power plants, nuclear plants continuously release decay heat after the reactor shutdown with approximate 20% of the previously operating thermal power. Without the cooling pumps, the huge heat fluxes can dry water coolant out in a few minutes and cause CHF problem. Besides, absence of the coolant will result in severe accident, for example, fuel failure and hydrogen explosion. The safety issues are always most important in nuclear reactors where many possible and rarely possible failures are tested. Since HTGRs utilize graphite bricks as the moderators, to avoid oxygen contacting with graphite is compulsory in a very high temperature environment. Although HTGRs have no dryout conditions, any size of breaks can happen everywhere in the reactor vessels and easily destroy them. Oxygen that enters the reactor vessel through the break and contacts with graphite will cause burning and oxidation and further failure the reactors. Air or oxygen intrudes into the reactor through breaks is regarded as the air ingress phenomenon following the loss of coolant accident (LOCA). The behaviors of two different fluids are governed by gravity, so the phenomenon is also defined as gravity currents.

1.2.2 Previous research reviews

Gravity currents or otherwise named as density currents, consist of a heavy fluid intruding into a lighter fluid can be observed in large or small scales, such as ocean (salt and fresh water), atmosphere (warm and cold air), laboratory man-made experiments, and other fields. When heavy fluids encounter light fluids, complex turbulent phenomena occur. Many researchers have devoted efforts to understanding flow behaviors. Benjamin started a broad study of gravity currents and proposed a theoretical solution to the two-dimensional steady gravity current in inviscid fluids [5]. In 1972, Simpson introduced a correlation between the depth of the mean cross-section and the mean height of the advancing current through a broad range of Reynolds number from 300 to 10000 in horizontal channels [6]. Simpson and Britter observed Kelvin-Helmholtz instability and more mixing mechanism generated on the front of the current head in horizontal channels [7, 8]. Britter and Linden investigated that using larger slopes in the inclined horizontal channels affected the buoyancy force to greatly reduce the influence caused by frictional force and provided the same wave front head velocity [9]. Huppert and Simpson developed a relationship of the buoyancy force to the inertial force and viscous force for predicting the position of the wave front, which was a function of time with two-dimensional rectangles or axisymmetric disks [10]. Boussinesq approximation was widely studied for the fluid-pairs as water and brine or very low density ratios. Gibson investigated the interactions of shallow and deep ocean waves where the Boussinesq approximation can be adopted. Gibson observed that the estimations of dissipation rate and turbulent velocities might underestimate the space-

time averaging results in short vertical or short horizontal shear layers [11, 12]. Gardner and Crow studied air bubble motion in horizontal channels containing water, and Wilkinson included surface tension effects on bubble motion in the water horizontal ducts [13, 14]. Rottman and Simpson observed that there were two different phases of the gravity front due to the behavior of the front speed. The velocity of the gravity current is constant after instantaneous release of salt water in the fresh water channel as the initial phase. The velocity decreased as $t^{-1/3}$ when the flow becomes self-similar [15]. Webster investigated the density-driven stratified shear flow of a wind tunnel where the density gradient was created by heating air [16]. In atmosphere and ocean science, Lin *et al.* investigated the density stratified flow in a wind channel by heating the ambient air and cooling the lower boundary. Strong turbulence was discovered in the upper part of the rotor [17]. Based on the studies using two uniform streams of air in wind tunnels, Scotti, and Scotti *et al.* investigated different heated fluids for the Richardson number from 0.07 to 0.76 with the Reynolds number from 30 to 70 [18, 19]. Furthermore, Pao, Lange, and Dickey observed the decaying turbulence in stable stratified flows in horizontal and vertical channels [20-22]. Pao observed that the stratified flow far downstream had a layered structure which was created by the turbulent convection mixed by the mean flow [20]. Lange investigated fluctuation statistics of variety parameters in a horizontal channel and provided a decay law for density variance by approximately t^{-r} where r was from 0.3 to 0.6[21]. Dickey studied that the turbulent stratified flow with a short decay time in a wind tunnel for a non-dimensional time of 800 was similar to the case with the number of 275 [22]. Dickey observed that the decay

rate greatly decreased when the internal gravity waves replaced the turbulent fields [22]. Stillinger *et al.* studied density-driven stably stratified shear flows for the velocities from steady to 30 cm/s with the density ratio from 1.0 to 1.1 g/cm^3 and found a method to maintain arbitrary velocity profiles in each layer in time [23]. Boussinesq approximation is applicable for few percent of density ratios. In 1992, Grobelbauer *et al.* investigated the propagation of non-Boussinesq fronts with high density ratio from 1 to 20 in the exchange flow [24]. Grobelbauer *et al.* observed that the heavy- and light-fluid front velocities had limitations for the extrapolations to infinite depth and had good predictions from shallow-layer theory [24]. Barnea *et al.* concluded that the results of wide range of liquid viscosity showed similar amplification rate between the inviscid and the viscous Kelvin-Helmholtz analyses [25]. Barnea *et al.* observed that the fluid with a large viscosity was appropriate to be modeled with the inviscid Kelvin-Helmholtz theory whereas the low liquid viscosity had a significant discrepancy between the inviscid Kelvin-Helmholtz theory and the viscous Kelvin-Helmholtz theory [25]. Recently, Hartel *et al.* observed that the free-slip case showed results close to the classical Benjamin theory because the Boussinesq approximation was adopted for the slight density differences [26]. Shin *et al.* showed that dissipation rate was insignificant with high Reynolds numbers and developed a new theory for predicting gravity current velocity [27]. Gu and Guo studied Kelvin-Helmholtz criterion of the interfacial wave instability for horizontal and near horizontal pipes [28]. Gu and Guo observed that if the pipe inclination is greater than 0.4°, the critical heavy fluid height is insensitive to pipe inclination [28]. Gu and Guo developed a fitting curve of wave front speed versus wave

front height in pipe flow [28]. Stretch *et al.* observed the mixing efficiency in stratified flow where irreversible mixing mechanism appeared for turbulent kinetic energy converting back to potential energy. According to the simulation results obtained from DNS and rapid distortion theory, the mixing efficiency increased while initial Richardson numbers were small, but the efficiency remained constant for larger Richardson numbers [29]. Moreover, Lowe *et al.* developed a hydraulic model with two-layer fluids for the experiments with the density ratios from 0.61 to 1 [30]. Lowe *et al.* found that it was more unsteady for the heavy fluid than the light fluid at the interface [30]. Good agreements were obtained between experimental data and two-dimensional simulations researched by Birman *et al.* who observed that light currents followed Boussinesq level but heavy currents behaved as dissipative gravity currents [31].

1.2.3 Problem description

Unquestionably, the research of the gravity-driven stratified flows in nuclear engineering is necessary during a LOCA. NGNP organization encourages research in Very High Temperature Gas-cooled Reactors (VHGRs) under normal operation and accident scenarios such as air-ingress phenomena [32]. The air-ingress phenomenon is the accident scenario happening during a LOCA where the pressure inside the operating system decreases dramatically [33, 34]. Any size of the breaks that occurs at the co-axial pipe connecting the reactor vessel and the heat exchanger will result in a LOCA. The double ended guillotine break is considered as the worst condition happening in the accident even though this break is practically impossible. When the coolant fluid escapes from the reactor vessel and the pressure balances between the reactor vessel and the

surrounding environment, the air (with oxygen) in the cavity intruding into the reactor vessel, especially the support structure of the lower plenum which is made from graphite, will cause graphite oxidation and burning as described in Section 1.2.1 [33, 35]. In this problem, the focus is on the behavior of the stratified flows with different fluid pairs in the air-ingress process that is considered as gravity driven flows. Idaho National Laboratory (INL), under the U.S. Department of Energy (DOE), has organized many participants recently researching in this topic for VHTRs which has been researched since 1950s [0-3]. Oh, Kim, and many other participants studied air-ingress stratified flows in rectangular channels and pipes [33, 36, 37]. In this dissertation, the prototype designed from General Atomic was used to study gravity currents inside the coaxial pipe with assuming a double ended guillotine break [38]. STAR-CCM+ will be used to obtain simulation results which will be validated with experimental data done by Hartley [39].

1.3 Section 2 – OECD Bundle Benchmark Problem

1.3.1 Background

LWR concept that has been developed for more than 60 years is the most utilized design in the world because of highly dependable designs and easily obtainable materials. Also, many researchers continue advancing LWR designs in both PWRs and BWRs. PWR concepts have been designed widely in the world, for example, VVER in Russia, PWR and APWR in United States. The very high operating pressure is the main concept for water to prevent boiling that will break the primary cooling pump. In order to improve the efficiency of converting thermal power to electricity power, increasing

the heat transfer capability in PWRs becomes the main objective. From the thermo dynamics perspective, it is understandable that the higher temperature inlet of the heat exchanger improves efficiency. As a result, increasing coolant temperature in the core vessel e.g., water in PWR, provides improved thermal efficiency in nuclear reactors. Since PWRs use extremely large operating pressure inside the core vessels, water coolant can reach 300°C without the boiling mechanism that offers additional heat transfer capability. This defect can be compensated by increasing heat transfer capability. However, the fluid property cannot be changed much, so improving structure devices becomes beneficial. The concept can be achieved by attaching vanes on the spacers which will improve turbulent mixing mechanism to induce more turbulence and heat transfer capability. This dissertation uses the recent releases of the new designs to study the fluid behaviors. The MATiS-H benchmark problem (Measurement and Analysis of Turbulent Mixing in Subchannels-Horizontal) is sponsored by the OECD/NEA organization. The experimental test facility is established by the Korea Atomic Energy Research Institute (KAERI) [40].

1.3.2 Previous researches reviews

The development of PWRs is traceable back to the first generation of experimental nuclear power plants. The pressure drop problem is always an issue in any transportation phenomenon. DeStordeur tested several types of the spacers for the coolant flow paralleling to the bundle axis [41]. Melese *et al.* recommended different correlations to predict pressure drop for the fluids passing through the grid spacers in rod bundles [42]. In 1973, Rehme researched the prediction of the friction factor and

developed a pressure drop correlation for spacers [43-45]. Following Rehme, Yao et al. proposed a correlation of pressure drop for the spacer with and without vanes [46]. Schikorr *et al.* who used Rehme's correlations in the simulations obtained the results that showed very good agreements with the experimental data [47]. Among simulations performed by computational fluid dynamics (CFD) methodology, pressure drops, mixing mechanism, and heat transfer capability have been immensely researched recently. In vane design studies, Ikeda *et al.* and Navarro *et al.* performed 5X5 PWR rod bundles with mixing vane spacers [48, 49]. Lee and Choi studied flow downstream for different spacers [50]. Moreover, subchannel analyses have been researched for turbulent mixing phenomenon and secondary flows near fuel rods. Cui *et al.* and Kim *et al.* studied performance of vane shapes in subchannel and optimized mixing vane shapes [51-53]. According to previous researches, the additional vanes in different designs induce more turbulence and lead to different flow patterns, so the flow behaviors are interested.

1.3.3 Problem description

The OECD project is one of the benchmark problems of PWRs focusing on the spacer effect between the downstream and the upstream of the assembly. In this benchmark problem, the experimental facility is under the normal pressure and temperature with the isothermal boundary conditions, no buoyancy effect, and no gravity effect that is negligible in a long horizontal testing facility. The whole experimental facility is a 5-by-5 rod bundle structure with two flow stabilizers used to straighten and uniform flow inlet velocities conjugating a spacer followed by a 3-leg outlet device. PWRs have less mixing phenomenon and lower heat transfer rate because the boiling

process causing phase-change and turbulence can induce greater heat transfer capability and enhance turbulent mixing mechanisms. In order to improve heat removal ability in the primary cooling loops of PWRs, the spacers with vanes are implemented in the bundles not only to increase heat removal rate but also to stabilize the fuel rods and the assembly [54]. Velocity profiles and vortex contours at few different downstream cross sections for subchannel analyses between rod bundles are investigated because flow is highly disturbed at the downstream, especially close to the spacer. Another focus is on the different flow patterns and the invisible vortices which provide mixing mechanism using various vane designs. Two different vane designs, split and swirl, provided by the OECD/NEA organization are used to study the fluid behaviors. The experimental data that are also obtained from the OECD/NEA organization will be compared with simulations.

1.4 Objective

This dissertation includes two sections in nuclear engineering field. One study is the air-ingress phenomenon during a LOCA scenario held by NEUP organization under the U.S. DOE, and the other study is a 5-by-5 bundle assembly project under a design of PWRs delivered by the OECD/NEA organization.

The air-ingress problem following a LOCA has been regarded as a potential severe accident in HTGRs [33]. The concentrations of oxygen gas in all scenarios with different the break sizes directly affect the graphite oxidation conditions. Even though the double ended guillotine break is practically impossible, it is assumed as the most disastrous condition because of its large break size. In order to predict and validate this

shortly transient scenario, therefore, the gravity-driven stratified flow following an air-ingress phenomenon is investigated in this research. Helium as the coolant in HTGRs and air surrounding the environment are two fluids in the real accident. A fluid similarity scaling is provided to mimic the real accident because helium and air is difficult to dye. Most of the previous research studies are done on rectangular channels, ducts, or pipes containing salt and fresh water. The study of how two fluids behave in coaxial pipes becomes a new motivation in this dissertation since the research in coaxial pipe is a new study for gravity-driven stratified flows. A liquid-liquid scenario and a gas-gas case will be simulated in this research.

The focus of the OECD bundle exercise is on the flow behavior using different vane designs. Since PWRs utilize very large operating pressure to maintain water in single-phase (liquid), heat transfer capability is less than BWRs where boiling mechanism provides high heat transfer rates. Improving turbulent mixing mechanism can help increase heat transfer capability, so studying spacer effects becomes the main interesting part in the PWR rod bundle. Velocity profiles and vortices contours can help very much in analyzing turbulent performance. Water is the material used in this project for the hydrodynamics study without heat sources. The gravity effects are neglected in the testing facility because of the long horizontal geometry. The objective of this rod bundle problem is to investigate the flow patterns at the downstream.

Currently, CFD methodology has become a major tool for studying and predicting fluid hydrodynamics. CFD will be used to model all scenarios because of the conveniently obtaining results, such as visual graphic interface and various packages of

turbulent modeling. Different commercial CFD codes e.g., STAR-CCM+ and ANSYS CFX, will be used to obtain simulation results for comparing and validating with experimental data [55-57]. MATLAB were used for the post analyses [58]. Besides, the mesh size sensitivity studies are performed to obtain numerical convergence with error analysis. Moreover, wavelet analysis and proper orthogonal decomposition (POD) were applied to characterize turbulence [59-62].

CHAPTER II

DESCRIPTION OF EXPERIMENTAL FACILITY

2.1 Section 1 – Air Ingress Phenomenon

2.1.1 Scaling process of the experiments

The GT-MHR design shown in Figure 1 includes the prismatic core with a lower plenum, the co-annular duct, and the heat exchanger and the turbine. As the arrows presented in Figure 1, hot helium from the reactor core goes through the hot duct of the coaxial pipes (inner pipe) and exchanges heat in the turbine and the electricity generator. Then, cold helium compressed in the compressor moves back to the core vessel via the outer pipe as the coolant that removes heat from the fuels and finally moves toward the heat exchanger as a close loop. Any break that occurs in the pipe or the reactor vessel will cause a loss of coolant accident (LOCA) and will eventually result in the air ingress phenomenon. In order to validate that the scale down to laboratory had the same VHTR conditions during a LOCA, the same fluid similarity between the real condition and the laboratory facility was performed [39]. Moreover, the scaling process was performed to represent the experiments for studying the gravity-driven stratified flow phenomenon and to mimic the real condition during the accident in the VHTRs. It is clear that the air-ingress phenomenon under prototype conditions has the following parameters: Fr=0.33 and Ri=0.68 [39]. The Froude number and the Richardson number are two common dimensionless parameters for studying stratified flows.

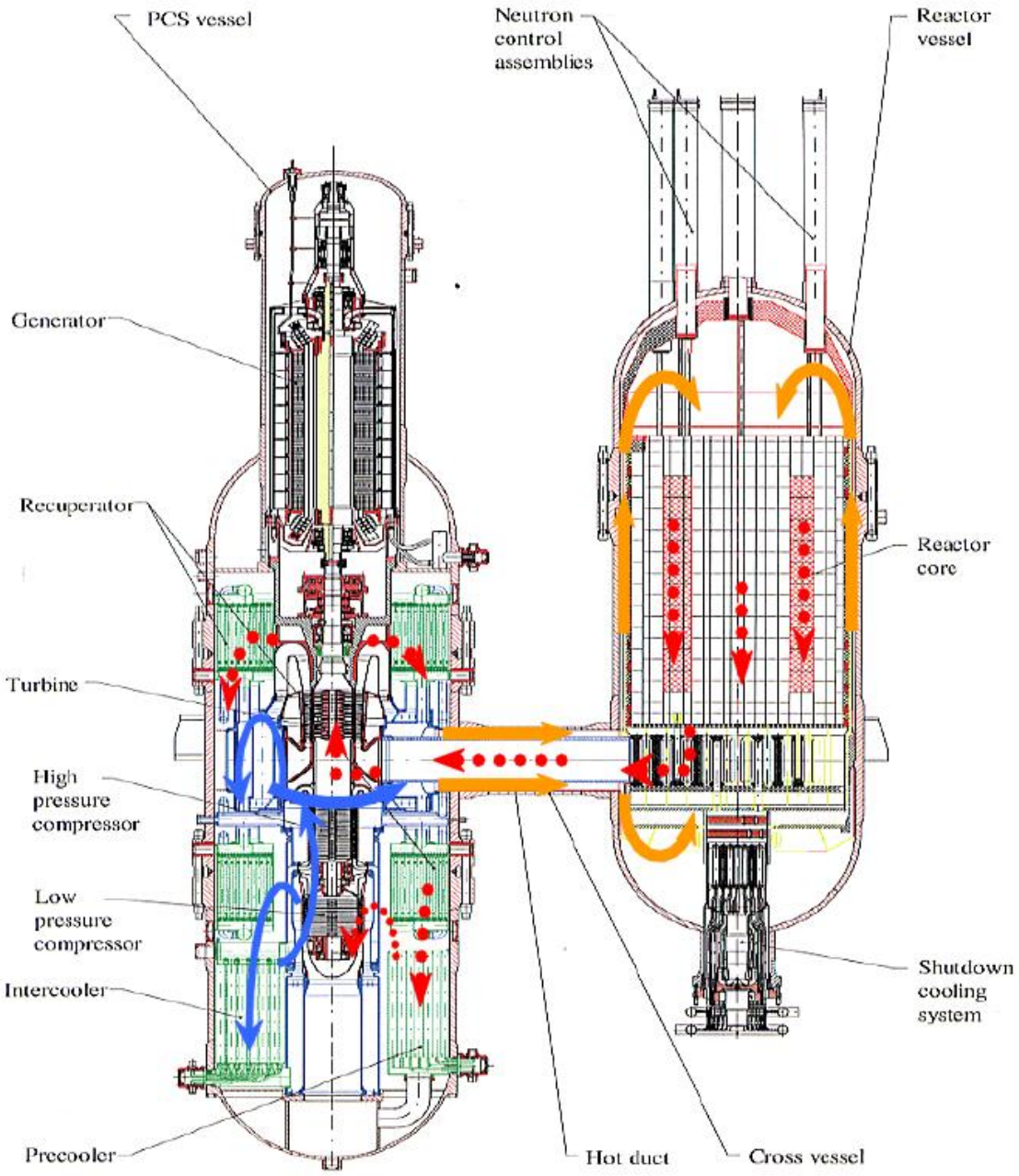

Figure 1. Design configuration of the GT-MHR [38].

The Froude number is defined as the ratio of inertial force to gravitational force, and the Richardson number is the ratio of buoyancy force to inertial force. Boussinesq approximation assumes that the inertia difference is unimportant and the gravity effects are strong to let specific weight be significant between two fluids; as a result, the Boussinesq approximation is applied to the Froude number and Richardson number to study density difference of the fluid pairs. In this study, the Froude number and Richardson number were calculated from Eq. 2-1 and Eq. 2-2.

$$Fr = \frac{inertial\ forces}{gravitational\ forces} = \frac{U}{\sqrt{gh}} \quad \text{(Eq. 2-1)}$$

$$Ri = \frac{buoyancy\ forces}{inertial\ forces} = \frac{g'h}{U^2} = \frac{g\frac{\rho_{heavy}-\rho_{light}}{\rho_{average}}h}{U^2} \quad \text{(Eq. 2-2)}$$

where g is gravity, g' is reduced gravity, h is wave front height, and U is wave front speed. The Benjamin theory was used for the gravity current front velocity in the scaling analysis [5].

Table 1 lists the comparisons of the fluid similarity in the real and the experimental conditions. In this study, two fluid pairs, helium-SF_6 and water-brine pairs, are used for the experiments. Helium and SF_6 were chosen for this problem because the dimensionless numbers were the same as those occurring in the actual air ingress scenario of the reactor (helium and air). As a result, using the fluid pairs (helium and SF_6) in the experiment and the simulation will allow the gravity current front velocity to be the same as that in the real air ingress condition in the reactor. Additionally, SF_6 is easier to dye than air, so SF_6 was used in the experiment. Although the dimensionless number of water and brine pairs does not match the real condition, the liquid-liquid case

is still utilized because of the good visualization. Moreover, the water-brine case is much easier to capture important phenomena than the gas-gas scenario because it is more difficult to dye gases.

Table 1. Lists of fluid pairs used for the reactor similarity.

Fluid Pair	Froude Number	Richardson Number	Density Ratio
Helium-Air	0.33	0.68	0.14
Water-Brine	0.43	4.89	0.88
Helium-SF_6	0.33	0.68	0.14

2.1.2 Geometry and dimensions of the experimental facility

The experimental prototype established at Texas A&M University is a simplified module with an approximate 1:20 scale of the original GT-MHR design [38]. The prototype is consisted of two identical fluid tanks, a knife gate valve, and a coaxial connecting pipe. The dimensions of the experimental facility are shown in Figure 2. It must be mentioned that the diameters of the inner and the outer pipes are 0.066 m and 0.1 m, respectively. Two different lengths of the co-axial pipe, 0.38m and 1m, are used to characterize the pipe break locations in order to study the effects of the break locations. Fluids are filled from the top of the tanks, and the moving valve will be moved in the direction toward the reader in the experiments.

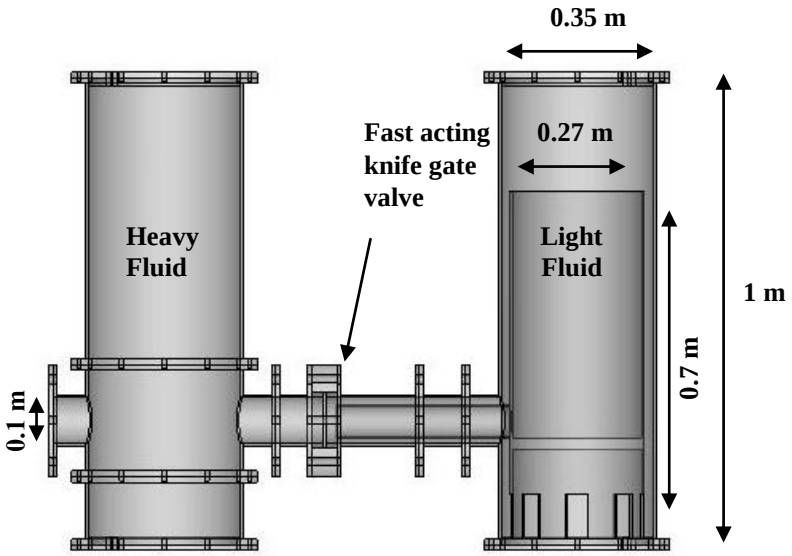

Figure 2. Laboratory experimental facility at Texas A&M University.

2.1.3 Initial and boundary conditions in the experiments

Two fluids were filled to the tanks and perfectly separated by the valve located at the connecting pipe as the initial condition. For the boundary condition, the two fluids were measured at the same pressure and at steady state. After the fluids reached equilibrium, the valve was suddenly open. During the experiments, the total physical time to open the valve was 0.534s in the direction toward the reader (Figure 2). Since the valve moved within an extremely short time, it was assumed that the valve moved with a constant speed for the simulation. In the water-brine case, the brine solution is dyed for visualizations. For the helum-SF_6 scenario, it is difficult to dye SF_6, so the particles that were applied to SF_6 were irradiated by the laser lights. To observe the air ingress phenomenon, 2 (short-pipe) or 3 (long-pipe) high speed cameras were used to capture transient flow behaviors.

2.2 Section 2 – OECD Bundle Benchmark Problem

2.2.1 Geometry and dimensions of the experimental facility

The rod bundle project is released by the OECD/NEA organization. The geometry of the experimental facility established by the KAERI is demonstrated in Figure 3[40]. The main flow area is composed of an approximate 5 meters long and 170-by-170 mm square duct. The square duct contains 25 rods with 33.12 mm rod pitch and 25.4 mm outer diameter which is 9.6 times larger than the fuel rod size in real PWR designs. As a result, the hydraulic diameter of the cross section is 24.27 mm. A 3-leg outlet and an inlet with 4 inches diameter are connected to the main flow domain at the end and the beginning of the facility, respectively. Two flow straighteners and one

testing spacer are implemented in the facility in order to obtain a uniform velocity profile. In other words, the straighteners are implemented to generate approximately irrotational flows that are of advantage to simplify this study. Therefore, the vorticity effects due to spacers are characterized in the downstream. Between the second straightener and the testing spacer, the upstream distance (S) is set to 100 hydraulic diameters to allow the flow to have a fully developed flow profile. As a result, the only factor that influences the flow behaviors at the downstream is simplified as the testing spacers. Figure 4 shows the testing spacers used in the experiments. The same dimensions of the devices are used in the simulations. Figure 4 shows the split-type and the swirl-type test spacers utilized in the rod bundle experiments. The significant difference of the vane designs affects flow features at the subchannel regions. The CAD geometry files are also employed for the simulations to mesh conveniently.

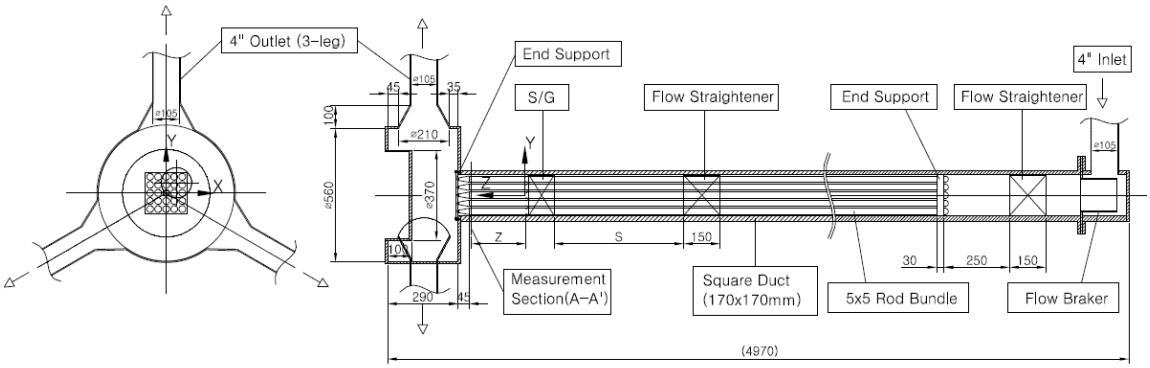

Figure 3. The cross section and dimensions of the experimental facility in OECD/NEA benchmark problem where S is $100D_h$ and Z is $10D_h$ [40].

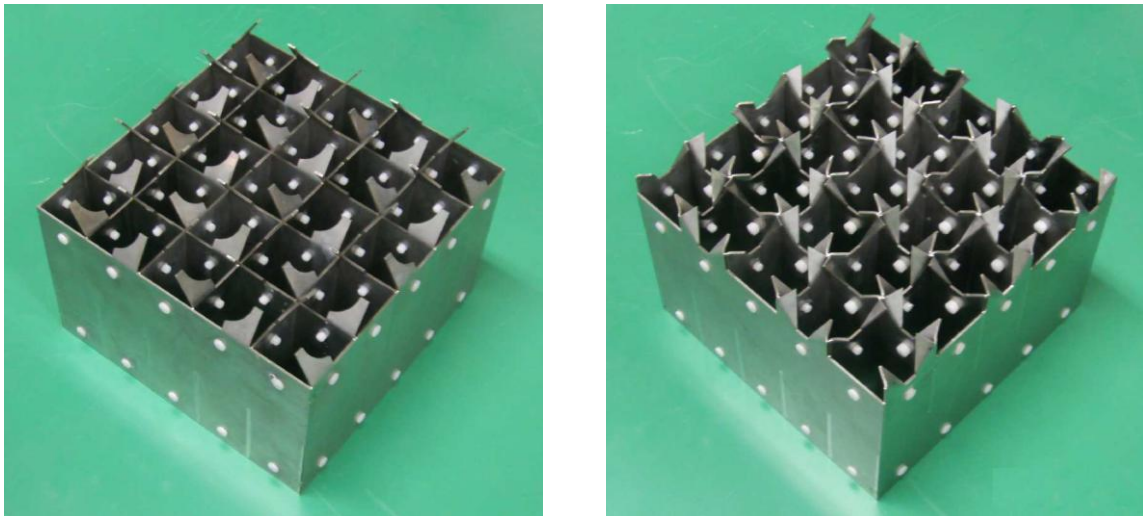

(a) **(b)**

Figure 4. Two different types of the testing spacers: (a) Split spacer, (b) Swirl spacer [40].

2.2.2 Initial and boundary conditions in the experiments

The OECD experiment was under normal pressure and temperature conditions. The operating pressure in the facility was 156.9 kPa, and the water temperature was controlled at 35°C. The inlet mass flow rate was 24.2 kg/s which implied a bulk velocity of 1.5 m/s with the Reynolds number of 50,250 that was calculated from the hydraulic diameter and the bulk velocity [40]. It is assumed that the bulk velocity is uniform at the entrance of the spacer as the boundary condition. This assumption was valid in the experiments because two straighteners were used to unify inlet flow profile. Additionally, no heat sources were applied to the experiment. Two different types of the spacers, split type and swirl type, were used to study flow patterns and turbulent behaviors.

CHAPTER III

COMPUTATIONAL FLUID DYNAMICS

In fluid mechanics, the Euler equations are used to characterize inviscid flows where viscous effects are negligible. The Navier-Stocks equations are utilized to solve viscous flows because of the additional viscosity term. In order to study turbulence, it is assumed that fluid behaviors can be predictably solved via the Navier-Stokes equations which require additional equations for closure, such as continuity equations, momentum equations, energy equations, and equation of state. However, the Navier-Stokes equations are non-linear functions that cannot currently be solved analytically, and the Navier-Stokes equations become more complicated when the problem is of more than one dimension. Using regular processes is difficult to analyze highly dimensional (3 dimensions in space and 1 time) Navier-Stokes equations, so numerical methods are used to solve fluid dynamics. In the wake of developments in semiconductors and technology, computers are more powerful to computer more data faster than before. The larger random-access memory (RAM) can provide more data storages for accelerating computations and saving time. Therefore, CFD has become a common numerical tool for solving fluid dynamics since the end of 20^{th} century. The concept of CFD is nothing but that the fluid domain is fully discrete to a large amount of volume cells for numerically calculating. CFD code then solves the governing equations for the unknown variables with given boundary conditions and physical models which will be discussed later. After multiple iterations, the code finally gets either converged or diverged due to

several reasons (algorithm, mesh quality, turbulent models, boundary and initial conditions, and etc.). Generally speaking, the convergence criteria are set to the residuals of variables (*e.g.*, velocity components and continuity) below 10^{-6}.

In the initial development, only the structure cells were applied for CFD calculations, so CFD simulations were limited to simple geometries, such as square channels and cylindrical pipes. By the algorithm improvements of discrete methods, the unstructured cells nowadays can deal with complex geometries. Direct numerical simulation (DNS) as the meaning of the name is the first method to analyze fluid dynamics used to solve the Navier-Stokes equations directly without turbulence models. Since no assumptions and models are applied to DNS, it is simple and powerful for solving every detail of the fluid in low Reynolds numbers. Unfortunately, the computational needs increases dramatically to solve lager Reynolds numbers. Furthermore, since the whole ranges of the temporal and spatial scales are resolved in DNS, a very small time discretization and an extremely fine mesh size are compulsory. The range of resolving the spatial and temporal scales is from the smallest scale, the Kolmogorov scale or the local Reynolds number of one, to the integral scale. The ratio of the integral length scale to the Kolmogorov scale is proportional to the Reynolds number to the power of ¾, and the ratio of time scale is approximate the Reynolds number to the power of ½ [63]. In other words, a 3D scenario with time requires that the total number of computational points is proportional to Reynolds numbers to the power of 3 [63]. For instance, a typical Reynolds number in aerospace is approximate 10^6, even though a supercomputer is difficult to deal with a scenario with a high Reynolds number.

3.1 Governing Equations

The governing equations in CFD are continuity equations, momentum equations, energy equations, and equation of state. In this dissertation, the isothermal condition was applied to each project. Also, a three-dimensional (3D) laboratory coordinate system was used in each project. To describe the governing equations, four parameters are listed as the follows: Temperature (T), Velocity ($\vec{v}$), Pressure (P), and Density (ρ).

Now, the mass conservation or the continuity equation is given by

$$\frac{\partial \rho}{\partial t} + \nabla \cdot (\rho \, \vec{v}\,) = 0 \qquad \text{(Eq. 3-1)}$$

Eq. 3-1 is the general form of the continuity equation and is valid for both compressible and incompressible flows. Two fluid pairs were utilized in the air ingress project. For liquid-liquid case, the incompressible condition was applied to water and brine. Since liquid is approximately incompressible, this assumption is reasonable. In the gas-gas scenario, helium and SF_6 were assumed as ideal gases with compressible flow conditions.

Secondly, the momentum conservation, or momentum equation, is the concept of Newton's second law of motion. The momentum equation is given by

$$\frac{\partial \rho \vec{v}}{\partial t} + \nabla \cdot (\rho \, \vec{v}\vec{v}) = -\nabla P + \nabla \cdot \bar{\bar{\tau}} + \rho \, \vec{g} + \vec{F} \qquad \text{(Eq. 3-2)}$$

where $\rho \, \vec{g}$ and $\vec{F}$ terms are gravity force and external force. $\bar{\bar{\tau}}$ is the shear stress tensor and is defined as Eq. 3-3

$$\bar{\bar{\tau}} = \mu \left[(\nabla \, \vec{v} + \nabla \, \vec{v}^{\,T} + \frac{2}{3} \nabla \cdot \vec{v} \, I \right] \qquad \text{(Eq. 3-3)}$$

The diagonal value of the shear stress tensor is the isotropic shear stress that is the isotropic pressure term in Eq. 3-2. If no external force exists in the problem, the last force term enable to delete. Additionally, the gravity can be ignored whether it is negligible or unrequired in the problem. The gravity was included in the air ingress phenomenon study because of gravity-driven stratified flows, but was excluded in the rod bundle benchmark problem because the geometry was a very long horizontal channel.

Subsequently, the energy conservation, or energy equation, is the first law of thermodynamics described by

$$\frac{\partial}{\partial t}(\rho E) + \nabla \cdot \left(\vec{v}\,(\rho E + P)\right) = \nabla \cdot \left(k_{eff}\nabla T - \Sigma_j h_j \vec{J}_j + \left(\bar{\bar{\tau}}_{eff} \cdot \vec{v}\right)\right) \qquad \text{(Eq. 3-4)}$$

where the total energy E and entropy h are shown in Eq. 3-5 and Eq. 3-6, respectively.

$$E = h - \frac{P}{\rho} + \frac{v^2}{2} \qquad \text{(Eq. 3-5)}$$

$$h = \int_{T_{ref}}^{T} C_{pj}\, dT \qquad \text{(Eq. 3-6)}$$

In Eq. 3-6, T_{ref} by default is room temperature, 298.15K (25°C).

Equation of State is the equation that describes the relationship of density, temperature and pressure. If the fluid is considered as the ideal gas, density will be written in a simple relationship with pressure and temperature as $\rho = \frac{P}{RT}$. The density will be a constant if the fluid is regarded as incompressible fluids.

3.2 CFD Solver

CFD codes have various solver types in each commercial code and are discussed later. The most common types are the implicit scheme and the explicit scheme that are

used for different purposes. For a given variable, the unknown and the existing values from the neighbor cells are used to solve the unknown variable in each cell in the implicit scheme. Instead, the existing values are used to calculate the unknown variable without guessing in the explicit scheme. As a result, an unknown variable will appear in all equations that are solved simultaneously in the implicit scheme. Alternatively, in the explicit scheme, the unknown variable appears in only one equation, and all unknown variables are solved one at a time. Generally, the implicit method requires extra computations because it solves all equations simultaneously. The explicit formulation is available only for the coupled solver, and the implicit formulations can be applied to either a segregated or a coupled solution method. The segregated approach solves a single variable at a time, but the coupled approach solves all variables at the same time. Generally speaking, the coupled solver requires more computational time during iterations, but the segregated solver spends less time during iterations. However, the segregated solver needs more iteration to reach convergence criteria. Both methods have been modified to solve and operate for a wide range of flow conditions.

The SIMPLE algorithm is the only pressure-velocity coupling solver for the segregated flow model in STAR-CCM+ [55]. In ANSYS CFX, the pressure and velocity are fully coupled (no segregated solver), and the momentum-like equation is applied in the calculating domain. Rhie Chow discretization is used to model pressure-velocity coupling [56]. In FLUENT, five pressure-velocity coupling algorithms are applied to the segregated algorithm: SIMPLE, SIMPLEC, PISO, Coupled, and Fractional Step. SIMPLE and SIMPLEC methods solve velocity and pressure separately and calculate

the pressure correction to correct pressure which is used to satisfy the continuity equation. SIMPLEC is a modified method in order to accelerate convergence in problems to solve pressure-velocity coupling. The PISO pressure-velocity coupling algorithm is a further modification of SIMPLE method to satisfy better momentum balance after solving the pressure-correction. The PISO scheme shows good performance in neighbor corrections and skewness corrections. The fractional step method uses operator-splitting or approximate factorization to solve momentum and continuity equations. The couple algorithm is suggested in a problem with poor quality of meshes or large time steps in FLUENT [57].

3.3 Turbulence Modeling

Flow behaviors become more complex in the high Reynolds numbers. Turbulent flows are characterized by fluctuating velocity fields that contain transport properties which are of small scales and high frequencies. The computational resource of these small turbulent quantities is time consuming when the simulation proceeds in practical engineering applications. To study complex fluid dynamics, turbulent models are used to reduce computational resource. Two main different turbulent models, RANS and LES, were used for studying the problems. The turbulent models applied in this dissertation are the Realizable k-ε model, the shear stress transport k-ω model, and the LES approach [55-57].

3.3.1 Realizable k-ε model

The k-ε model is a two-equation model where the turbulent kinetic energy k and its dissipation rate ε are implemented. Many forms of the k-ε models have been

developed in the past few decades, and the k-ε model has become the most widely used model in academy and industrial applications. The difference between the Standard k-ε model and the Realizable k-ε model is the difference of coefficient of the dissipation rate [55-57]. The Realizable k-ε model practically has better performance than the Standard k-ε model for many applications since the coefficients are calibrated with experimental data and a new transport equation for the turbulent dissipation rate is applied. The Bussinesq approximation and the eddy viscosity definition are two principles of the Realizable k-ε model used to solve the transport equations of the turbulent kinetic energy, k, and the dissipation rate, ε. The turbulent viscosity coefficient in the Realizable k-ε model replaces the constant value in the Standard k-ε model. The examples of the transport equations of the turbulent kinetic energy and the dissipation rate are shown in Eq. 3-7 and Eq. 3-8.

$$\frac{\partial(\rho k)}{\partial t}+\frac{\partial(\rho k u_j)}{\partial x_j}=\frac{\partial}{\partial x_j}\left[\left(\mu+\frac{\mu_t}{\sigma_k}\right)\frac{\partial k}{\partial x_j}\right]+G_k+G_b-\rho\varepsilon-Y_M \quad \text{(Eq. 3-7)}$$

$$\frac{\partial(\rho \varepsilon)}{\partial t}+\frac{\partial(\rho \varepsilon u_j)}{\partial x_j}=\frac{\partial}{\partial x_j}\left[\left(\mu+\frac{\mu_t}{\sigma_\varepsilon}\right)\frac{\partial_\varepsilon}{\partial x_j}\right]+C_{1\varepsilon}\frac{\varepsilon}{k}C_{3\varepsilon}G_b-\rho C_{2\varepsilon}\frac{\varepsilon^2}{k+\sqrt{v\omega}} \quad \text{(Eq. 3-8)}$$

$$G_k=-\rho\overline{u'_\iota u'_J}\frac{\partial u_j}{\partial x_i} \quad \text{(Eq. 3-9)}$$

$$G_b=\beta g_i\ \frac{\mu_t}{Pr_t}\frac{\partial T}{\partial x_i} \quad \text{(Eq. 3-10)}$$

where $G_k$and $G_b$are the turbulent production term and the buoyancy production term, respectively. Y_M is defined as the fluctuating dilation in compressible turbulence considered for high Mach number flow, and is given by $Y_M=2\rho\varepsilon M_t^2$. The turbulent production term, the buoyancy production term, and the dilatation dissipation term may

be defined differently in each code. Coefficients used in Eq. 3-7 to Eq. 3-10 are different in each code [55-57]. Here, the basic concepts are described.

3.3.2 Shear stress transport k-ω model

The k-ω model is another two-equation model compared to the k-ε model. Two governing transports equations are the turbulent kinetic energy k and a specific dissipation rate ω which is defined from ε and k. Similarly, many k-ω models have been developed. The advantage of the k-ω model is that the k-ω model performs better for boundary layers under adverse pressure gradient than the k-ε model. Generally speaking, the k- ε models predict the onset of separation later than the real condition and under-predict the later calculations. In order to overcome this problem, the k-ω model developed to solve this issue provides remarkable accurate predictions in many cases. An innovative k-ε model, the shear stress transport k-ω (SST k-ω) model, was developed to provide more accurate performance of the onset of the flow separation. Moreover, the SST k-ω model accounts for the transport effects of the turbulent shear stress, and the eddy viscosity is over-predicted without this assumption. The modified productions terms of the k and ω equations are added to the SST k-ω model. The transport equations of the turbulence kinetic energy and the specific dissipation rate are described by

$$\frac{\partial(\rho k)}{\partial t} + \frac{\partial(\rho k u_i)}{\partial x_i} = \frac{\partial}{\partial x_j}\left[\Gamma_k \frac{\partial k}{\partial x_j}\right] + G_k - Y_k \qquad \text{(Eq. 3-11)}$$

$$\frac{\partial(\rho \omega)}{\partial t} + \frac{\partial(\rho \omega u_i)}{\partial x_i} = \frac{\partial}{\partial x_j}\left[\Gamma_\omega \frac{\partial \omega}{\partial x_j}\right] + G_\omega - Y_\omega \qquad \text{(Eq. 3-12)}$$

where $\Gamma_k = \mu + \frac{\mu_t}{\sigma_k}$, $\Gamma_\omega = \mu + \frac{\mu_t}{\sigma_\omega}$, and $\omega = \frac{\varepsilon}{k}$

G_k, G_ω, Γ_k, and Γ_ω are the turbulent production term, the production of specific dissipation rate, and the effective diffusivity of k and ω, respectively. The definition of $G_k$is the same as Eq. 3-9. G_ω, Γ_k, and Γ_ω are given by Eq. 3-13, Eq. 3-14, and Eq. 3-15, respectively.

$$G_\omega = \alpha \frac{\omega}{k} G_k \quad \text{(Eq. 3-13)}$$

$$Y_k = \rho \beta f_\beta k\omega \quad \text{(Eq. 3-14)}$$

$$Y_\omega = \rho \beta f_\beta \omega^2 \quad \text{(Eq. 3-15)}$$

Y_k and Y_ω represent the dissipation of k and ω due to turbulence. Again, the turbulent production terms and the effective diffusivity terms may vary in different codes. The corresponding coefficients and constants used in Eq. 3-13 to Eq. 3-15 can be found in each code [55-57].

3.3.3 Large eddy simulation

Turbulent eddies contain a wide range of length and time scales, especially in high Reynolds number. Using DNS solves a turbulent flow with high Reynolds number is not practicable. Clearly, a new turbulent model is required to solve this problem. Large eddy simulation (LES) resolves large eddies directly and models small eddies. LES is a completely new concept compared to RANS models for the turbulent modeling [64]. All RANS models use the time-average concept to obtain average physical quantities. LES approaches utilize spatial average to separate large and small scales. When the mesh size is decided, eddies that are smaller than the mesh sizes will be filtered. Then, the governing equations are filtered in the physical space. Since the

average of the fluctuation term is not zero, filtering the Navier-Stocks equations leads to additional unknown quantities shown in Eq. 3-16.

$$\tau_{ij} = \overline{U_i U_j} - \overline{U}_i \overline{U}_j \quad \text{(Eq. 3-16)}$$

The new unknown is named as subgrid-scale stress. The eddy viscosity approach is defined by the relationship between the subgrid-scale stresses and the large-scale strain rate tensor which are described in Eq. 3-17 and Eq. 3-18, respectively.

$$\left(\tau_{ij} - \frac{\delta_{ij}}{3}\tau_{kk}\right) = 2\nu_{sgs}\overline{S_{ij}} \quad \text{(Eq. 3-17)}$$

$$\overline{S_{ij}} = \frac{1}{2}\left(\frac{\partial \overline{U_i}}{\partial x_j} + \frac{\partial \overline{U_j}}{\partial x_i}\right) \quad \text{(Eq. 3-18)}$$

Different subgrid-scale (SGS) models are used to model the eddy viscosity, ν_{sgs}. Unlike RANS models, which use the eddy viscosity to represent all turbulent scales, the SGS viscosity is only applied to model small scales in LES.

In STAR-CCM+, two SGS models are available: the Smagorinsky model and the wall-adapted local eddy-viscosity (WALE) model. First of all, the Smagorinsky model is based on the dimensionless analysis and is proportional to the unresolved length scale (usually mesh size) and the unresolved velocity scale. The coefficients for Smagorinsky SGS model vary with the geometry and mesh resolution. Since the Smagorinsky SGS model is coefficient sensitive, the WALE model is the innovative modification that has lesser coefficient sensitive and can reproduce correct turbulent viscosity for laminar shear flows, where the Smagorinsky SGS model produces non-zero values [55].

3.4 Wall Treatments

Turbulent behaviors at the near-wall region are significantly anisotropic, so using the original numerical method to solve the viscous sublayer is insufficient. Resolving near-wall region requires a very refined grid mesh and massive computations. In order to reduce computational needs, the suitable wall treatments have been developed.

Three wall treatments in STAR-CCM+ are low y+ wall treatment, high y+ wall treatment, and all y+ wall treatment. The low y+ wall treatment basically solves the low-Reynolds number turbulence which assumes that the viscous sub-layer is properly resolved without wall functions (y+ is approximately 1). The high y+ wall treatment is the approach that the near-wall cell locates on the logarithmic region of the boundary layer (y+ >30). In other words, coarse meshes may use the high y+ wall treatment rather than the low y+ wall treatment which is suitable for fine meshes. The all y+ treatment is the hybrid treatment that combine the low y+ and high y+ wall treatments. If the near-wall cell locates at the buffer region (1< y+ <30), the all y+ wall treatment will automatically compute the reasonable results for the desirable characteristic [55].

The scalable wall functions and automatic near-wall treatment are available in ANSYS CFX. Even though the standard wall function can be selected, it is not suggested to be used because it has no advantage over the scalable wall functions. The scalable wall function allows for solving most of the near-wall turbulence. However, if a very fine mesh is applied to the near-wall region, the SST model with automatic near-wall treatment is recommended because of extra effects in the sublayer. The automatic near-wall treatment is developed to solve the region with low turbulent Reynolds

number, especially the highly refined near-wall grid resolution (y+<0.2). The automatic near-wall treatment is the default in all models based on the ω equations [56].

The scalable wall function in ANSYS FLUENT is a modified wall treatment from the standard wall function for y+<11. If the mesh is coarser than y+>11, the scalable wall function is identical to the standard wall function. The enhanced wall treatment is a new concept combining a two-layer model with enhanced wall function which is modified with different coefficients. If the near-wall mesh is fine enough to resolve the viscous sublayer (y+ close to 1), the enhanced wall treatment is identical to the traditional two-layer zonal model [57].

3.5 Solution Controls

STAR-CCM+ was used to simulate most of the cases. The 2nd order upwind method was applied to the convection and transient terms in STAR-CCM+ because it is essential the 2nd order accurate over the 1st order scheme. In STAR-CCM+, the central-differencing scheme was applied to preserve turbulent kinetic energy in LES, where the upwind schemes cause turbulent kinetic energy to decay abnormally fast [55]. The central-differencing method has the same order accuracy as the 2nd order upwind method. In the cases simulated by FLUENT, the 2nd order upwind method was selected to the convection and the transient terms. The high resolution method that was between the 1st and the 2nd order was implemented in CFX [55-57].

3.6 Convergence

In all simulations, the residuals of all solving variable were monitored. In both LES approaches and RANS models, the continuity, the velocity components, and the

pressure were monitored to check the convergence criteria. In the cases applying RANS models, the additional turbulent kinetic energy and the dissipation rate were monitored. A criterion of 10^{-6} is considered for reaching convergence. The criterion can be set even lower to obtain more accurate results, but this will result in requiring more time to reach convergence.

CHAPTER IV

DESCRIPTION OF THE CFD MODEL DEVELOPED

Many issues can significantly influence CFD simulation results, such as mesh type and sizes, turbulent models, near-wall treatments, and boundary conditions. Usually, a coarse mesh size predicts unstable calculations; as a consequence, the mesh size independent study is used to obtain calculations with high confidence. Besides, understanding appropriate assumptions and models before implementation in the simulation is extremely required; otherwise, the results are inaccurate or meaningless. Wrong boundary conditions result in incorrect answers even though the simulations are converged; therefore, results are more meaningful with proper boundary conditions. Currently, it is not possible to directly solve Navier-Stokes equations without any turbulence models, such as RANS and LES, because it consumes enormous computational resources to solve all details. Selecting a suitable turbulent model, using reasonable boundary conditions, and using enough fine mesh size are the optimizations for CFD.

4.1 Section 1 – Air Ingress Phenomenon

STAR-CCM+5.02 was the software used in all air ingress simulations. The dimensions of the geometry, the grid sizes of meshes, the selections of the turbulent models, the initial and boundary conditions, the working fluids, and the technique of obtaining transient results were discussed in the following sub-sections.

4.1.1 Simulation geometry and mesh grids

Since the study is to mimic the heavy fluid intruding into the reactor, the experimental configuration has been modified to a simple geometry that contains two tanks, one valve, and one co-annular duct with two lengths (0.38m and 1m) as illustrated in Figure 5. Unlike the experimental geometry (Figure 2), the heavy fluid was placed in the right tank, and the light fluid was located in the left tank (Figure 5). Three different mesh sizes of 1.5 mm, 1.0 mm, and 0.7 mm shown in Figure 6 were used for the mesh size sensitivity study and also for the computational uncertainty study [65]. Because the focus was on the flow behaviors inside the coaxial pipe, the finer mesh size was only applied to the pipe region in order to obtain more details.

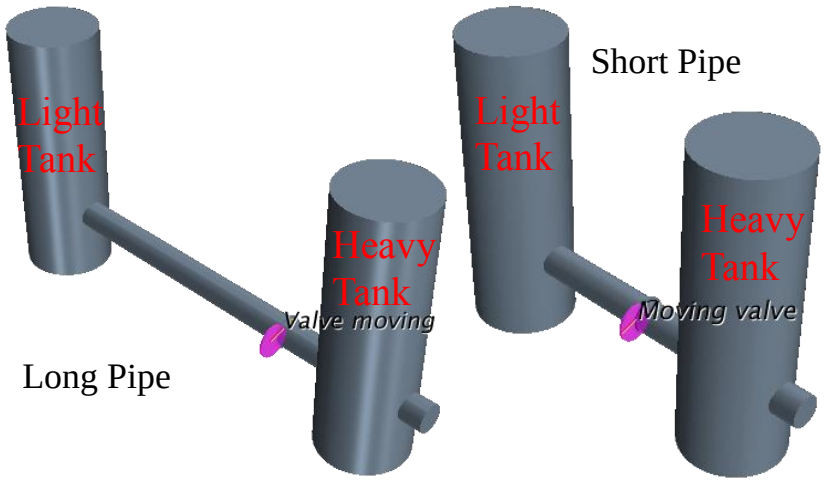

Figure 5. Geometry representation in the simulations: tanks, coaxial pipe, and valve.

In the other parts of the flow domain, 2.5 mm surface size was set for all cases to mesh grids to reduce computational needs. For example, in the case has with the highest number of the volume cells, the 2.5 mm surface mesh size was set everywhere and the 0.7 mm surface mesh size was used on the pipe. The polyhedral volume mesh was applied to generate volume cells. Mesh size sensitivity study was only performed on the short-pipe geometry in which cases with 1.5 mm, 1.0 mm, and 0.7 mm surface sizes contained approximately 5.4M, 10.6M, and 23.5M volume cells, respectively [65]. For the long-pipe geometry, only the 0.7 mm surface size was utilized, and the total polyhedral volume cells were approximate 40M volume cells [65]. Table 2 lists the information of the geometries and the mesh sizes with corresponding amount of volume cells.

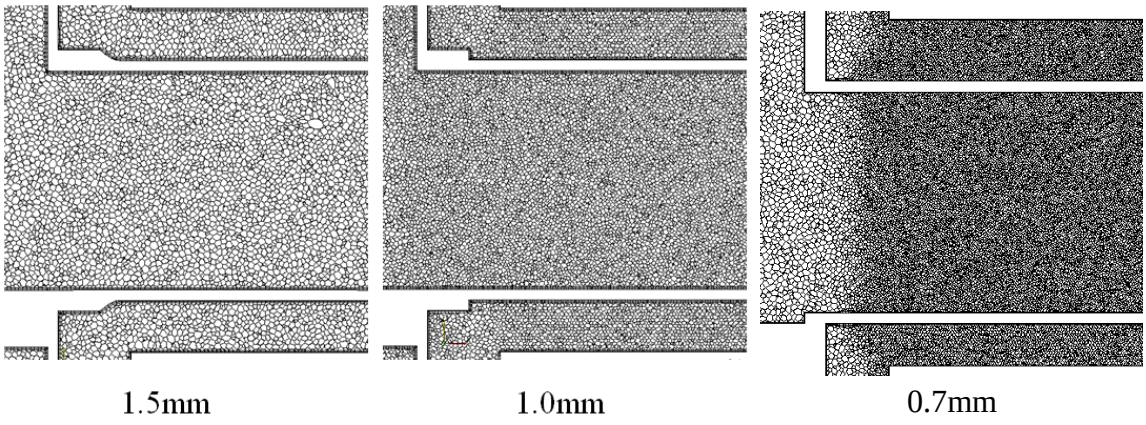

Figure 6. Mesh presentations at the coaxial pipes in the simulations. Polyhedral volume cells were applied to generate meshes.

Table 2. Lists of mesh size and number of volume cells.

Grid Number	Cell Size	Number of Cells	Geometry
0	0.7 mm	39.8M	Long
1	0.7 mm	23.5M	Short
2	1.0 mm	10.6M	Short
3	1.5 mm	5.4M	Short

4.1.2 Turbulent models selections

The air-ingress problem was a transient accident, so the implicit solver was used to solve the governing equations. The unsteady RANS (URANS) model and the LES approach in STAR-CCM+ were two different concepts of turbulent models applied to this study in order to compare the results [55]. The RANS model is based on the time-averaged properties of the fluid flow, which are divided into two parts (i.e., the average value and the fluctuating part). On the other hand, the LES model is the concept based on the spatial average that depends on the mesh size as the filter, which separates fluid quantities into the spatial average term and the fluctuating term [64]. As described in Section 3.3.3, the unresolved limit of the filter depends on the grid size. The comparison between the averaging quantities (URANS) and the instantaneous results (LES) was described in CHAPTER VI. The unsteady Realizable k-ε two-layer model was selected to solve the average quantities at each time step in this study. The instantaneous quantities in the LES model were directly solved in large scales, and the unresolved quantities were modeled in small scales. As a result, the WALE SGS model was applied to compute the unresolved turbulent scales for the transient problem. In order to simulate

the turbulent effects in the near-wall region, all y+ wall treatments were selected for both turbulent models.

4.1.3 Description of the simulations

As described in Section 2.1.3, the tanks were filled with two fluids and were blocked by the valve which was assumed to open in 0.534s with a constant speed. In some scenarios, the valve was considered fully open as the initial condition. For example, the fully open valve was implemented to the mesh sensitivity study. This assumption is acceptable because the purpose of the sensitivity study is to understand the mesh size convergence. Three different mesh sizes of 1.5 mm, 1.0 mm, and 0.7 mm were applied for the grid size independent study where the simulations utilized He-SF_6 as the fluid pairs with the Realizable k-ε model, the short pipe geometry, and the fully open valve condition. These simulations as describe in Section 4.1.1 contain 5.4M, 10.6M, and 23.5M cells [65]. The time step was set to one millisecond (1ms) in all simulations. The gravity influence was set in the negative y direction to include gravity effects.

For the valve moving test, the Unsteady Realizable k-ε model was used because the Realizable k-ε model was the only model applied to the fully open valve scenarios. The LES model was utilized in the pipe length study. Using the different pipe length was to investigate the effects of the break location on the coaxial pipe. In order to collect simulation results, two horizontal and six vertical line probes were included in the simulation. Two horizontal probes, line-probe HU and line-probe HB, were aligned with the walls of the inner and the outer pipes, respectively (Figure 7). The vertical probes were located at equal distances from the entrance of the tank to the valve as presented in

Figure 7. Besides, an axial plane cross-section of the inner pipe was created to obtain results shown in Figure 8. The resolutions of the horizontal and vertical axes were identical to the mesh size that was set to 0.7 mm. Therefore, the axial plane cross-section that was equally discretized with 0.7 mm contained total 1471 by 101 cells. Four transverse plane sections were created to store the transient graphs in each time step for the short-pipe simulations as shown in Figure 9. As presented in Figure 10, seven transverse plane sections were used for the long-pipe simulations. The additional transverse plane section was illustrated in Figure 11. The first transverse plane section in both short-pipe and long-pipe cases located at the valve. Figure 12 gives an example of one axial plane section at the time step of 0.567 second. The simulation results in RANS model were compared with the efforts in LES approaches.

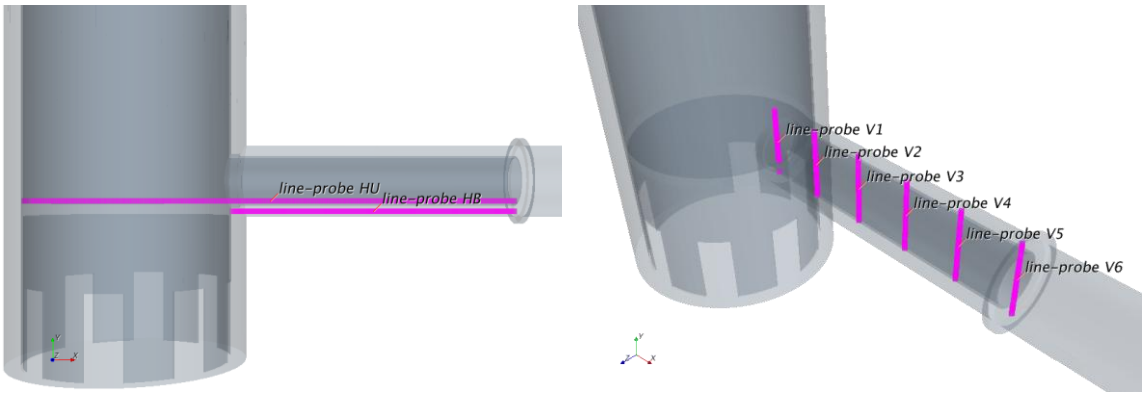

Figure 7. The horizontal and vertical line probes to record transient results.

Figure 8. An axial plane cross-section presentation used to obtain results. The resolutions in horizontal and vertical directions are 1470 and 101, respectively.

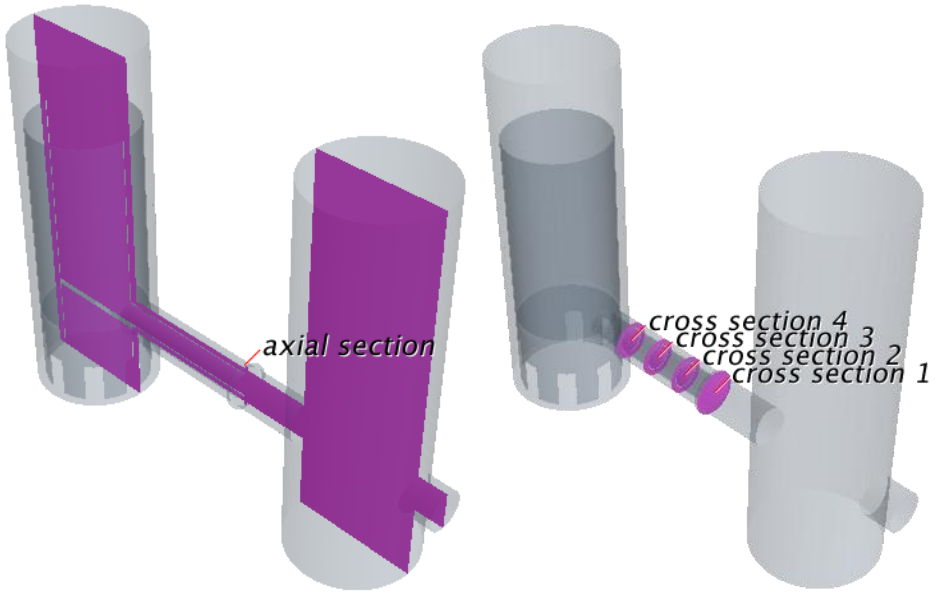

(a) (b)

Figure 9. The plane cross-sections used in the short-pipe scenario in STAR-CCM+. (a) one axial cross-section, (b) four transverse cross-sections.

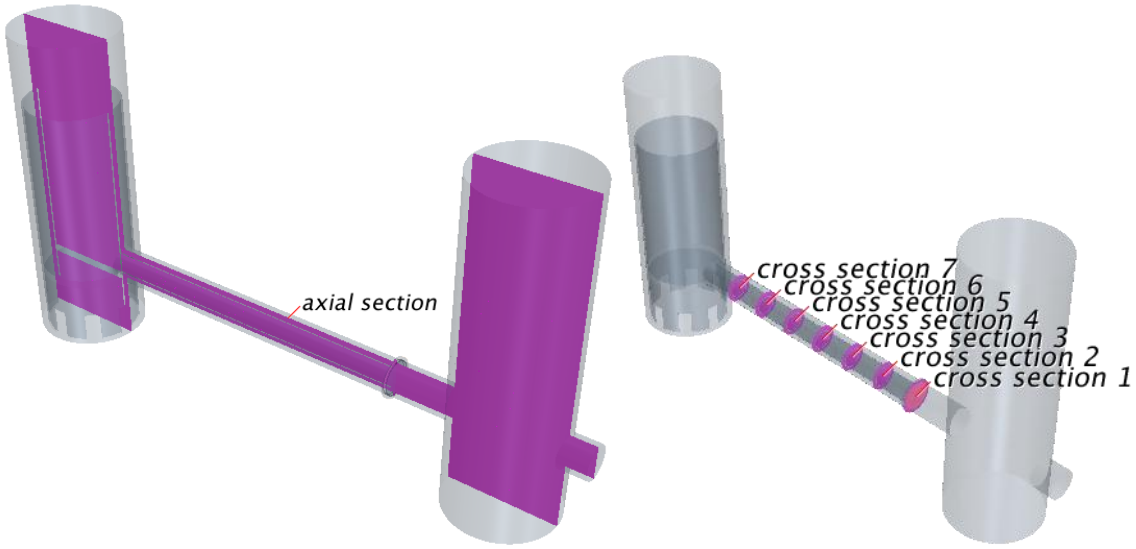

(a) **(b)**

Figure 10. The plane cross-sections used in the long-pipe scenario in STAR-CCM+. (a) one axial cross-section, (b) seven transverse cross-sections.

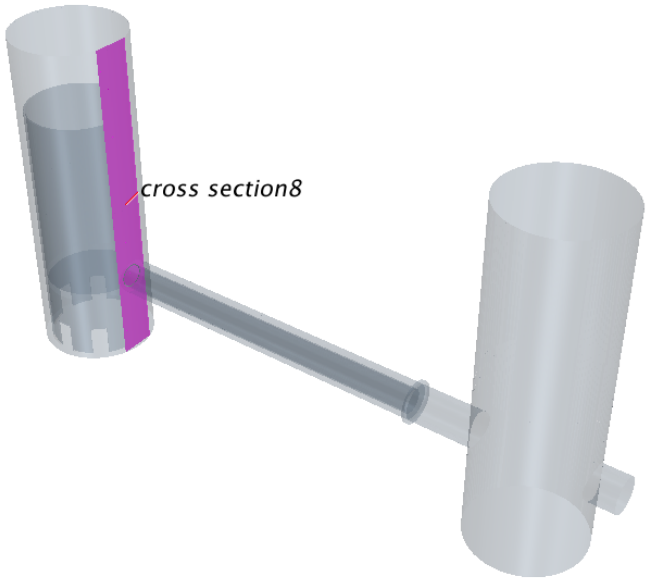

Figure 11. The plane cross-sections located near the entrance of the tank in the long-pipe simulation in STAR-CCM+.

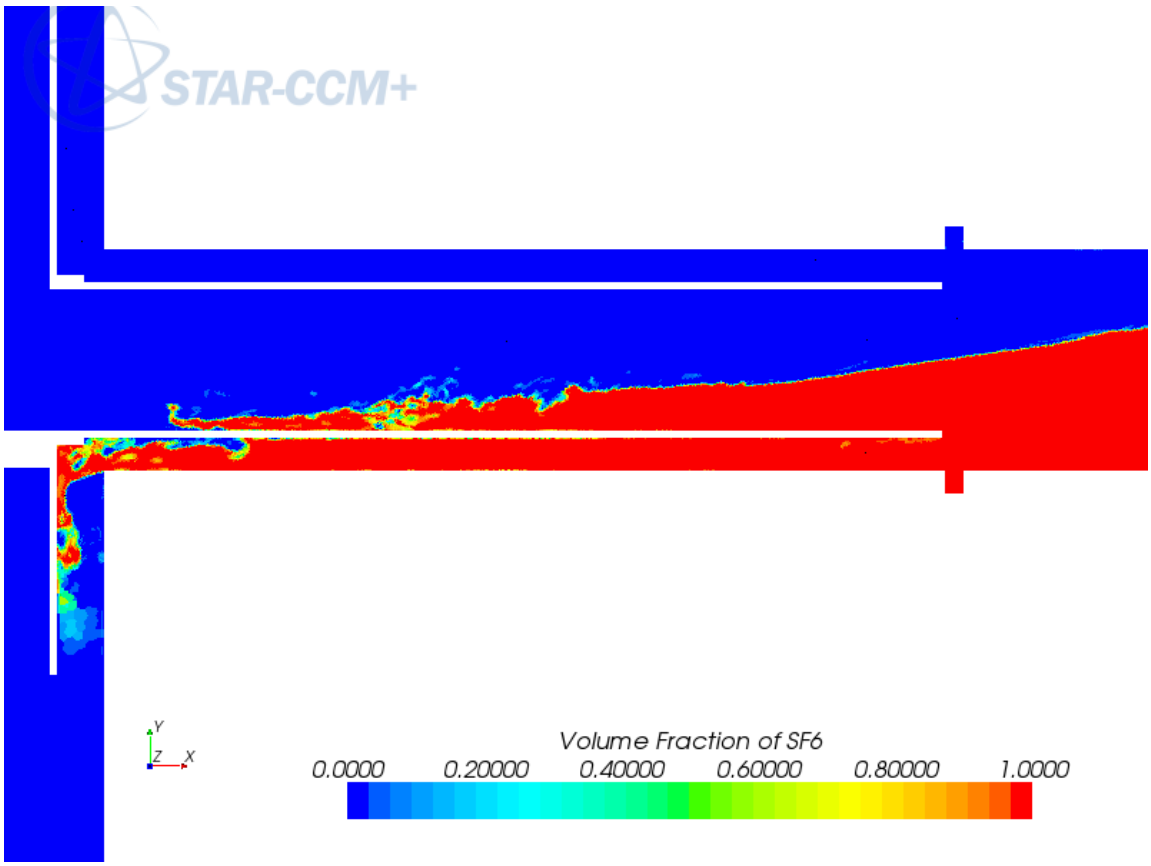

Figure 12. Example of the He-SF_6 short pipe simulation with 0.7 mm mesh size and LES modeling at 0.567 second.

4.2 Section 2 – OECD Bundle Benchmark Problem

In the rod bundle problem, three different commercial codes, which were STAR-CCM+5.02, ANSYS CFX13, and ANSYS FLUENT13, were used for the simulations in order to validate with the experimental data and to compare the codes to each other. The simulation geometry and settings were described in the following sub-sections, such as the selections of the turbulent models, the initial and boundary conditions, and the technique of obtaining transient results.

4.2.1 Simulation geometry and mesh grids

The simulation geometry was identical to the dimensions of the experimental facility except the upstream region prior to the second flow straightener. Figure 13 illustrates the simulation geometry that is similar to Figure 3. The upstream distance between the 2nd straightener and the spacer in the simulations was 242.7 mm ($100D_h$) that was the same distance in the experiment [40]. The downstream distance (Z) between the top of the vanes to the 3-leg structure were different in two spacers because the dimensions of the vanes were changed. The swirl type spacer was slightly longer than the split type spacer. The total length of the simulation geometry was approximate 4m which caused massive computations. A coarse mesh with split spacer was used to for testing simulation results in using CFX code. After preliminary comparison with experimental data, a finer mesh was applied to the geometries with split and swirl types of spacers. Even though the mesh size was finer, the simulation results showed significant discrepancies to experimental data. The finest mesh size of 0.5 mm was decided to generate the latest mesh grids.

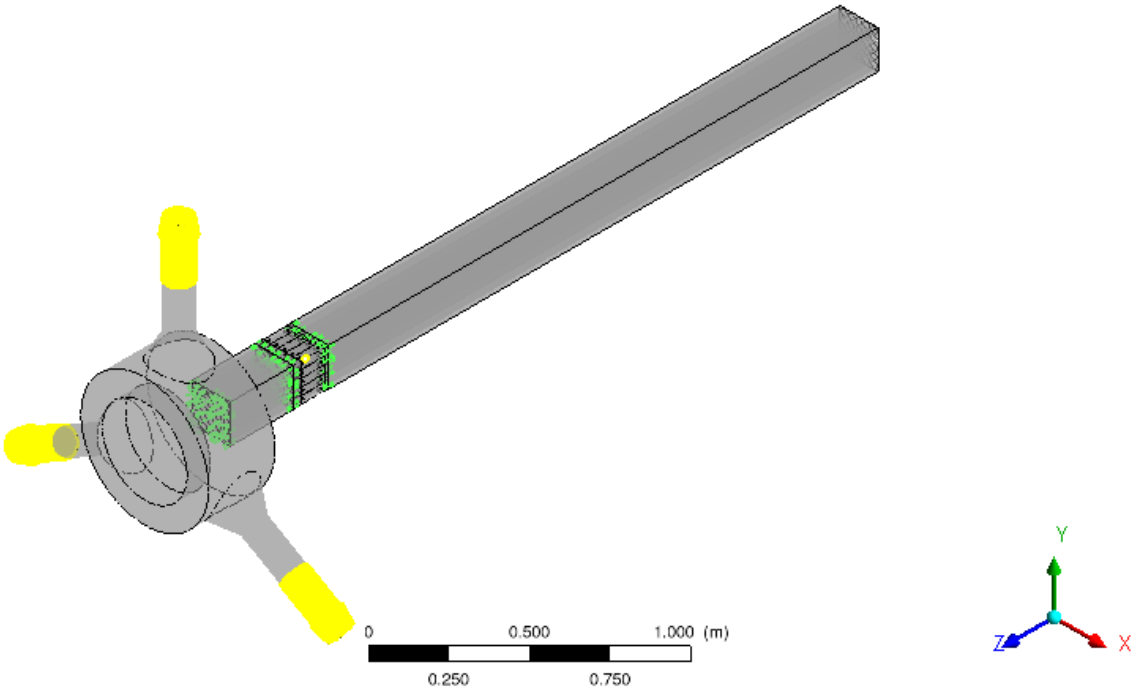

Figure 13. Geometry in the simulation: inlet, spacer (two types), downstream outlet, and 3-leg outlet device. The yellow bars showed the outlet locations. The green area presented the interfaces between two regions.

Table 3 lists all mesh sizes, spacer types, corresponding number of volume cells, and the using CFD codes. The same geometry and mesh grids of split type spacer were used for the three commercial codes, which is referred to as the code-to-code comparisons. The tetrahedral volume meshes were implemented to the spacers for overcoming the problem that the spacers contained complex geometries, such as springs and vanes. The hexahedral volume meshes were applied to the other portions of the geometry that was relatively simpler to generate structure meshes. Figure 14 (a) and (b) show the examples of the mesh presentations for the spacer and the other regions of the split spacer and the swirl spacer, respectively. The examples of the mesh files with 1.0 mm mesh size shown in Figure 14 were applied to CFX, FLUENT, and STAR-CCM+ as listed in Table 3. Furthermore, the finest mesh was implemented in the simulations that were simulated by STAR-CCM+. Figure 15 presents the examples of the finest mesh applied to STAR-CCM+.

Table 3. List of the spacer type, the corresponding mesh size with the numbers of cells, and the CFD Codes.

Spacer Type	Cell Size	Number of Cells	CFD Codes
Split	1.5 mm	25M	CFX
Split	1.0 mm	65M	CFX & FLUENT & STAR-CCM+
Swirl	1.0 mm	68M	CFX & FLUENT
Split	0.5 mm	128M	STAR-CCM+
Swirl	0.5 mm	160M	STAR-CCM+

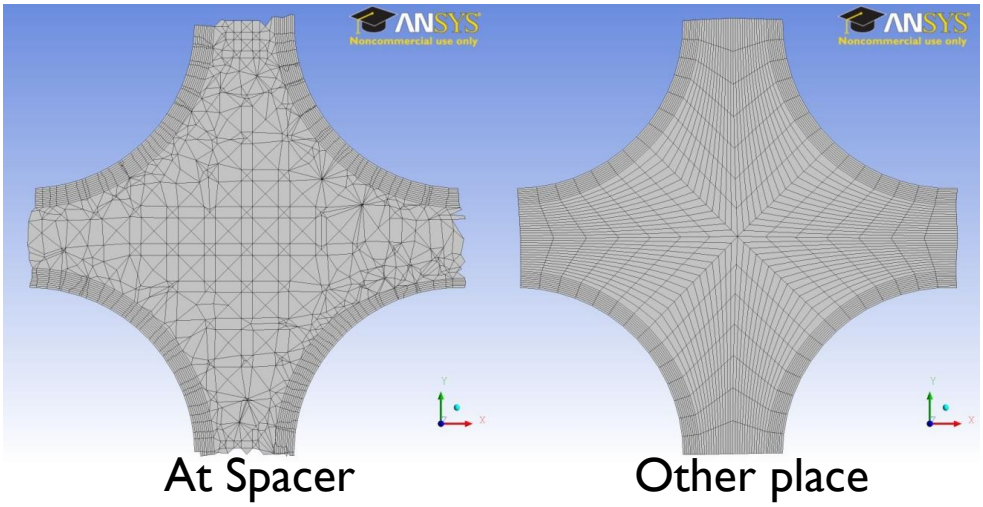

(a)

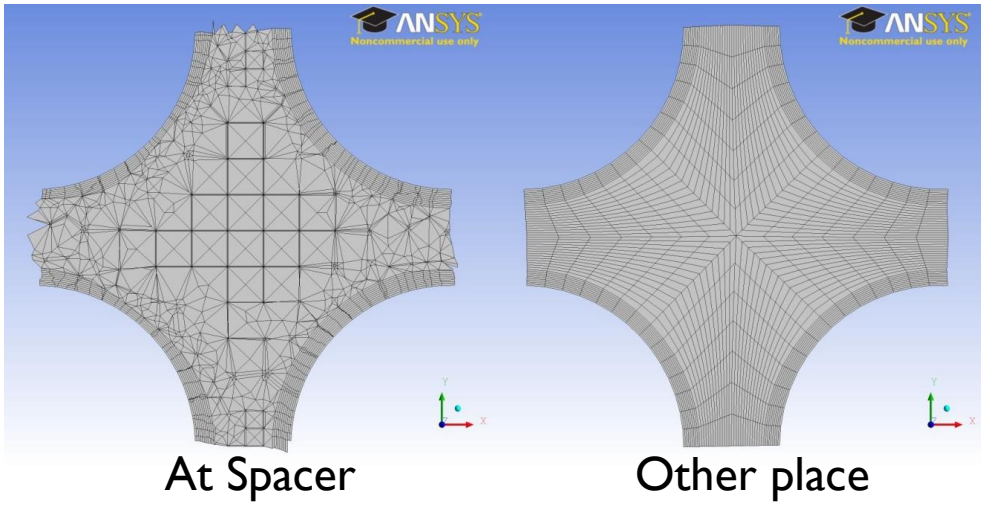

(b)

Figure 14. Mesh presentations at the spacer region and the other place. Tetrahedral volume cells were used in the spacer region. The other places utilized fully hexahedral volume cells. (a) split type spacer, (b) swirl type spacer.

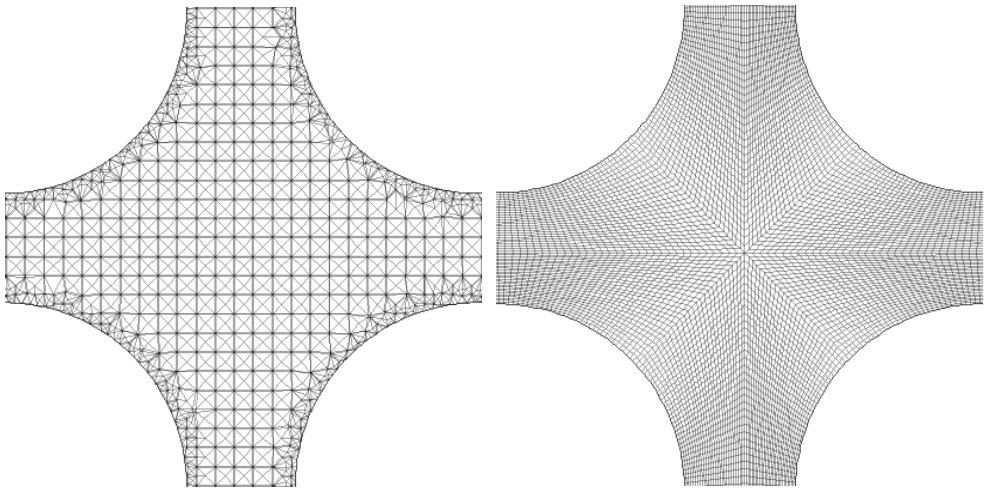

Figure 15. The finest mesh presentation in STAR-CCM+ for the spacer region and the other places.

4.2.2 Turbulent models selections

The OECD rod bundle exercise was considered as a transient problem, and the experimental data were the mean physical quantities with turbulent intensities. If only the mean quantities are considered for the comparison, the steady solver will be sufficient. If the turbulent intensities are required, two methods will be available to achieve this requirement. Running the simulation with URANS models can obtain both mean quantities and fluctuating variables. The other method is to use LES approaches that give instantaneous results. The simulation using a LES model requires sufficient time period in order to reach quasi-steady state. Then, the averaging process can be applied to LES results for calculating mean quantities and their fluctuating intensities. It was difficult for FLUENT solvers to handle the computations with the unsteady

schemes. As a result, the steady SST k-ω model with the enhanced wall treatment was applied to FLUENT. STAR-CCM+ had the same issue as FLUENT, so the steady Realizable k-ε model with two-layer all y+ wall treatment was used. CFX had better performance in handling the computations with unsteady schemes. The unsteady SST k-ω model with the scalable wall function was used.

In order to predict more accurate results, a 0.5 mm surface mesh size was used to generate a new volume mesh. The new case with 0.5 mm surface mesh size contained 128M volume cells for only the spacer and the downstream outlet. Since the uniform velocity was applied to the entrance of the spacer, using the geometry with only the spacer and the downstream outlet was sufficient. Additionally, only the simulations with the finest mesh size contained better mesh qualities, so the LES model and unsteady Realizable k-ε model with two-layer all y+ wall treatment were used in STAR-CCM+ to simulate this problem.

4.2.3 Description of the simulations

As described in Section 2.2.2, the OECD rod bundle exercise was simple because the boundary conditions were simplified for this study in both types of the spacers. Water was used as the working fluid in the simulations with a constant temperature of 35°C without heat sources, so the isothermal condition was applied to all simulations. Since the geometry was a long horizontal channel, the gravity influence was negligible. Moreover, the operating pressure was under normal pressure condition of 156.9kPa with a reference pressure of 1 atmosphere in the simulations. The uniform inlet velocity of 1.5m/s was used as the boundary condition [40]. Split and swirl spacers were

implemented to this exercise for studying the flow features and turbulent behaviors. Three different mesh sizes that were simulated in CFX were used for the mesh size sensitivity study. In the unsteady schemes, the time step was set to one millisecond (1ms) for the both URANS and LES models. The unsteady SST k-ω model was applied to CFX for both split and swirl spacers. The steady SST k-ω model was utilized to FLUENT for both spacers geometries. In STAR-CCM+, the steady Realizable k-ε model was used for both scenarios. For cases with the finest mesh size, the steady Realizable k-ε model and LES approaches were used for two types of the spacers.

Four planes in different heights (Z-positions) were created to extract simulation results. Each plane had three lateral line-probes which were located at different Y-positions along with X-axis, so twelve horizontal line-probes were created in order to compare with the experimental data. Figure 16 presents the examples of twelve line-probes that were demonstrated in STAR-CCM+. The identical line-probes were generated in CFX and FLUENT at the same locations. In addition, three axial plane cross-sections that were located at the same Y-positions were created to obtain instantaneous results shown in Figure 17. Only three axial cross-sections were provided in the simulations with the finest mesh size. The resolutions of the horizontal and vertical axes were identical to the mesh size of 0.5 mm, so each plane cross-section contained total 340 by 400 cells.

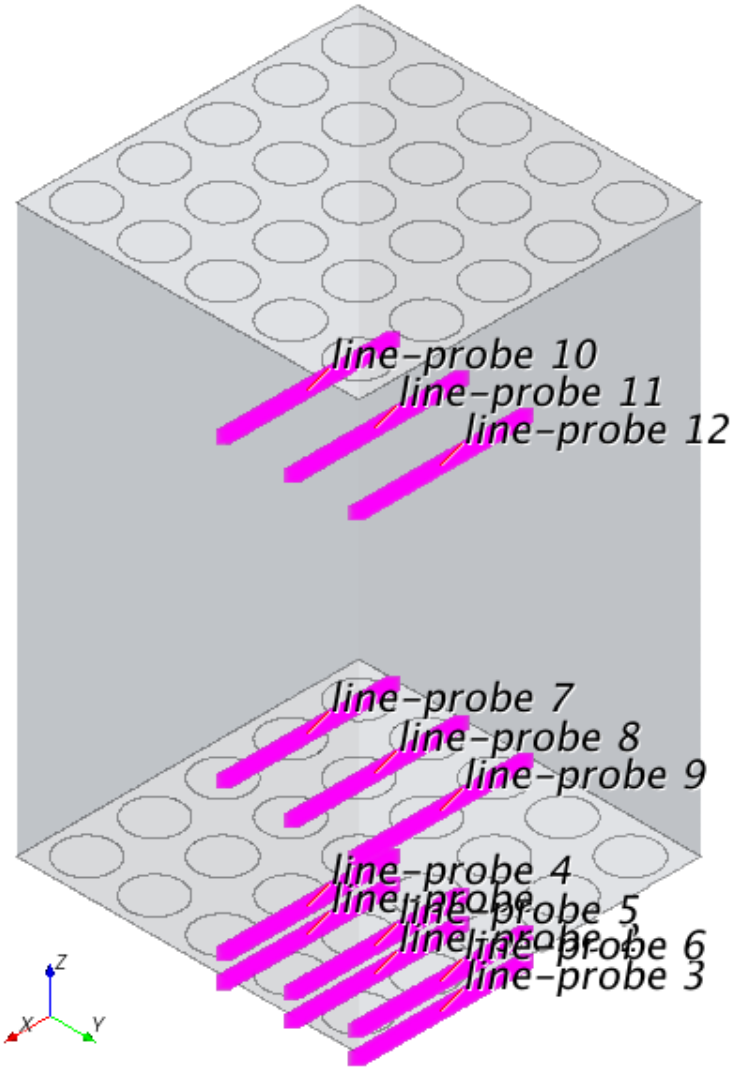

Figure 16. Twelve horizontal line-probes evenly located at four planes. Each plane with different height had three line-probes that were at the same locations projecting to x-y plane.

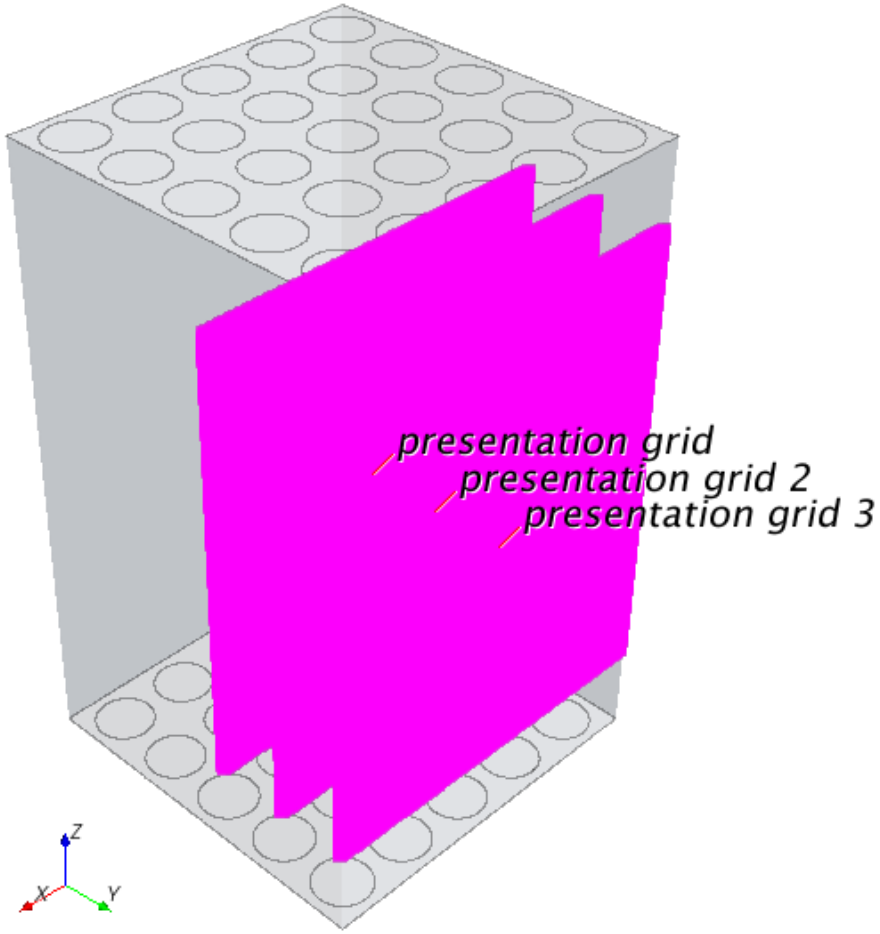

Figure 17. Three axial plane cross-sections were used to extract results for analyses.

CHAPTER V

ANALYZING METHODOLOGY

5.1 Turbulent Analyses Methods

Comparing simulation results with experimental data is the most convenient way to validate and verify CFD efforts. Besides, the spectral analysis is used to study CFD simulations. Fast Fourier Transform (FFT) is the command tool for analyzing datasets in the spatial or the temporal domains. Furthermore, FFT can be used to study Kolmogorov's hypothesis where the fluctuating velocities are required to create a turbulent kinetic energy spectrum [63]. If a scenario is a strong transient phenomenon that contains more information of velocity evolution rather than the turbulence cascading energy spectrum, the study of Kolmogorov's hypothesis will be inappropriate [63]. Therefore, it was difficult to create turbulent kinetic energy spectra for the air ingress phenomenon; instead, the energy spectra of the flow evolution were compared in URNAS and LES models. Moreover, Fourier analysis was applied to the OECD rod bundle study for analyzing turbulent kinetic energy spectra that was available with respect to Kolmogorov's hypothesis [63]. Since the OECD study was a quasi-steady state problem, it had no strong effects of the flow evolution. Thus, the turbulent kinetic spectra were studied. Before comparing with Kolmogorov's hypothesis, a line-probe was used to record fluctuating velocities that were transformed by FFT to calculate turbulent kinetic energy in spectral domain. Then, the magnitudes of the energy were calculated from the velocities of FFT results and their conjugates value. The discretization of the

line-probe and the amounts of samples were utilized to calculate the corresponding wavenumbers. Subsequently, a new spectral analysis method, wavelet transform has been well developed in the past few decades. The wavelet analysis was used in the dissertation to overcome the deficiencies of FFT, such as solving time and frequency domains simultaneously. In addition, the difference between wavelet transform and FFT is that the wavelets are localized in time and frequency domains but FFT is only localized in frequency domain [59]. Also, FFT is composed of sine and cosine functions, but wavelet transform can have infinity mother wavelets bases. Another analysis method named proper orthogonal decomposition (POD) was implemented for the simulation results because it is advantageous to filter out small signals. POD method is widely used to experimental results to study flow features and invisible flow patterns. The original signals are decomposed to eigenvalues and eigenvectors in the POD. Then, the signal is reconstructed by selecting different numbers of the eigenvalues, so the small signals are filtered out. The concept of POD method is similar to LES approaches. Wavelet analysis and the POD method were discussed more in the following sub-sections.

5.1.1 Wavelet analysis method

Spectral analyses were implemented to study the simulation results based on the temporal or spatial domains that were dependent on the sources of the results. For example, if the results are recorded at a certain time step, the analysis will be a wavenumber analysis. If the dataset is from a time series, the analysis will result in a frequency analysis. FFT and wavelet analyses are both useful for spatial and frequency analyses. Although Fourier analysis is convenient and simple to use, unfortunately, it can

be applied to only one domain (space-wavenumber or time-frequency) at a time. In order to overcome the defects, wavelet analysis is used to characterize turbulence. Wavelet transform was applied for analyzing results in this dissertation because it can handle results of high order dimensions simultaneously. Wavelet can provide more temporal and local details than FFT and can deal with rapidly changing signals [59].

For example, if the function ψ satisfies Eq. 5-1 and Eq. 5-2, ψ is considered as the mother wavelet.

$$\int_{-\infty}^{\infty}|\psi(t)|^2\,dt < \infty \qquad \text{(Eq. 5-1)}$$

$$C_\psi = 2\pi \int_{-\infty}^{\infty} \frac{|\Psi(\omega)|^2}{|\omega|} d\omega < \infty \qquad \text{(Eq. 5-2)}$$

where Ψ is the Fourier transform of ψ. Eq. 5-1 shows the finite energy condition. Eq. 5-2 give that $\Psi(0) = 0$ if $\Psi(\omega)$ is smooth. Then, the wavelet transform of a real signal is given by Eq. 5-3.

$$S(b, \mathrm{a}) = \frac{1}{\sqrt{a}} \int_{-\infty}^{\infty} \psi'\left(\frac{t-b}{a}\right) s(t)\,dt \qquad \text{(Eq. 5-3)}$$

where ψ' denotes the complex conjugate of ψ. The parameters b and a are the time shift and the scale of the analyzing wavelet, respectively. Assuming $\psi_{a,b}(t)$ is defined as Eq. 5-4.

$$\psi_{a,b}(t) = \frac{1}{\sqrt{a}} \psi\left(\frac{t-b}{a}\right) \qquad \text{(Eq. 5-4)}$$

Here, the wavelet transform of the real signal becomes as:

$$S(b, \mathrm{a}) = \int_{-\infty}^{\infty} \psi'_{a,b}(t) s(t)\,dt \qquad \text{(Eq. 5-5)}$$

Now, the original signal $s(t)$ is provided by the inverse transformation shown in Eq. 5-6.

$$s(t) = \frac{1}{C_\psi} \int_{-\infty}^{\infty} \int_{-\infty}^{\infty} S(b, \mathrm{a}) \psi_{a,b}(t) \frac{da\, db}{a^2} \qquad \text{(Eq. 5-6)}$$

MATLAB code has many choices of mother wavelet functions, such as Meyer wavelet, and Morlet wavelet [58]. Selecting suitable mother wavelet function is required to obtain reasonable results. The Continuous Wavelet Transform (CWT) in MATLAB code was used for the post analyses [58]. Different wavelet mother functions were used for the comparisons of frequency distributions in the air-ingress phenomenon and the OECD problem. Figure 18 shows examples of two different wavelet mother functions, the Meyer wavelet function and the Morlet wavelet function. The Morlet wavelet function using in MATLAB code is given in Eq. 5-7

$$\psi(x) = \mathrm{e}^{-x^2/2} \cos(5x) \qquad \text{(Eq. 5-7)}$$

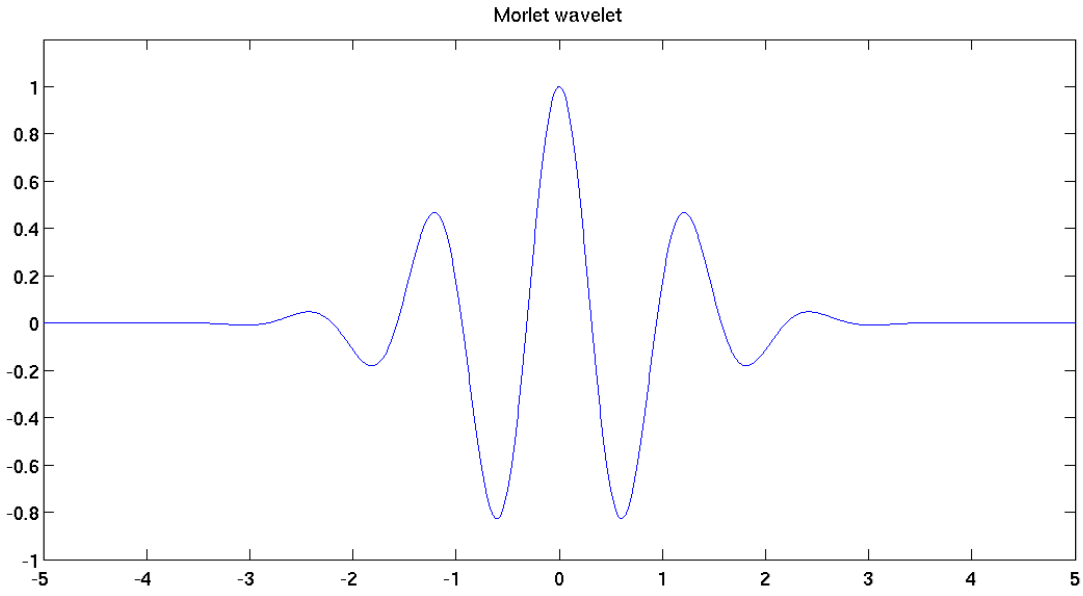

Figure 18. Examples of wavelet mother functions from 5 to -5 with 2048 points: (a) the Meyer wavelet functions, (b) the Morlet wavelet functions.

5.1.2 Proper orthogonal decomposition

The flow visualization technique is one of the primary techniques used to identify vortices within experimental flow fields. Particle image velocity (PIV) technique is used to obtain two- and three-dimensional flow fields, and DNS and LES method are utilized for computations of 3D flow fields. The POD method is introduced to help study turbulent velocity fields in the dissertation [61]. The concept of the POD method is to decompose the original signal into many modes with its eigenvectors and eigenvalues which are descended to find the principle directions of the datasets. New signals are reconstructed by selecting the numbers of the modes from the most important to the minimum required by the user. When the least eigenvalues are ignored, the reconstructed fields present the results with large flow patterns that are similar to those results resolved in LES approaches [60, 61]. Since this method can filter out small components and retain the relatively important components, POD helps study flow features and flow patterns [62].

For example, a two-dimensional (2D) dataset is given, and the velocity is expanded as Eq. 5-8.

$$u_i(\mathrm{x},\mathrm{t}) = \sum_k \sum_n a^{(k,n)}(t)\psi_i{}^{(k,n)}(x) \qquad \text{(Eq. 5-8)}$$

where a is the time-dependent coefficient corresponding to the orthogonal basis, ψ_i, for the *i*th component and is calculated from Eq. 5-9.

$$a^{(k,n)}(\mathrm{t}) = \frac{1}{L_{x_1}L_{x_2}} \iint u_i(\mathrm{x},\mathrm{t})\psi_i^{*(k,n)}(x)\,dx \qquad \text{(Eq. 5-9)}$$

where L_{x_1} and L_{x_2} are the extents of the domain in x_1 and x_2 directions, respectively. The (*) denotes the complex conjugate value. Assuming ψ_i is a product of a Fourier basis in x_1 and an inhomogeneous basis (ϕ_i) in x_2 given by Eq. 5-10.

$$\psi_i{}^{(k,n)}(x) = \phi_i{}^{(k,n)}(x_2) e^{\frac{i2\pi k x_1}{L_{x_1}}} \quad \text{(Eq. 5-10)}$$

where $i = \sqrt{-1}$ inside the exponential term. After doing this, a 2D problem is converted into a 1D POD problem. Here, a POD filter can be defined as a large-scale field and a small-scale field (Eq. 5-11).

$$u = \overline{u} + u'' \quad \text{(Eq. 5-11)}$$

where the filtered field is shown in Eq. 5-12.

$$\overline{u}_i(\mathrm{x}_1, \mathrm{x}_2) = \sum_{k=0}^{K} \sum_{n=0}^{N} H^{(k,n)} a^{(k,n)} \psi_i{}^{(k,n)}(x_1, x_2) \quad \text{(Eq. 5-12)}$$

In Eq. 5-12, $H^{(k,n)}$ is a filter characteristic function to amplify or attenuate the eigenvalues of each POD mode. If no amplification or attenuation is required, $H^{(k,n)}$ is simply 1.

Here, the filtered field can be expressed as Eq. 5-13.

$$\overline{u}_i(\mathrm{x}_1, \mathrm{x}_2) = \frac{1}{L_{x_1} L_{x_2}} \iint u_j(x_1', x_2')\, h_{ij}(x_1, x_2, x_1', x_2')\, dx_1' dx_2' \quad \text{(Eq. 5-13)}$$

where the kernel, h_{ij}, is given by Eq. 5-14.

$$h_{ij} = \sum_{k=0}^{K} \sum_{n=0}^{N} H^{(k,n)} \psi_i{}^{(k,n)}(x_1, x_2) \psi_j{}^{(k,n)*}(x_1, x_2) \quad \text{(Eq. 5-14)}$$

POD method is used to study the air-ingress phenomenon and the rod bundle problem. A MATLAB script was developed to use POD method.

5.2 Error and Uncertainty Analyses

The results of CFD predictions are sensitive to many factors, such as mesh sizes and iterative convergence issues. Especially, the mesh size affects significantly the final results of CFD efforts [66]. Verification and validation that are two concerns for quantifying simulation results provide accuracy with high confidence [67, 68]. Verification relies on solving correct governing equations and selecting proper assumptions and boundary conditions. Instead, a comparison using experimental data to assess computations is required for validation [66]. The final solutions of CFD simulations are calculated by using DNS which requires extremely large computations. In order to reduce computational resource, the Richardson extrapolation was used. The solution verification using Richardson Extrapolation and GCI provides error estimations of numerical uncertainty with a numerical error interval. Simulations with higher order of numerical scheme provide higher order of accuracy and less numerical errors. Due to Taylor-series expansions, low order numerical methods seem to have more numerical uncertainty than high order methods. The study of the mesh grid size independency was delivered by using Richardson Extrapolation and grid convergence index (GCI) method [67-70].

5.2.1 Richardson extrapolation

Richardson extrapolation is powerful to improve numerical convergence and to serve two practical purposes. First, the extrapolation results can be used to estimate the error due to mesh sizes. The other benefit is using the simulation results of different mesh sizes to extrapolate the actual values [66]. However, the estimated final values are

enormously affected by the incomplete iterative convergence errors. When a simulation does not reach convergence, the simulation results change significantly [66]. Using Taylor's expansions which are the most common methods can simply estimate answers with higher order of accuracy [69]. Richardson extrapolation was implemented to quantify the simulation results of the air ingress problem and the OECD rod bundle exercise [66, 69].

5.2.2 Grid convergence index method

Grid convergence index (GCI) is a study of approaching to quantification of uncertainty in CFD. Similar to any numerical methods, the higher order calculations of GCI have less uncertainty than the lower order calculations [70]. Applying GCI to the results of fine meshes is normally used to obtain the uncertainty with high confidence, but using coarse grids gives at least some certain level confidence of the uncertainty [70]. Besides applying to structure mesh grids, GCI has been developed for the use of unstructured mesh grids; therefore, GCI has become more common for the quantification of uncertainty in CFD publications [66]. Generally speaking, the second order accuracy is embedded in GUI working usually with Richardson Extrapolation to obtain whole information that contains the estimating value and the corresponding uncertainty [66].

5.2.3 Example calculations of Richardson extrapolation

At least three simulation sets with different mesh sizes are prepared to determine values of key variables for applying to Richardson Extrapolation and GCI. The approximate relative error, the estimated relative error of the extrapolations, and the uncertainty estimation are requirements for calculating GCI and the corresponding

uncertainty. Calculating a representative grid size of structured grids and unstructured grids that are both available for GCI is simply following the calculations as given in Eq. 5-15 and Eq. 5-16, respectively.

$$h = [(\Delta X_{max})(\Delta Y_{max})(\Delta Z_{max})]^{1/3} \quad \text{(Eq. 5-15)}$$

$$h = [(\sum_{i=1}^{N} \Delta V_i)/N]^{1/3} \quad \text{(Eq. 5-16)}$$

The grid refinement factors, r, that are defined as the ratio of two representative grid sizes are suggested to be greater than 1.3. The constant and non-constant r can both be applied to calculate the observed order (p), which is used for Richardson extrapolation and GCI. The calculations of the observed order (p) with constant or non-constant r are given by Eq. 5-17 and Eq. 5-18, respectively.

$$p_{const} = \frac{|\ln|\varepsilon_{32}/\varepsilon_{21}||}{\ln(r_{21})} \quad \text{(Eq. 5-17)}$$

$$p_{non-const} = \frac{|\ln|\varepsilon_{32}/\varepsilon_{21}|+q(p)|}{\ln(r_{21})} \quad \text{(Eq. 5-18)}$$

where ε_{32} and ε_{21} are absolute difference between two simulation results. r_{21} is the grid refinement factor of the second dataset to the first dataset. $q(p)$ is defined in Eq. 5-19.

$$q(p) = \ln\left(\frac{r_{21}^{p}-s}{r_{32}^{p}-s}\right) \quad \text{(Eq. 5-19)}$$

$$s \equiv 1 * sign(\varepsilon_{32}/\varepsilon_{21}) \quad \text{(Eq. 5-20)}$$

The observed order is used to calculate the extrapolated values of the unknown variable given by Eq. 5-21.

$$\phi_{ext}^{21} = \left(r_{21}^{p}\phi_1 - \phi_2\right)/\left(r_{21}^{p} - 1\right) \quad \text{(Eq. 5-21)}$$

Finally, the observed order, the approximate relative error, and the estimated relative error of the extrapolations are utilized for GCI that is further applied for calculating uncertainty (Eq. 5-22).

$$u_{numerical} = GCI/k \quad \text{(Eq. 5-22)}$$

where k defined as the error distribution is 1.15 for a shifted Gaussian and is 2 for a Gaussian distribution.

CHAPTER VI

RESULTS AND ANALYSIS

6.1 Section 1 – Air Ingress Phenomenon

The study of air ingress phenomena contained five sub-topics: the mesh size sensitivity study, two fluid pairs (gas-gas and liquid-liquid), two geometries (short and long pipe), the moving valve conditions (fully open and moving), and two turbulent models (RANS and LES). Table 4 lists the results of eight scenarios that were simulated and two experiments in the air ingress study. From Case 1-3, the mesh size sensitivity study was given. Case 3 and 4 were used for the valve moving comparison. The turbulent modeling comparison was simulated in Case 4 and 5. The effects of the pipe lengths were done in Case 5 and 6 and Case 7 and 8 with He-SF_6 and water-brine, respectively. Case 7 and 8 were the simulations representing the experiments. Case 9 and 10 were the experiments listed in Table 4.

Table 4. Lists of inner and outer maximum wave front velocity and the corresponding ratios of simulations in the air ingress problem.

Case	Mesh Size	Pipe	Valve	Turbulence	Inner Vel.	Outer Vel.	I/O Ratio	Fluid Pair
1	1.5 mm	Short	Fully Open	Realizable k-ε	0.955 m/s	1.112 m/s	85.9%	He-SF6
2	1.0 mm	Short	Fully Open	Realizable k-ε	0.944 m/s	1.104 m/s	85.5%	He-SF6
3	0.7 mm	Short	Fully Open	Realizable k-ε	0.924 m/s	1.099 m/s	84.1%	He-SF6
4	0.7 mm	Short	Moving	Realizable k-ε	0.699 m/s	0.900 m/s	77.7%	He-SF6
5	0.7 mm	Short	Moving	LES	0.723 m/s	0.905 m/s	79.9%	He-SF6
6	0.7 mm	Long	Moving	LES	0.881 m/s	1.071 m/s	82.3%	He-SF6
7	0.7 mm	Short	Moving	LES	0.134 m/s	0.168 m/s	79.8%	Water-Brine
8	0.7 mm	Long	Moving	LES	0.142 m/s	0.172 m/s	82.6%	Water-Brine
9	Experiment	Short	Moving	X	X	0.164 m/s		Water-Brine
10	Experiment	Long	Moving	X	X	0.168 m/s		Water-Brine
11	Theory	X	X	X		0.1604 m/s		Water-Brine

The comparisons of scenarios with different sub-topics were listed in Table 5 where, for example, the mesh size sensitivity study was listed as the first category. Two subsequent sub-sections discuss a liquid ingress phenomenon (Case 7-10) and a gas ingress phenomenon (Case 1-6), respectively.

Table 5. Comparisons between different cases.

Case Comparison	Inner Difference	Inner Ratio	Outer Difference	Outer Ratio
1, 2, & 3 (Mesh)	0.031 m/s	3.25%	0.013 m/s	1.17%
3 & 4 (Valve)	0.225 m/s	24.35%	0.199 m/s	18.11%
4 & 5 (Turbulent)	0.024 m/s	3.32%	0.005 m/s	0.55%
5 & 6 (Pipe[1])	0.158 m/s	17.93%	0.166 m/s	15.50%
7 & 8 (Pipe[2])	0.008 m/s	5.63%	0.004 m/s	2.33%
9 & 10 (Pipe[3])	X	X	0.004 m/s	2.38%
7 & 9 (*)	X	X	0.004 m/s	2.38%
8 & 10 (*)	X	X	0.004 m/s	2.33%

1: With He-SF_6 fluid pairs
2: With water-brine fluid pairs
3: Comparison for the experiments
*: Comparison for the experiments and simulations

6.1.1 Grid sensitivity study

Numerical diffusion occurs in discretizing differential equations, such as the Navier-Stokes equations. To achieve high simulation fidelity, the mesh size sensitivity study is delivered to minimize the numerical diffusion and to determine the appropriate mesh size. The Richardson extrapolation is introduced to accomplish the goal of the grid sensitivity study and the corresponding uncertainty.

Starting with the mesh size sensitivity study, three simulations with the mesh sizes of 1.5 mm, 1.0 mm, and 0.7 mm were listed as Case 1, Case 2, and Case 3 in Table 4. The fully open valve condition with unsteady Realizable k-ε model, the short pipe geometry, and He-SF6 fluid pairs were used for the grid sensitivity study [65]. The extrapolated results and corresponding relative errors were calculated to confirm that the reliable results were obtained. The results of the three mesh sizes are shown in Figure 19. Table 4 shows that the relative difference is 3.25% and 1.17% for the inner pipe and the outer pipe, respectively. Figure 20 and Figure 21 show the velocity magnitudes and relative errors for the extrapolations and the simulations with different mesh sizes. The definitions of calculated relative errors were seen in Eq. 6-1.

$$e_{ext}^{21} = \left|\frac{\phi_{ext}^{21} - \phi_1}{\phi_{ext}^{21}}\right| \quad \text{(Eq. 6-1)}$$

It was obvious that three simulation results gave the relative errors within 4% (Figure 20). The 1.5 mm mesh size gave better predictions with the Richardson Extrapolation than the 1.0 mm simulation which predicted large discrepancy with the other simulations and the extrapolation. The results with 0.7 mm mesh size presented the best agreement with the Richardson Extrapolation within 1% of relative errors. Although the results of 1.5 mm and 1.0 mm showed similar calculations and had the relative errors within 4%, the 0.7 mm mesh size showed the best predictions in three simulations. The 0.7 mm mesh size was chosen for the further simulations in this air ingress problem.

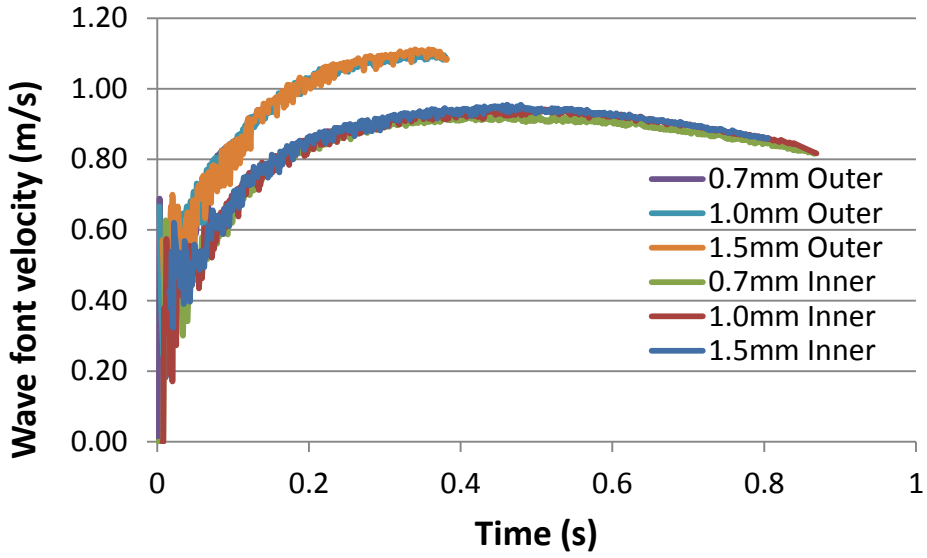

Figure 19. Comparison of wave front velocity profile of the mesh sensitivity study.

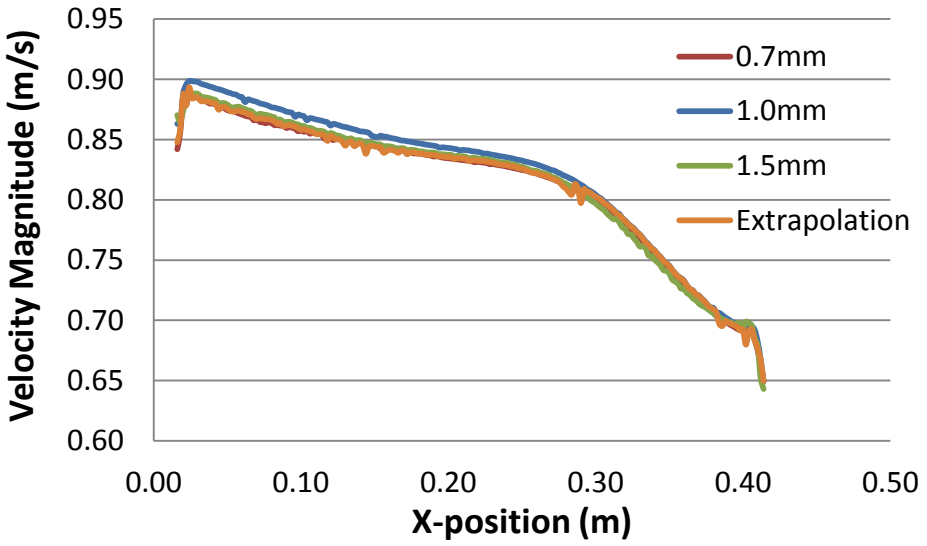

Figure 20. Velocity magnitudes of the fluid along with x-axis for 200 locations in the simulations and the Richardson Extrapolation.

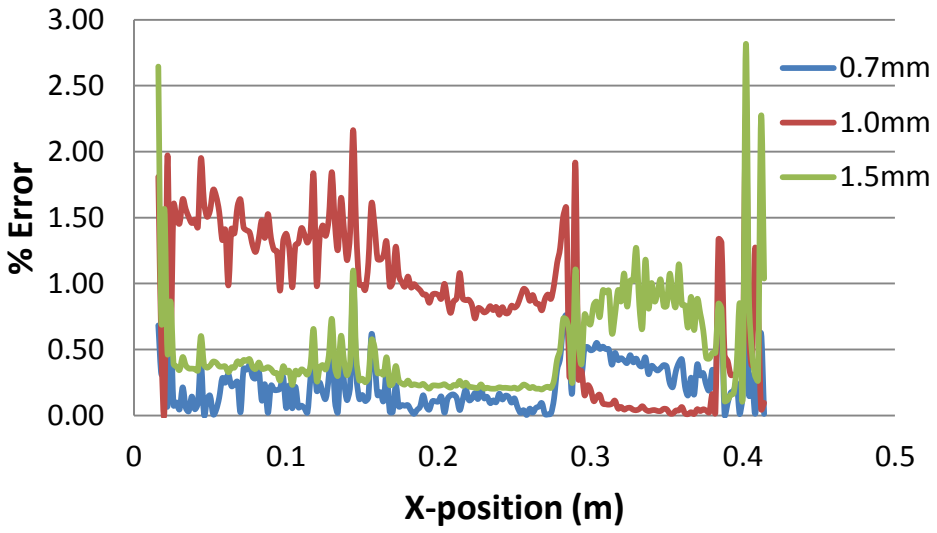

Figure 21. Relative errors comparing with the extrapolations along with x-axis for 200 locations in three mesh sizes.

6.1.2 Water ingress phenomenon

Two water-brine cases using different pipe length were simulated as Case 7 and 8 listed in Table 4. The finest mesh size (0.7 mm), the LES turbulent model, and two geometries (long and short pipes) were used in the water-brine simulations. The evolutions of the wave front velocity in the co-axial pipes and in the lower plenum are shown in Figure 22 and Figure 23, respectively. The maximum wave front velocities were defined as the maximum values during the velocity evolution of the pipe. The maximum inner velocities were 0.134 m/s and 0.142 m/s for the short and the long pipes, respectively.

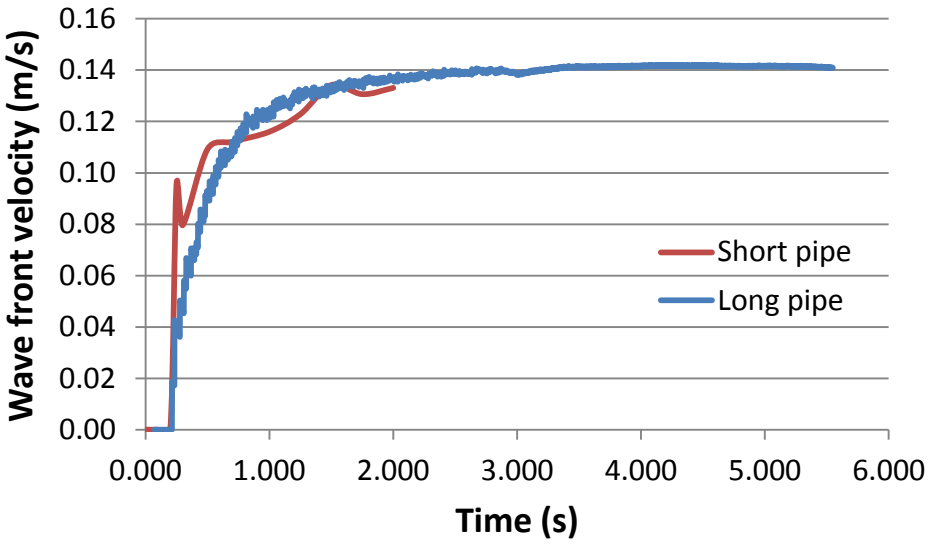

Figure 22. The evolutions of the wave front velocity in the inner pipe for the simulations with different pipe lengths.

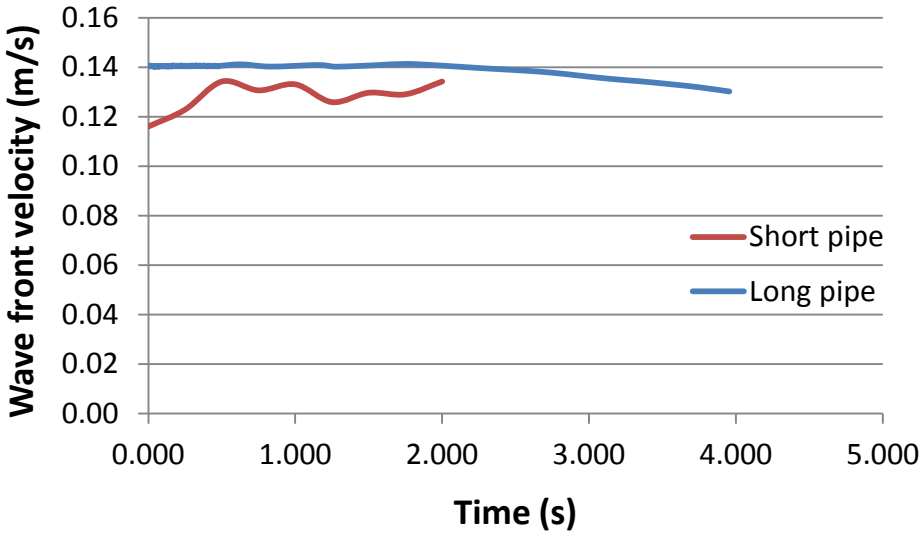

Figure 23. The evolutions of the spreading rate in the lower plenum for the simulations with different pipe lengths.

In these simulations, the maximum wave front velocities were considered as the terminal velocities. The maximum wave front velocities of the outer pipe were 0.168 m/s and 0.172 m/s for the short and the long geometries, respectively. The absolute difference was simply calculated as 0.008 m/s and 0.004 m/s for inner and outer pipes by using Eq. 6-2. The definitions of calculated relative difference were given in Eq. 6-3. According to Benjamin's theorem, the wave front velocity is related to the density ratio and the height of the fluid (or the height of the pipe) [5]. Thus, the theoretical terminal velocity is calculated as 0.1604 m/s for the outer pipe. The simulation results gave the relative error of 4.74% for the short pipe case where the experimental data showed the relative error of 2.24%.

$$\begin{cases} \Delta V_{inner} = V_{inner}(long) - V_{inner}(short) \\ \Delta V_{outer} = V_{outer}(long) - V_{outer}(short) \end{cases} \quad \text{(Eq. 6-2)}$$

$$\begin{cases} \frac{\Delta V_{inner}}{V_{inner}(long)} = 100\% \frac{V_{inner}(long) - V_{inner}(short)}{V_{inner}(long)} \\ \frac{\Delta V_{outer}}{V_{outer}(long)} = 100\% \frac{V_{outer}(long) - V_{outer}(short)}{V_{outer}(long)} \end{cases} \quad \text{(Eq. 6-3)}$$

The pipe lengths from the valve to the light fluid tank were used to simulate the distance from the break locations to the reactor vessel. After simulations, the geometry effects from changing a short pipe to a long pipe showed a slight enhancement of the maximum wave front velocity. Theoretically, the maximum velocity is affected by the diameter of the pipe and the density ratio of the fluid pair, so it is regarded to have a constant maximum velocity. The maximum wave front velocities of the inner and the outer pipes increased with the magnitudes of 5.63% and 2.33%, respectively. According to Eq. 6-4, the ratio of the maximum velocity of the inner pipe to the outer pipe for the

short and the long geometries were 79.8% and 82.6%, respectively. Comparing with the theoretical value of 0.1604m/s. the simulation result and the experimental data provided 7.23% and 4.74%, respectively.

$$Velocity\ Ratio = 100\% \frac{V_{inner}}{V_{outer}} \quad \text{(Eq. 6-4)}$$

Based on the experimental data, the wave front velocities of the outer pipe were 0.164 m/s and 0.168 m/s for the short and the long geometries (Table 4). The wave front velocity of the inner pipe was difficult to be analyzed because it was challenging to distinguish the inner wave fronts. Figure 24 shows that the inner wave front is difficult to be measured.

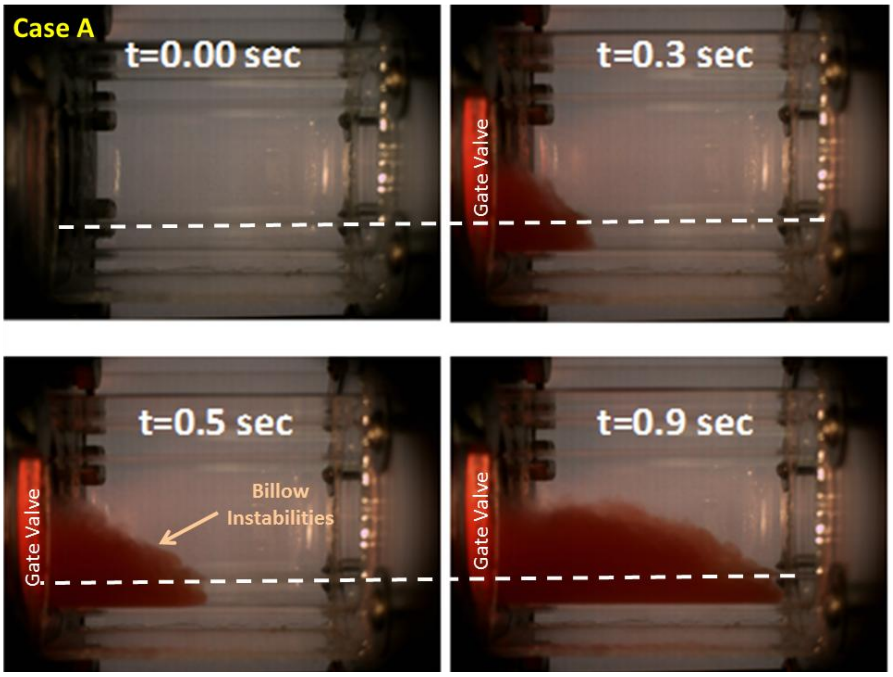

Figure 24. Examples of experimental snapshots for the gravity-current propagation of the water-brine scenario with the short pipe geometry [39].

Depending on the experimental data, the relative difference of the outer wave front velocities between the short and long pipes is 2.38% (Eq. 6-3). In other words, the maximum wave front velocities in the experiments increased with the magnitudes of 2.38% which was approximately the same as the value obtained by the simulations. These results were summarized in Table 4 and Table 5.

The wave front behaviors of the outer pipe were shown in Figure 25 and Figure 26. In both short pipe and long pipe comparisons, the simulations predicted lower values for the wave front locations and velocities than the experimental data. The initial rapid burst was observed in both short pipe and long pipe cases of the experiments and the simulations. Even though the experimental data showed more noticeable initial burst than those of the simulations, the terminal velocities of the wave fronts between experiments and simulations did not show significant difference. Figure 25 (b) shows that the wave front velocity from the experiments suddenly jumps to a peak of 0.242 m/s after the valve was removed. The wave front velocity, then, rapidly decreased to the terminal velocity of 0.164 m/s after approximately 0.7 seconds. On the other hand, the wave front velocity of the simulations shows two plateaus in Figure 25 (b). The wave front velocity from the simulations jumped to a value of 0.120 m/s which was half of the experimental value and remained approximately constant till the valve fully open in the simulation. After the valve was fully open, the simulation velocity rapidly accelerated to the terminal velocity of 0.168 m/s and remained approximately constant. The initial rapid burst appeared in the long pipe scenario of the experiments in Figure 26 (b), and rapidly decreased as the same phenomenon in the short pipe scenario.

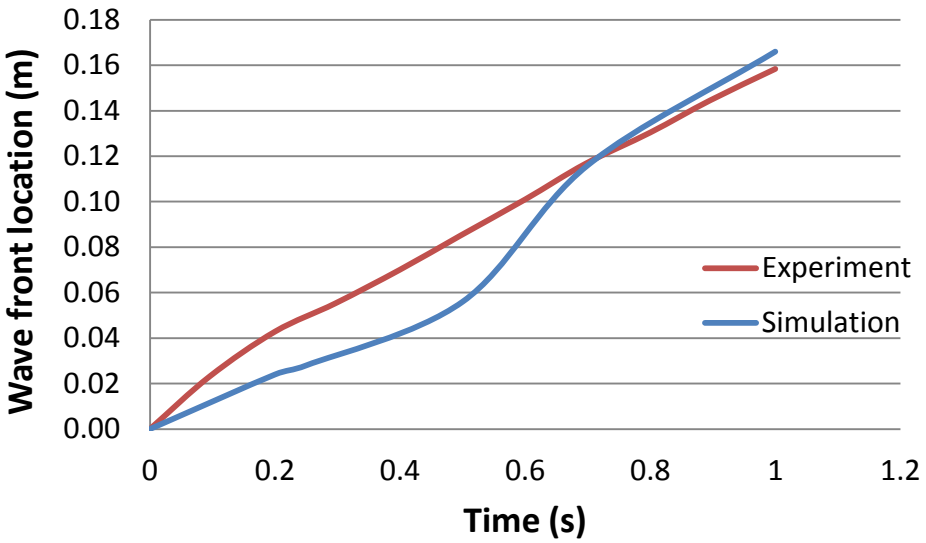

(a)

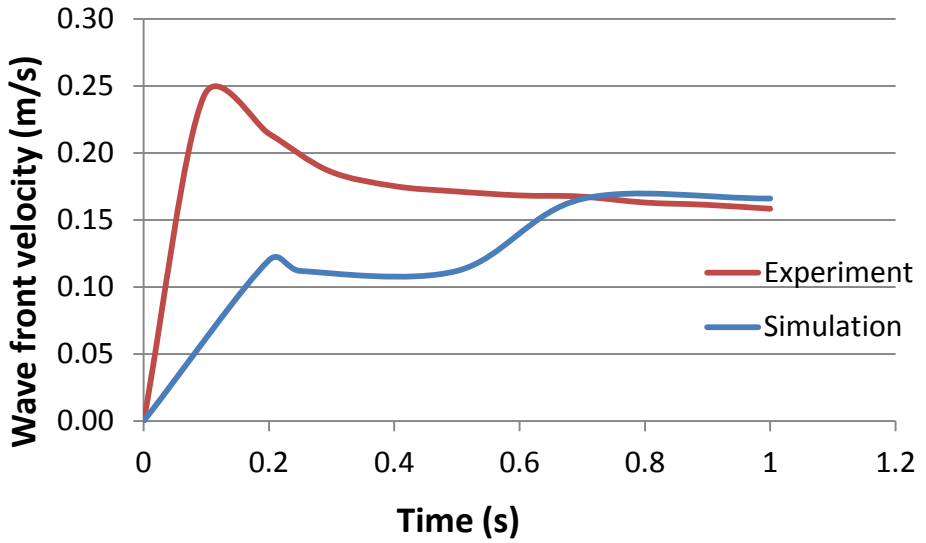

(b)

Figure 25. Results of the outer wave fronts in the short pipe geometry between simulations and experiments. (a) wave front locations; (b) wave front velocities.

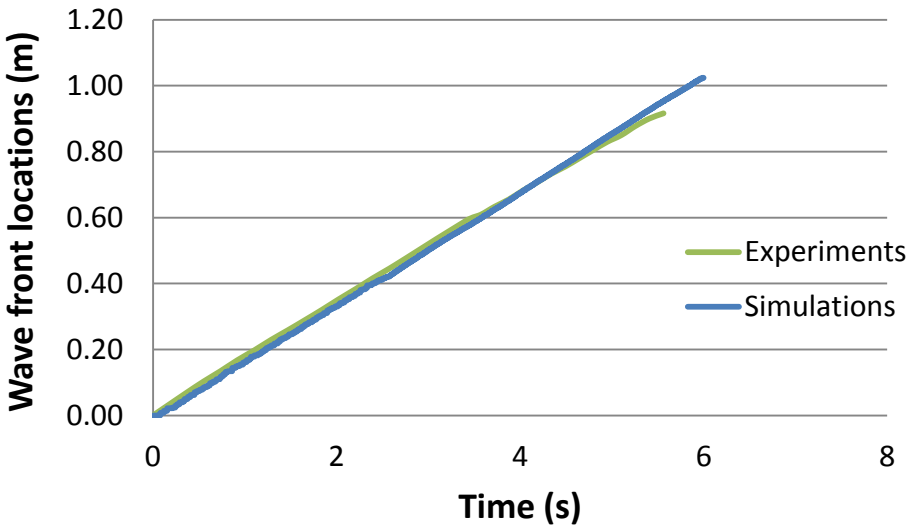

(a)

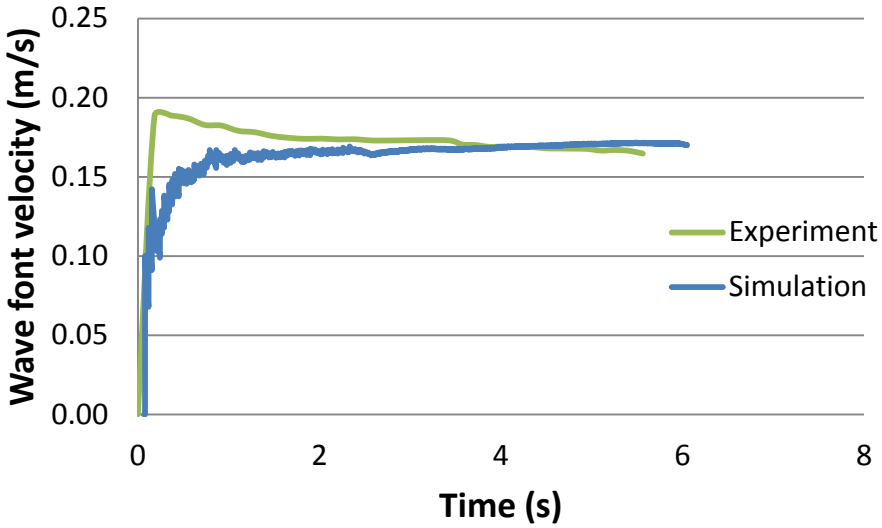

(b)

Figure 26. Results of the outer wave fronts in the long pipe geometry between simulations and experiments. (a) wave front locations; (b) wave front velocities.

It took longer for the heavy fluids to reach terminal velocities for both experiment and simulation in the long pipe scenario. These discrepancies between the experiment and the simulation during the time that the valve was opened were probably caused by the moving valve assumption. It was believed that the valve was moved faster at the beginning in the experiments than the simulations where the valve was set to move with a constant speed. Assuming the valve moved with a constant speed was probably an appropriate approximation because the valve information obtained from the experiment was the time that the valve was opened. Further analyses were required to examine this assumption. Eq. 6-5 and Eq. 6-6 were used to calculate the absolute difference and the relative difference between the simulation results and experimental data.

The comparison gave the difference within 2.4% for the short and the long pipes cases listed in Table 5. Moreover, the wave fronts in the simulation finally reached the same locations and velocities as those in the experiment. This showed that it was appropriate to assume the valve to move with a constant speed, although the discrepancies were shown at the initial state. As a result, this assumption of steadily moving valve was applicable for the gas-gas simulations.

$$\Delta V_{outer} = V_{outer}(simulation) - V_{outer}(experiment) \quad \text{(Eq. 6-5)}$$

$$\frac{\Delta V_{outer}}{V_{outer}(simulation)} = 100\% \frac{V_{outer}(simulation) - V_{outer}(experiment)}{V_{outer}(simulation)} \quad \text{(Eq. 6-6)}$$

Fast Fourier Transform (FFT) was used to analyze the frequencies in the air ingress phenomenon. The line-probes of the simulations were used to plot FFT spectra. The frequency based power spectra of the wave front velocity evolution were analyzed in this section.

Figure 27 and Figure 28 show the frequency power spectra for the cases of the short pipe and the long pipe, respectively. The time step in both cases was one millisecond (1ms). The samples of the short and the long pipes were 512 and 4096, respectively. Thus, the frequencies in FFT were calculated as 1.953 to 500 (1/s) for the short pipe case and as 0.244 to 500 (1/s) for the long pipe scenario. Both figures show that the significant frequencies of the flow evolutions were approximately less than 4Hz for different locations in the liquid-liquid ingress phenomenon.

6.1.3 Gas ingress phenomenon

The grid independent study proved that the 0.7 mm mesh size was enough fine to obtain high fidelity simulation result in Section 6.1.1. The moving valve assumption was proved to be a good agreement with the experimental data in Section 6.1.2. Consequently, the turbulent models were used to study the difference between the unsteady RANS and the LES approaches as the Case 4 and Case 5 listed in Table 4 whose corresponding comparisons (4&5) could be seen in Table 5. Two helium-SF6 simulations, with the same geometry and mesh size (0.7 mm) but using different turbulence models (Realizable k-ε and LES) are discussed here. In the simulations, a moving valve was modeled to represent the experiment including a valve opening time of 0.534 seconds.

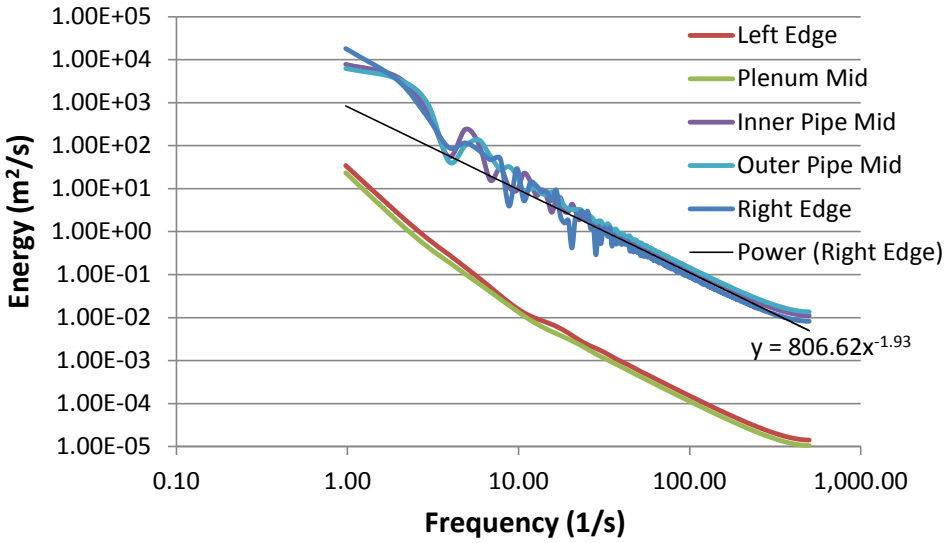

Figure 27. Frequency power spectra of the velocity evolutions at certain locations with water-brine fluids, the LES model, short pipe, and 0.7 mm mesh size.

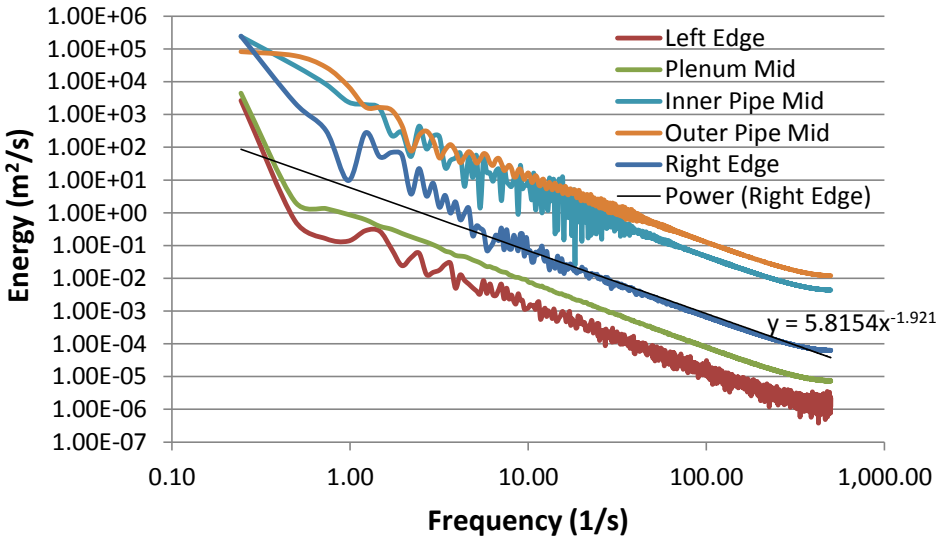

Figure 28. Frequency power spectra of the velocity evolutions at certain locations with water-brine fluids, the LES model, long pipe, and 0.7 mm mesh size.

The wave front velocity evolutions of the inner and outer pipes are shown in Figure 29 and Figure 30. The LES result predicted a larger maximum wave front velocity than the unsteady Realizable k-ε model for the inner and the outer pipes. In the inner pipes, the LES and the Realizable k-ε models showed the maximum velocities of 0.723m/s and 0.699m/s. In the outer pipes, the magnitudes of the maximum wave front velocity from the LES and the Realizable k-ε predictions were 0.905m/s and 0.900m/s, respectively. The values are listed as the Case 4 and Case 5 in Table 4. Through Eq. 6-7, the absolute differences between the two models were 0.024m/s and 0.005m/s for the inner pipe and the outer pipe, respectively. The results obtained through LES simulations provided a slightly different value of 3.32% from that of the Realizable k-ε simulations for the inner pipe and a different value of 0.44% for the outer pipe (Eq. 6-8). The values are listed in Table 2 as the comparison 4-5. This shows that the simulation results have good agreements with the experimental data in the liquid-liquid scenario. Based on the results, the ratio of maximum wave front velocity of the inner pipe to the outer pipe (Eq. 6-4) was 79.9% for the LES approach, and the value was 77.7% for the Realizable k-ε model.

$$\begin{cases} \Delta V_{inner} = V_{inner}(LES) - V_{inner}(k-\varepsilon) \\ \Delta V_{outer} = V_{outer}(LES) - V_{outer}(k-\varepsilon) \end{cases} \quad \text{(Eq. 6-7)}$$

$$\begin{cases} \frac{\Delta V_{inner}}{V_{inner}(k-\varepsilon)} = 100\% \frac{V_{inner}(LES) - V_{inner}(k-\varepsilon)}{V_{inner}(k-\varepsilon)} \\ \frac{\Delta V_{outer}}{V_{outer}(k-\varepsilon)} = 100\% \frac{V_{outer}(LES) - V_{outer}(k-\varepsilon)}{V_{outer}(k-\varepsilon)} \end{cases} \quad \text{(Eq. 6-8)}$$

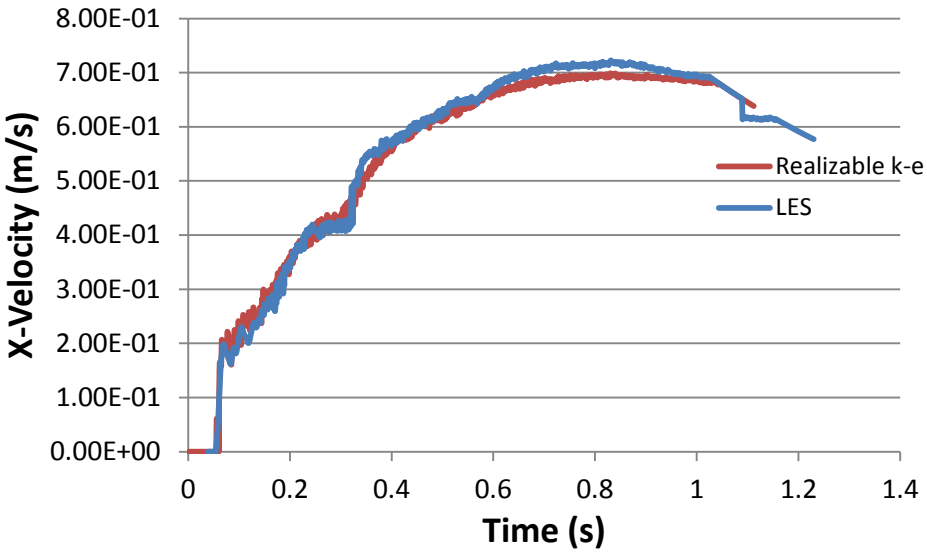

Figure 29. Wave front velocity evolution in the inner pipe for two turbulent models in 0.7 mm mesh size.

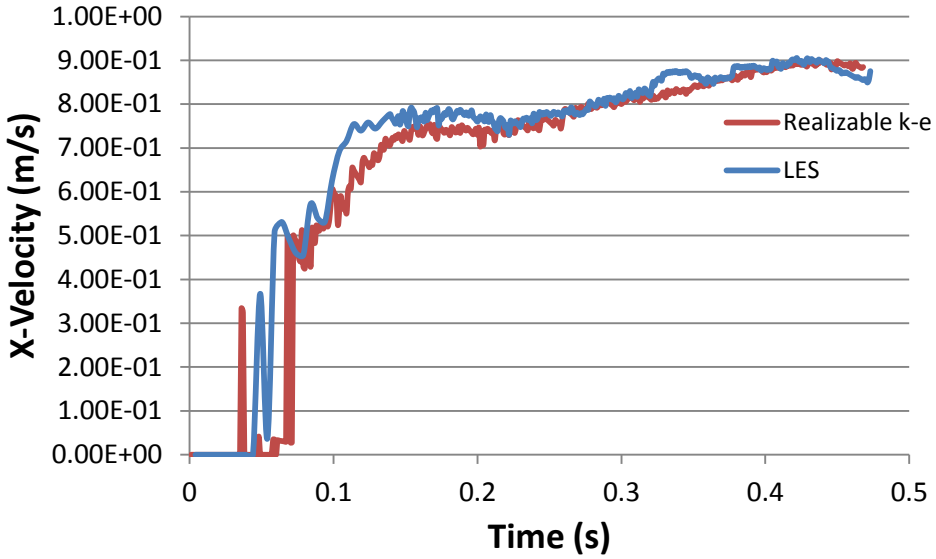

Figure 30. Wave front velocity evolution in the outer pipe for two turbulent models in 0.7 mm mesh size.

The FFT analysis was used to create energy spectra to analyze the results of both LES and RANS simulations. For the frequency based spectra, a certain location is fixed, and the time-series velocities are recorded. The magnitudes of the energy were calculated from the results of Fourier transform and its conjugates value. Five locations were selected from the two line probes to compare the energy spectra of LES approaches with those of RANS model. Figure 31 and Figure 32 show the frequency based energy spectra in log-log scale. The FFT results of the Realizable k-ε model were similar to the LES predictions. The significant frequencies were approximately less than 5Hz for both turbulent models. The smallest resolving frequency in the figure depended on the total number of the samples, and the largest resolving frequency was affected by the total samples or time steps. For example, the time step was 1 millisecond with the total number of 512 samples in the LES case; therefore, the frequency range was from 1.9531 Hz to 500 Hz. In the RANS simulation, the time step was 1 millisecond with a total number of 1024 samples, so the frequency range was from 0.9766 Hz to 500 Hz.

It should be mentioned that the moving valve is not included in the set of the grid independent study. This was assumed to be acceptable as the purpose of these particular simulations were to determine the size where the mesh independence had been reached for the co-annular duct. The scenario of the finest mesh size had been performed with and without the moving valve to determine the effect on the velocity profile and ingress velocities. Two He-SF_6 simulations were discussed in this paragraph as Case 3 and Case 4 in Table 4. The difference between Case 3 and Case 4 was the moving valve conditions.

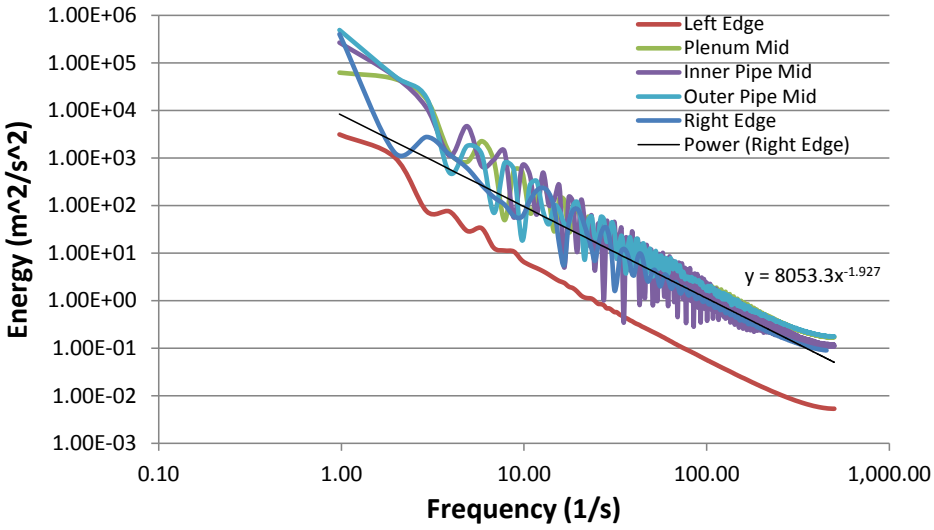

Figure 31. Frequency power spectra of the velocity evolutions at certain locations with He-SF_6 fluids, the Realizable k-ε model, short pipe, and 0.7 mm mesh size.

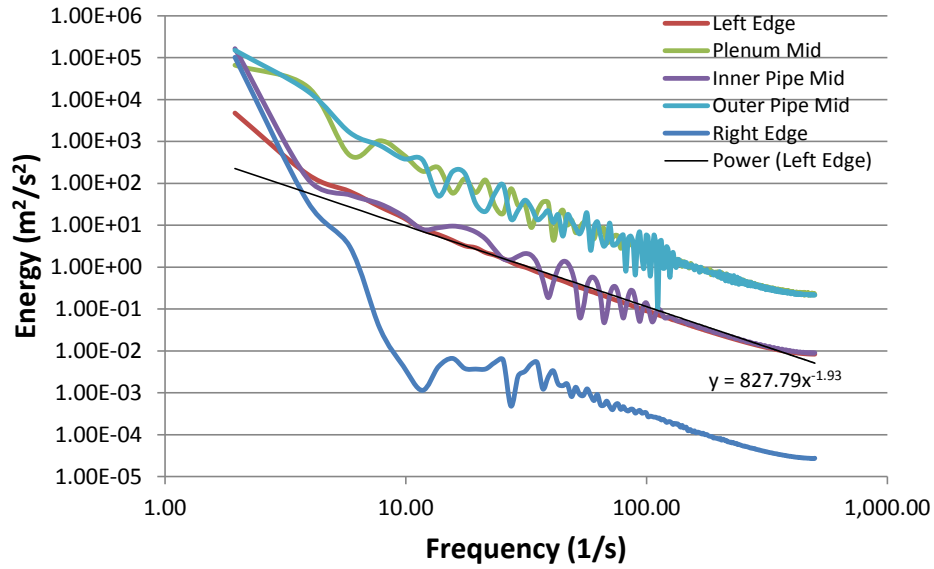

Figure 32. Frequency power spectra of the velocity evolutions at certain locations with He-SF_6 fluids, the LES model, short pipe, and 0.7 mm mesh size.

The fully open valve was assumed as the initial condition for Case 3, and the valve opened with a constant velocity was implemented for Case 4. The simulation and comparison results were seen in Table 4 and Table 5. From Case 3 of Table 4, the maximum wave front velocities of the inner and the outer pipe were 0.924m/s and 1.099m/s, respectively. The scenario with the moving valve predicted the inner and the outer wave front velocity of 0.696 m/s and 0.896 m/s, respectively. Based on the results, the ratio of the maximum velocity between the inner and the outer pipes is 84.1% for the fully open valve (Case 3). The ratio of the maximum wave front velocity of the inner pipe to the outer pipe was 77.7% (Eq. 6-4) for Case 4.

From Eq. 6-9, the absolute difference between the simulations (with and without the moving valve) was 0.225 m/s and 0.199 m/s for the inner pipe and the outer pipe, respectively. From Eq. 6-10, the relative differences of the wave front velocities for the inner and the outer pipes were calculated as 24.35% and 18.11%, respectively. These calculations are listed in Table 5. For the pipe length study, the difference in the water-brine simulations was not as significant as that in the He-SF_6 simulations.

$$\begin{cases} \Delta V_{inner} = V_{inner}(no\ valve) - V_{inner}(with\ valve) \\ \Delta V_{outer} = V_{outer}(no\ valve) - V_{outer}(with\ valve) \end{cases} \quad \text{(Eq. 6-9)}$$

$$\begin{cases} \frac{\Delta V_{inner}}{V_{inner}(no\ valve)} = 100\% \frac{V_{inner}(no\ valve) - V_{inner}(with\ valve)}{V_{inner}(no\ valve)} \\ \frac{\Delta V_{outer}}{V_{outer}(no\ valve)} = 100\% \frac{V_{outer}(no\ valve) - V_{outer}(with\ valve)}{V_{outer}(no\ valve)} \end{cases} \quad \text{(Eq. 6-10)}$$

6.1.4 Wavelet analysis

The wavelet analyses were used to further analyze the simulation results. The simulation results of the gas-gas scenario with the long pipe geometry were used for the

wavelet analyses because the temporal resolution was better. The Morlet mother wavelet function was implemented to study air-ingress phenomenon. Figure 33 gives an example of the instantaneous profile of the SF_6 volume fraction. It was clear that more turbulence appeared to the wave fronts than the flow away from the wave head. The flow far away from the wave fronts was assumed to simply transport kinetic energy to the wave fronts in the large-frequency scales (or low frequencies). However, the low frequencies may contain other effects (e.g., the buoyancy frequency that will be discussed later in this section). Since it was inferred that the wave front head contained complex phenomena of flow transporting and energy cascading simultaneously, the wavelet analysis was used to help understand more information of the air-ingress phenomenon. Similarly, few positions were chosen for the 1D wavelet analysis. The Morlet mother function was applied for the 1D continuous transform. The results of continuous wavelet transform (CWT) with the corresponding velocity magnitude profiles are shown in Figure 34 and Figure 35. The decompositions in Figure 34 show slight difference of the dominant frequencies for different positions. The dominant frequency was approximately 1.7 Hz at the position near the valve and the center of the outer line-probe, and it was 3 Hz for the position at the left edge of the outer line-probe with a significantly secondary frequency as approximately 8 Hz. Figure 35 shows that the dominant frequency was approximately 2 Hz for the position close to the valve in the inner line-probe and approximately 2.4 Hz for the position at the entrance of the light fluid tank and the left edge of the inner line-probe. Three positions had secondary frequencies of 4 Hz and 8 Hz.

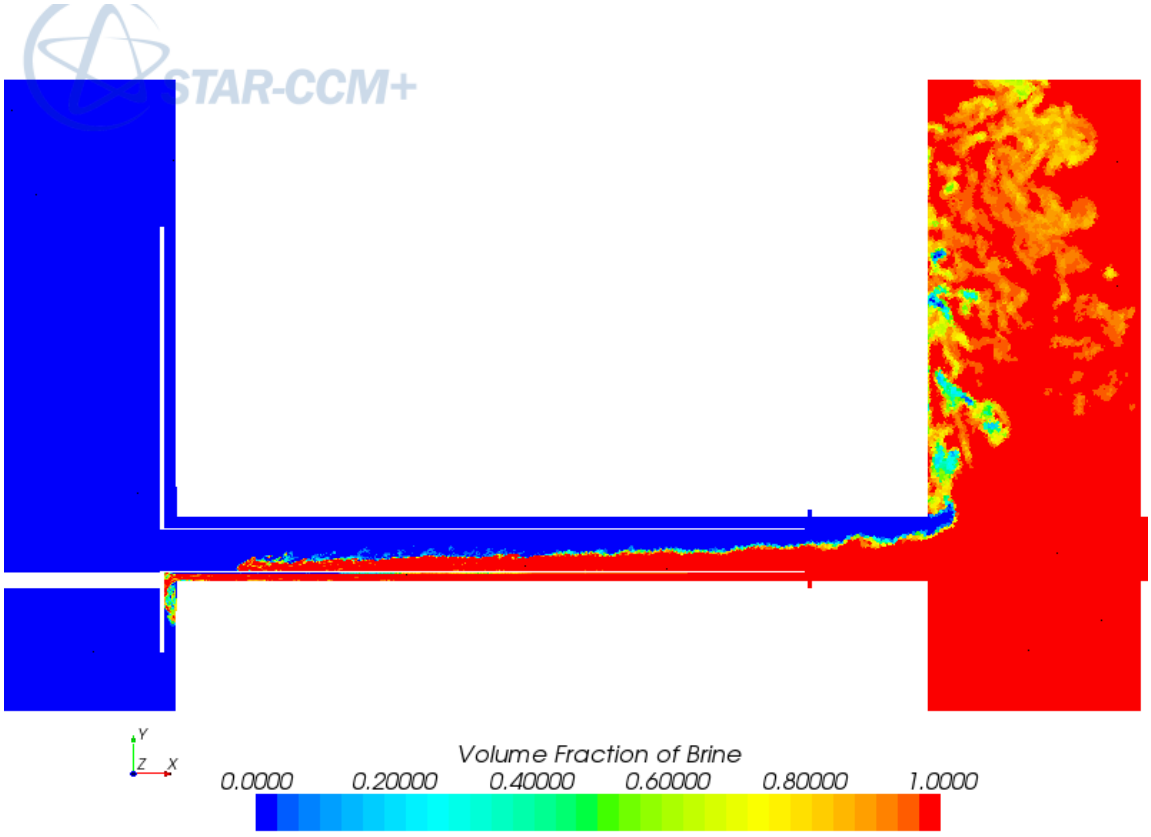

Figure 33. An example of volume fraction of Brine at the 6479th time step.

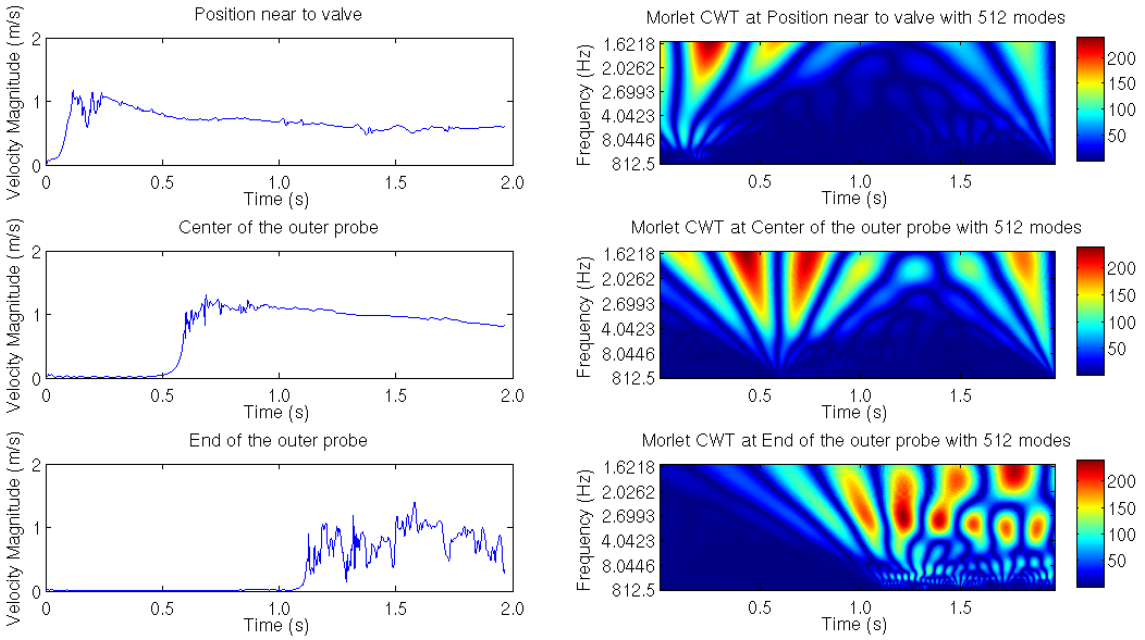

Figure 34. Instantaneous velocity magnitude signals from the outer line-probe of the long-pipe simulation results for the certain positions and their 1D continuous transform with using Morlet mother wavelet with 512 modes.

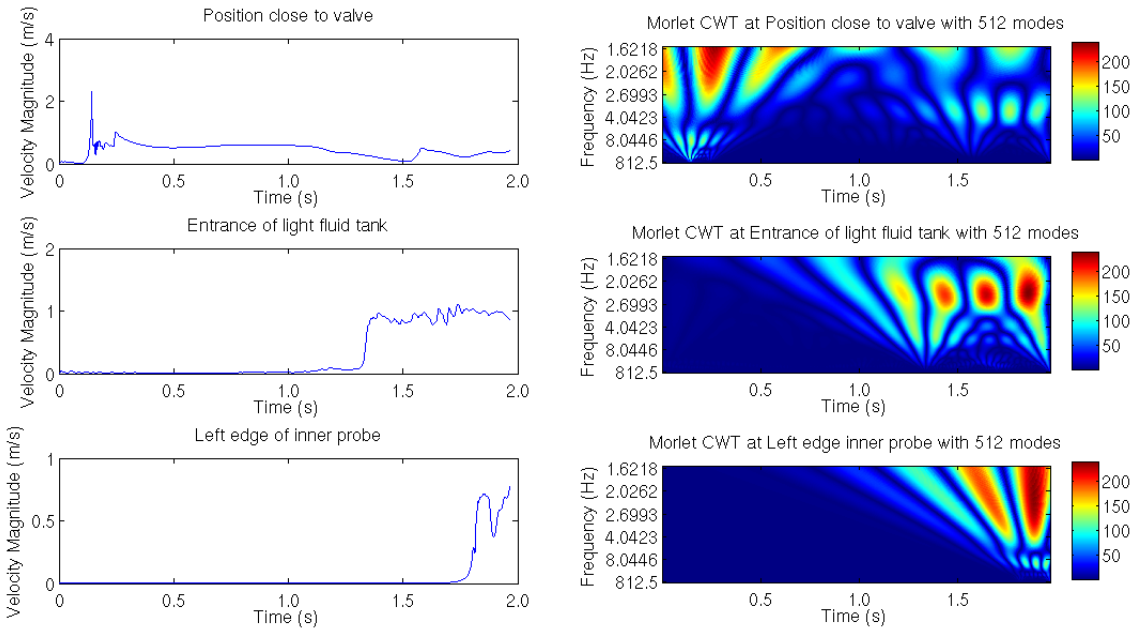

Figure 35. Instantaneous velocity magnitude signals from the inner line-probe of the long-pipe simulation results for the certain positions and their 1D continuous transform with using Morlet mother wavelet with 512 modes.

In order to study the effects from the number of total modes used in the wavelet analysis, the numbers of the modes from 32 to 1024 were implemented for the 1D Morlet CWT shown in Figure 36. It was obvious that the more modes were used to decompose the signal, the smaller frequencies were able to be analyzed. In the results of using 32 modes of Morlet mother function, the larger frequencies were unable to capture any signals. The decomposed signals for these modes were indistinct to provide dominant frequency of the flow. The comparisons showed that the approximately 6 Hz as the dominant frequency from 128 modes was the secondary frequency presented in the results from 256 modes. Similarly, the results of using 512 modes contained the secondary frequencies of 6 Hz and showed approximately 2 Hz as its dominant frequency. When 1024 modes were selected for the 1D continuous transform, the previously secondary frequency of 6 Hz was hardly observed. Instead, the 2 Hz frequency became the secondary dominant frequency in the 1D Morlet CWT with 1024 modes where the dominant frequency was approximately 0.9 Hz. As the total number of modes increases, the dominant frequency decreases (Figure 36).

The Brunt-Vaisala frequency, or buoyancy frequency, is given in Eq. 6-11.

$$N \equiv \sqrt{-\frac{g}{\rho}\frac{d\rho}{dz}} \qquad \text{(Eq. 6-11)}$$

where ρ is potential density. If the density gradient is negative, the instability at the interface between two fluids will become oscillating solutions. However, if the density gradient is positive, the stratification will become unstable. From Eq. 6-11, the frequency was calculated as approximately 2.34 Hz at the end of the outer line-probe, or the left edge of the light fluid tank. The frequency was very close to the value (2.4 Hz)

observed from the 1D Morlet wavelet analysis. The decomposition for this position in Figure 36 with 512 modes or 1024 modes confirmed this presence of a frequency in this range between times 1.2 s and 1.85 s.

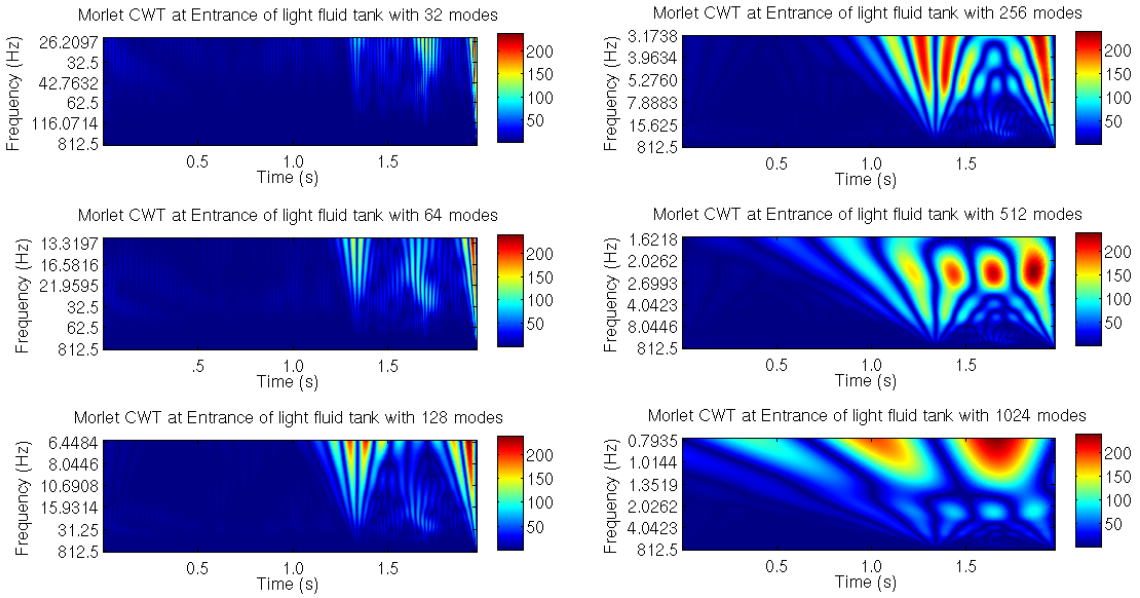

Figure 36. 1D Morlet CWT at the entrance of the light fluid tank with different number of modes from 32 to 1024.

6.1.5 POD method analysis

A plane cross-section shown in Figure 8 was utilized to extract results for the transient study with approximately 2 seconds. The LES results of approximately 2 seconds were used as the original modes of the database with a spatial resolution of 0.7 mm and a temporal resolution of one millisecond (1ms). 80 modes were selected to reconstruct the signal for comparisons with the original LES results. Generally, the first

mode of POD indicates the mean flow profile and contains the most of the kinetic energy. The air ingress phenomenon is a strongly transient scenario, so the first mode may not have enough strong influences on the flow behaviors. Figure 37 shows the accumulation and the percentage of the kinetic energy of the flow for each mode. The first mode in this study contained the 65.2% of kinetic energy of the flow. The 99.1% of the kinetic energy of the flow was covered by the first 80 modes. As described in Section 5.1.2, POD can help filter information of small scales from the original signals and retain the main information of large scales. Unfortunately, the reconstructions were limited to obtain clear results for POD method because the air-ingress phenomenon was a strongly transient scenario. Figure 38 illustrates the example that the POD method provides limit efforts even though the total number of the modes used for the reconstruction is reduced.

The signals in Figure 38 were extracted within the height of the wave front head (approximately 3 mm) since the wave front was considered to have the most information. However, it was obvious that the reconstructions presented rarely provide useful comparisons with the original LES results. It can be inferred that the wave front head contain many features with large scales which make complex flow patterns at the wave front head distinguish from the original LES results. The mixing mechanism occurring near the wave front head resulted from the heavy fluid intrusions. The Kelvin-Helmholtz instability at the interface was caused by density difference or density gradient. Subsequently, the next study was focus on the interface of two fluids.

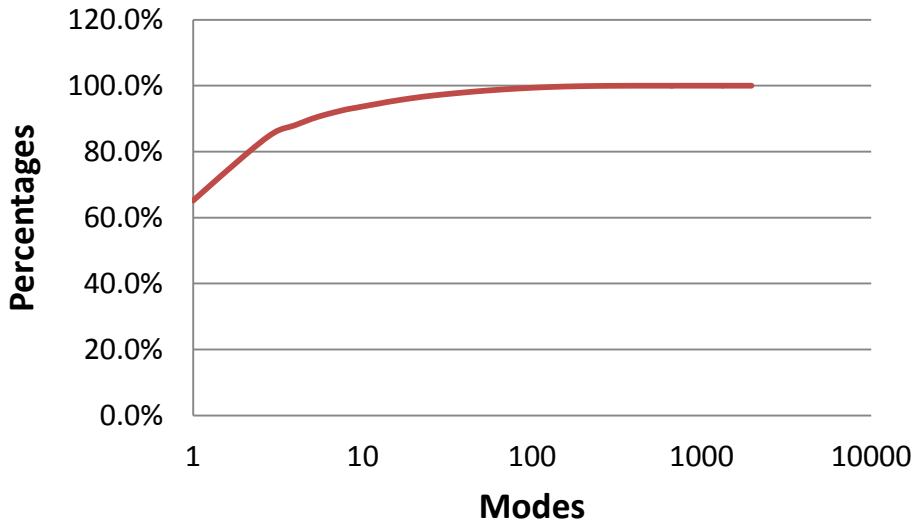

(a)

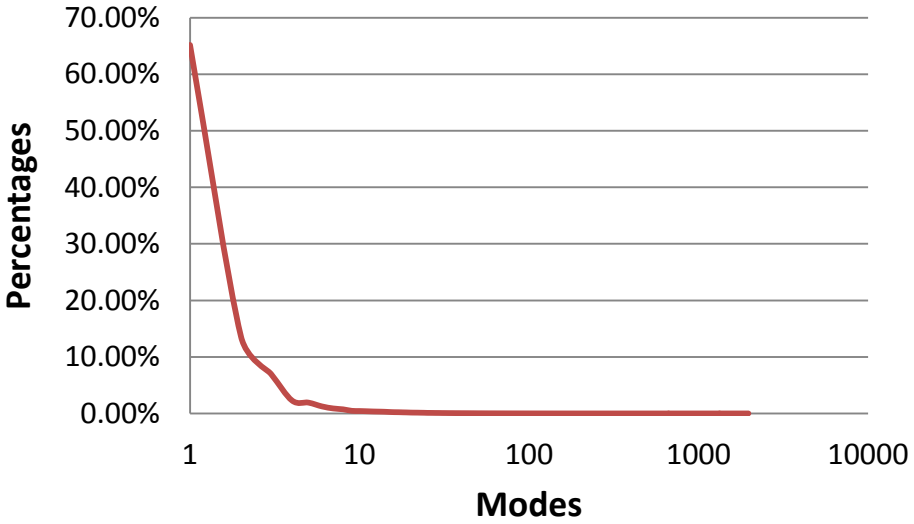

(b)

Figure 37. The percentage of total kinetic energy in each mode. (a) the accumulation percentage for each mode; (b) the percentage for each mode. The first mode contains the 65.2% of the kinetic energy of the flow. The first 80 modes contain 99.1%.

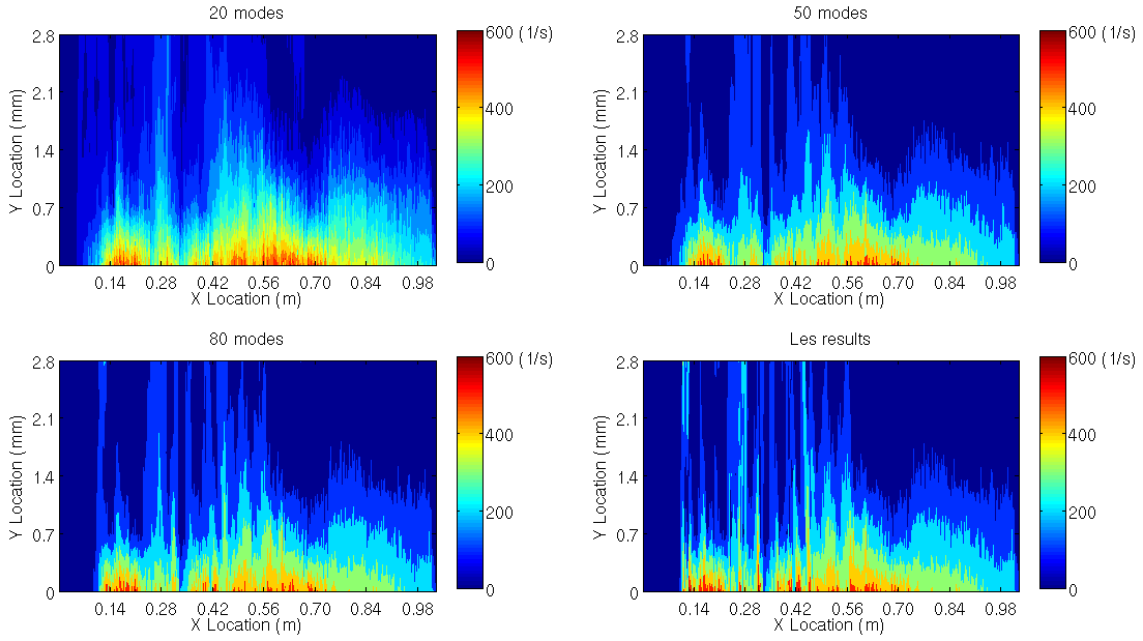

Figure 38. Vorticity magnitude contour of the 1200th snapshot for the LES results and the reconstructions of the wave front head.

Figure 39 shows an example of the reconstruction with 80 modes and the original LES results. The 80 modes were selected because of 99.1% of the original signal. Only a slightly improvement was offered in the reconstruction with 80 modes that showed minor differences compared to the LES results. POD had a slightly better effort in the study of the fluid interface than in that of the wave front head.

6.2 Section 2 – OECD Bundle Benchmark Problem

OECD bundle problem contained two types of the spacers (split and swirl). The effects of using different spacers focused on the hydraulic tests of velocity profiles and flow behaviors. The CFD simulations were validated with the experimental data that were measured for a plenty times and were ensemble averaged from the total dataset. In

order to compare with the experimental data, the averaging results of simulations were calculated from two methods: directly using the RANS models or the time-averaged LES calculations.

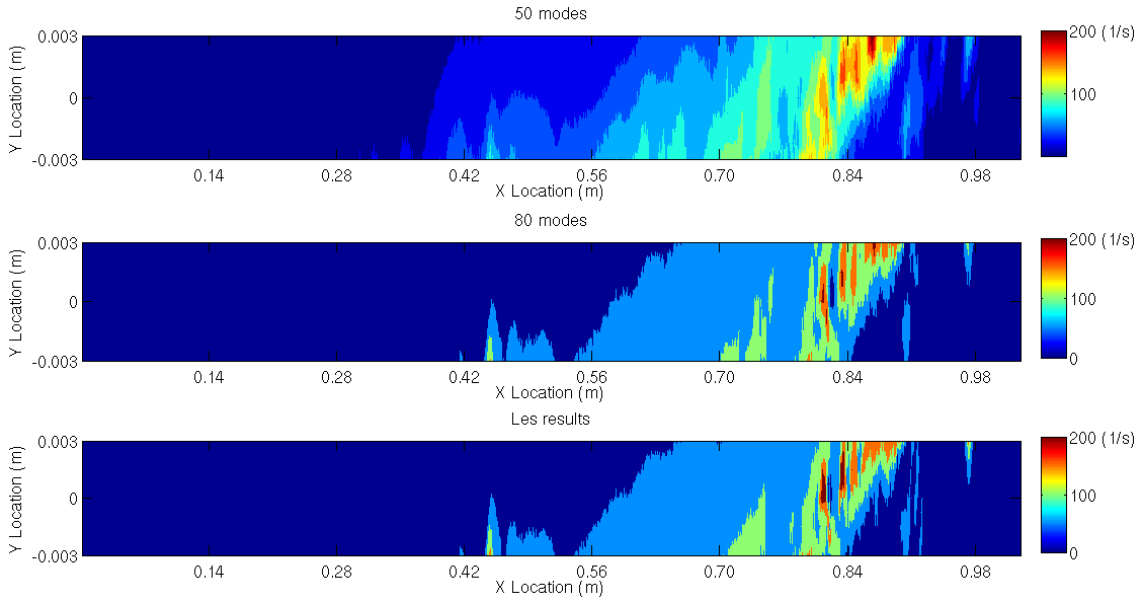

Figure 39. Vorticity magnitude contour of the 600th snapshot for the reconstruction with 80 modes and the original LES results for the interface.

The shear stress transport k-ω model was used for CFX and FLUENT as well as STAR-CCM+. The LES turbulent model was used for STAR-CCM+ because of convenience of extracting results. The Richardson extrapolation was implemented for the grid independent study to obtain higher fidelity results. The hydraulic diameter (D_h) is 24.27 mm. The analyses were performed in four different downstream.

6.2.1 Split type spacer

The comparisons between the simulation results of three computer codes and the experimental data that were provided from the OECD/NEA organization were shown from Figure 40 to Figure 51 where each figure presented the velocity profiles along with x-axis in three different Y and four different downstream planes. The 1.5 mm mesh size was implemented to three codes, and the finest mesh size of 0.5 mm was used for the unsteady RANS and the LES models in STAR-CCM+. The same mesh size in three different codes showed similar velocity profiles, but the different mesh size that was used in the same code predicted significant discrepancies as the expectations. It was obvious that the velocity profiles showed highly accordance with the experimental data at the downstream where the locations were just after ($0.5D_h$) and far away ($10D_h$) from the spacer. In Figure 40, the LES model under predicted flow velocity at approximately 20 mm where the RANS model performed very good agreement with the experimental data. Similarly, the RANS model under predicted velocity at approximately 75 mm where the LES model calculated good agreements with the experiment in Figure 40. The 1.5 mm mesh size showed the trend of the velocity profile of the experiment, but the velocity magnitudes did not match with the experimental data. At the $1.0D_h$ downstream, the simulations with the finest mesh size predicted slightly better results than the 1.5 mm mesh size which showed enormous discrepancies. The 1.5 mm mesh size over predicted velocities in Figure 43 and Figure 44 and under predicted at some points in Figure 45.

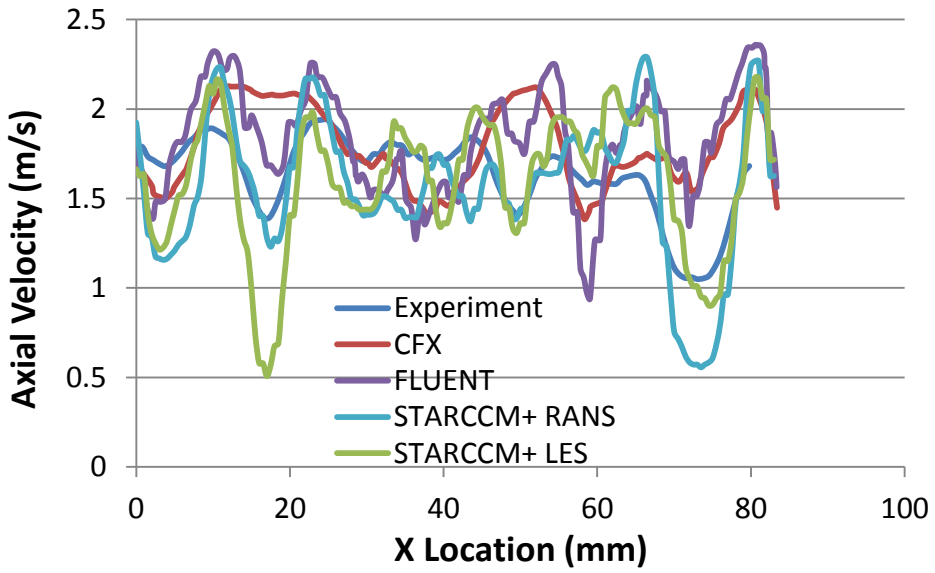

Figure 40. Line probe at the plane of 0.5 D_h downstream, Y=16.6mm, X=0 to 85mm.

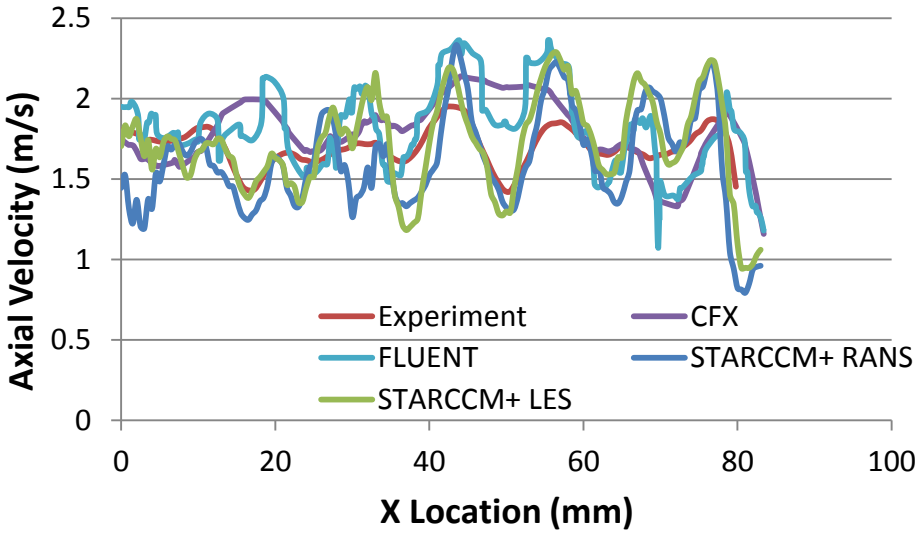

Figure 41. Line probe at the plane of 0.5 D_h downstream, Y=49.7mm, X=0 to 85mm.

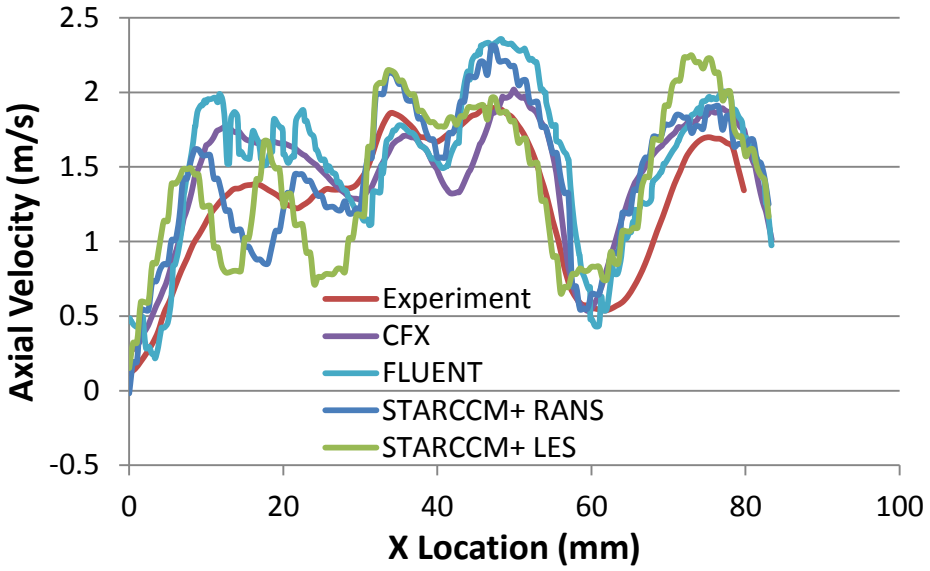

Figure 42. Line probe at the plane of 0.5 D_h downstream, Y=81.3mm, X=0 to 85mm.

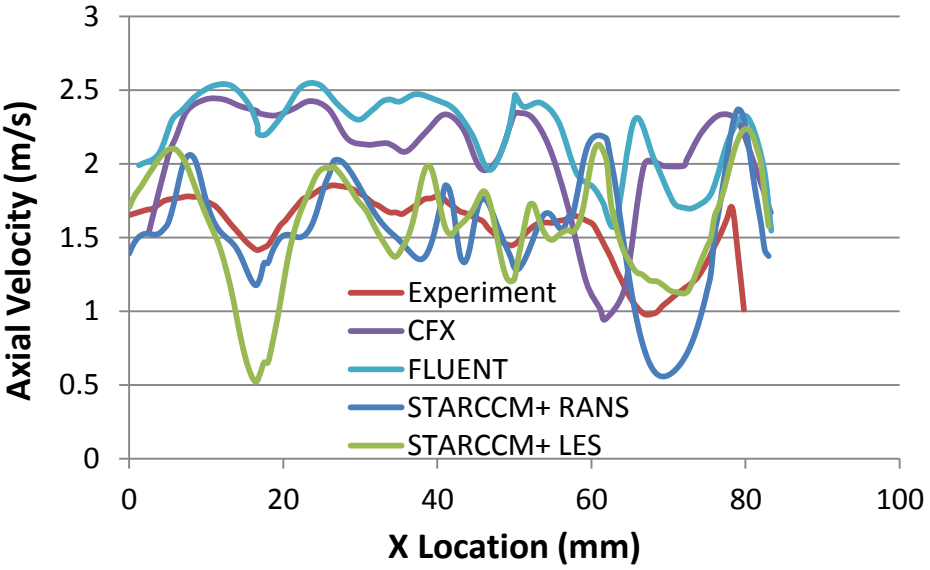

Figure 43. Line probe at the plane of 1.0 D_h downstream, Y=16.6mm, X=0 to 85mm.

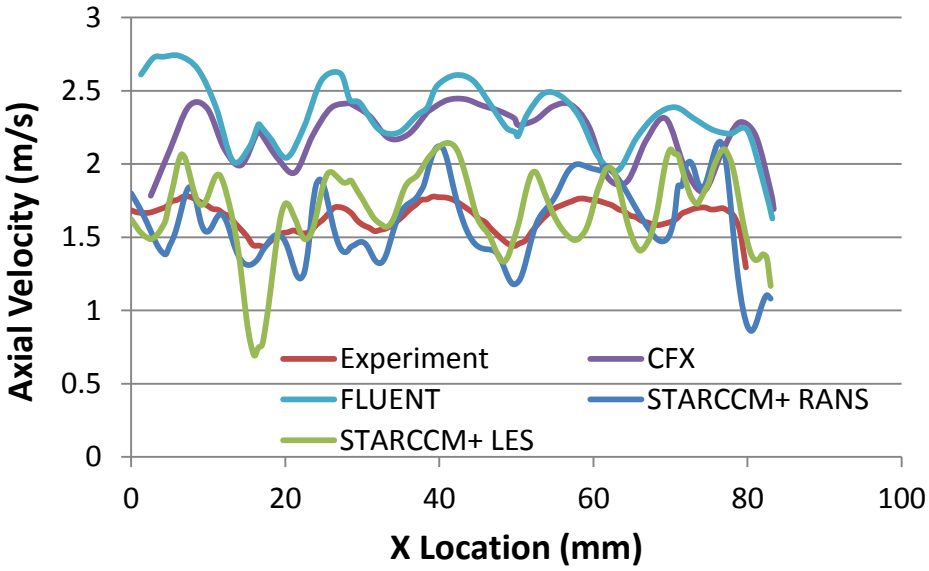

Figure 44. Line probe at the plane of 1.0 D_h downstream, Y=49.7mm, X=0 to 85mm.

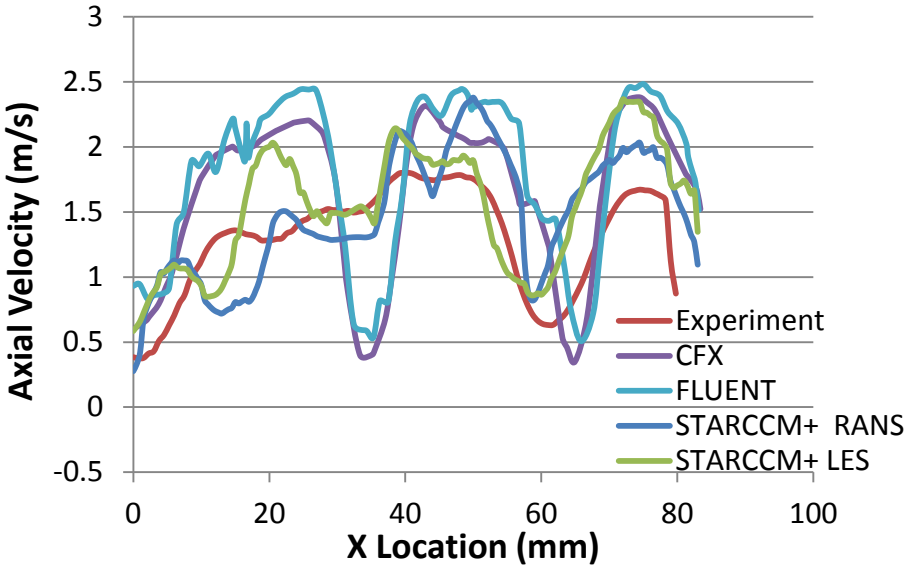

Figure 45. Line probe at the plane of 1.0 D_h downstream, Y=81.3mm, X=0 to 85mm.

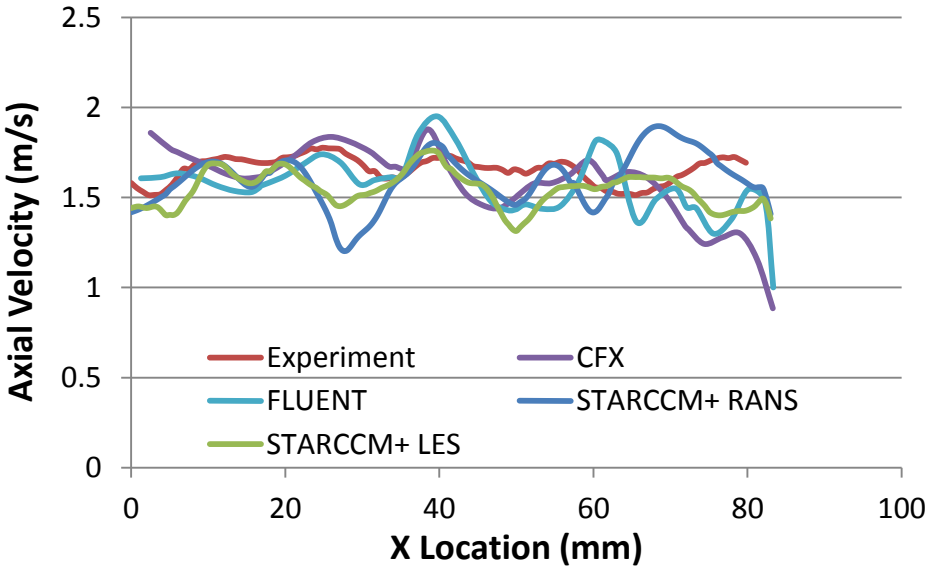

Figure 46. Line probe at the plane of 4.0 D_h downstream, Y=16.6mm, X=0 to 85mm.

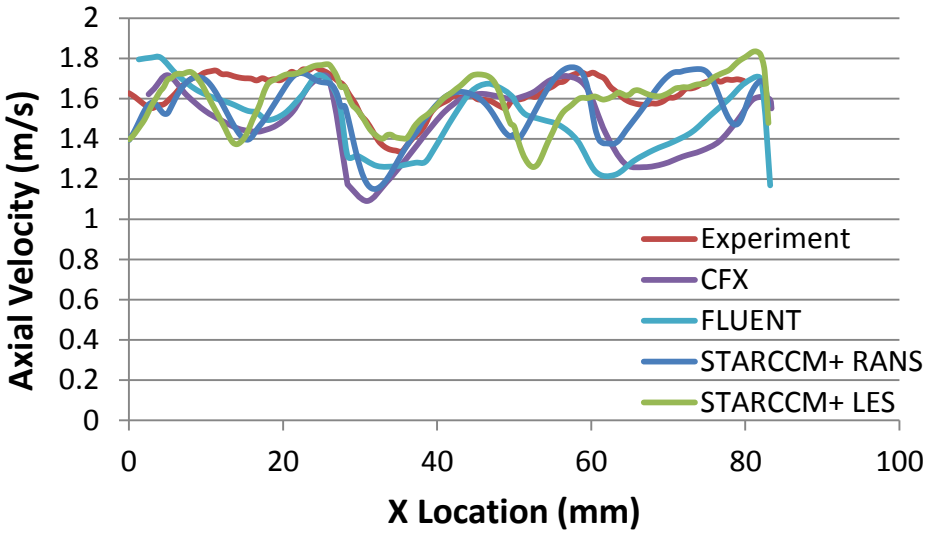

Figure 47. Line probe at the plane of 4.0 D_h downstream, Y=49.7mm, X=0 to 85mm.

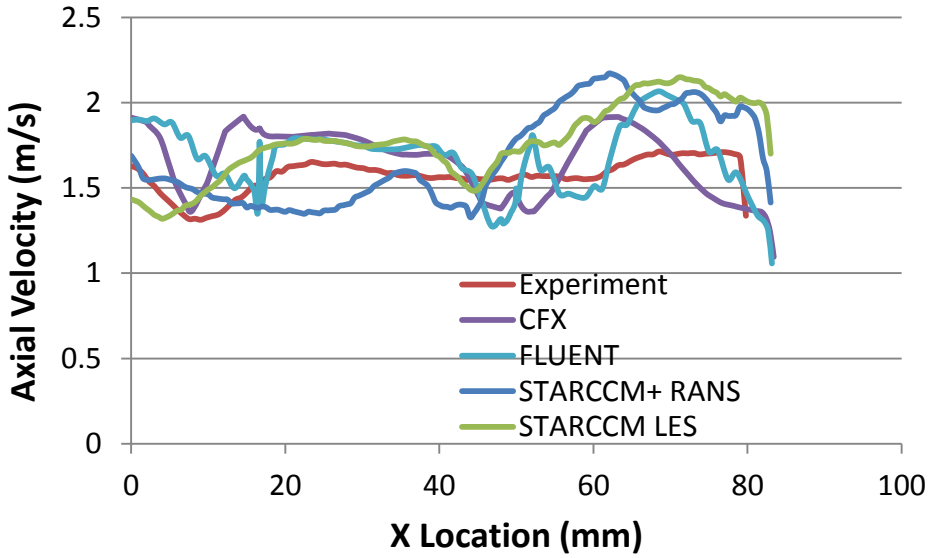

Figure 48. Line probe at the plane of 4.0 D_h downstream, Y=81.3mm, X=0 to 85mm.

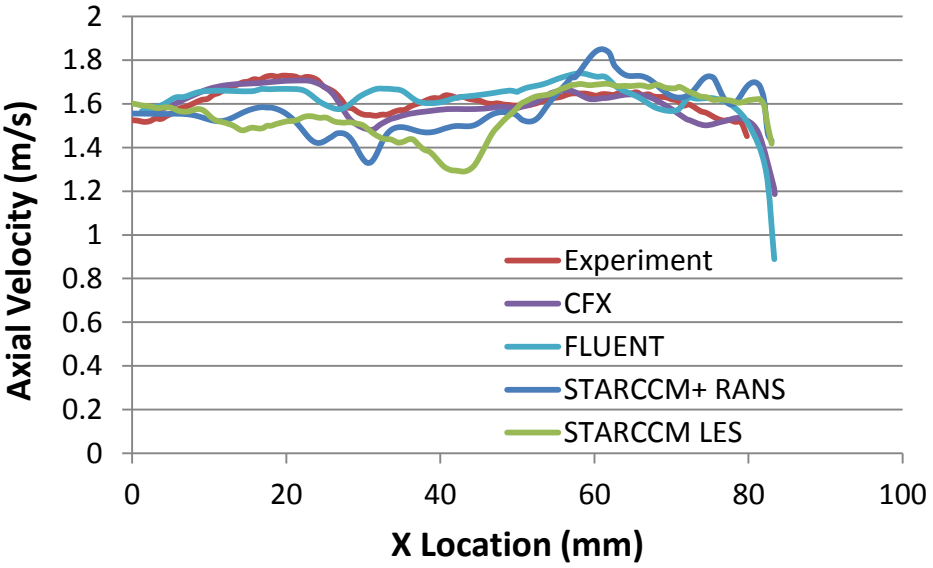

Figure 49. Line probe at the plane of 10.0 D_h downstream, Y=16.6mm, X=0 to 85mm.

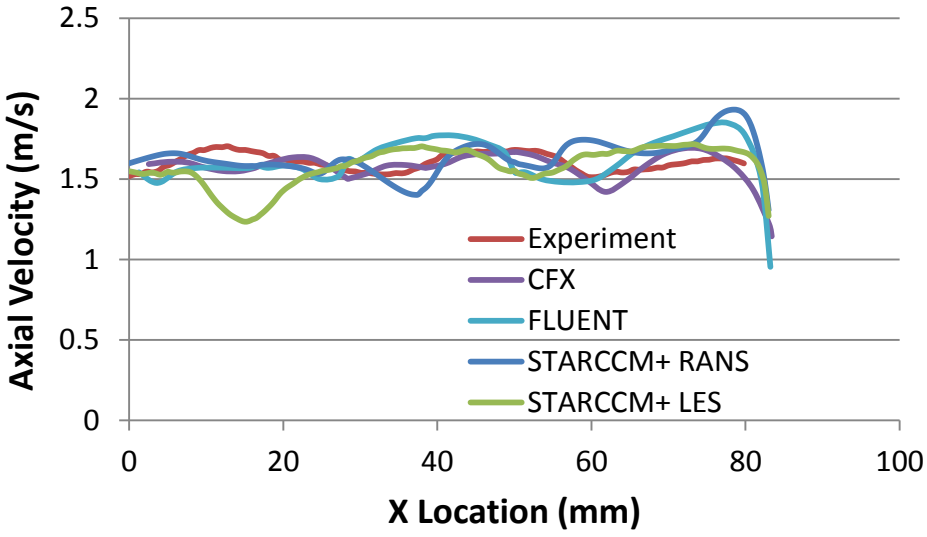

Figure 50. Line probe at the plane of 10.0 D_h downstream, Y=49.7mm, X=0 to 85mm.

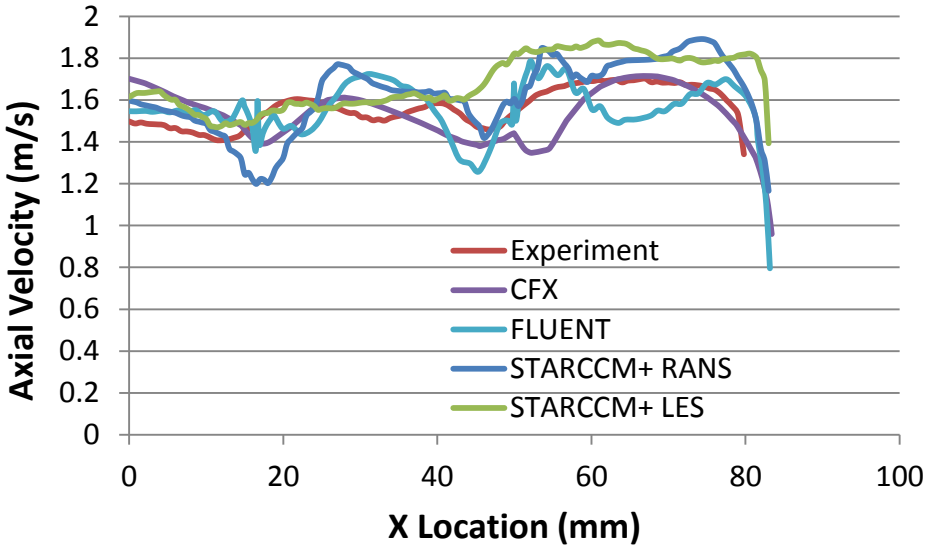

Figure 51. Line probe at the plane of 10.0 D_h downstream, Y=81.3mm, X=0 to 85mm.

However, not only RANS but also LES models did not provide good results with the finest mesh size in Figure 45. Approximately, the finest mesh size calculated better performance of velocity profiles than the 1.5 mm mesh size at the $1.0D_h$ downstream. At $4.0D_h$ downstream, the RANS and LES simulations predicted some discrepancies in Figure 46; for example, the position of X = 27 mm. The simulation results showed good agreements with the experimental data Figure 47, but none of the simulations caught the velocity profile as the experimental data in Figure 48. Generally, all simulations predicted better agreements at the far downstream ($10.0D_h$) than other downstream locations because of no the intense flow patterns with large vortices at very far downstream. Especially, significant disagreements were given at the $1.0D_h$ downstream where the highly turbulence was introduced by the vane of the split-type spacer. The massive discrepancies were showed in the line probes at Y=81.3 mm for the fours downstream. At some locations, the RANS model showed better results than the LES approaches, and *vice versa*. Similar results were performed in three codes; the mesh size gave significant differences. It was difficult to declare which code or turbulent model was the most appropriate to predict flow behaviors for the split-type spacer.

Since much information is obtained from the simulations and the results of the cases with coarse mesh have massive discrepancies, the selected comparisons between the experimental data and the simulations are shown in Figure 52. The selected locations were X from 0 to 85 mm at Y=16.6 mm at $0.5D_h$ downstream. In Figure 52, it is obvious that the low axial velocities are shown at the center of the subchannel. Because the flow was guided by the vanes in the certain directions through the spacer, the flow is

separated at the subchannels and forms large vortices. These large vortices showed strongly lateral velocities and decreased axial velocities. In the center of the gap that is defined as the location between the rods, the flow slightly increases. This is because the opposite vortices appear surrounding the center of gap at which the flows merge. The highly vortices are observed in the subchannels due to the vane effects shown in Figure 53 and Figure 54. The flow patterns at the downstream right after the spacer are strongly influenced by the vanes. Figure 53 and Figure 54 show the Z-vorticity contours at $0.5D_h$ downstream.

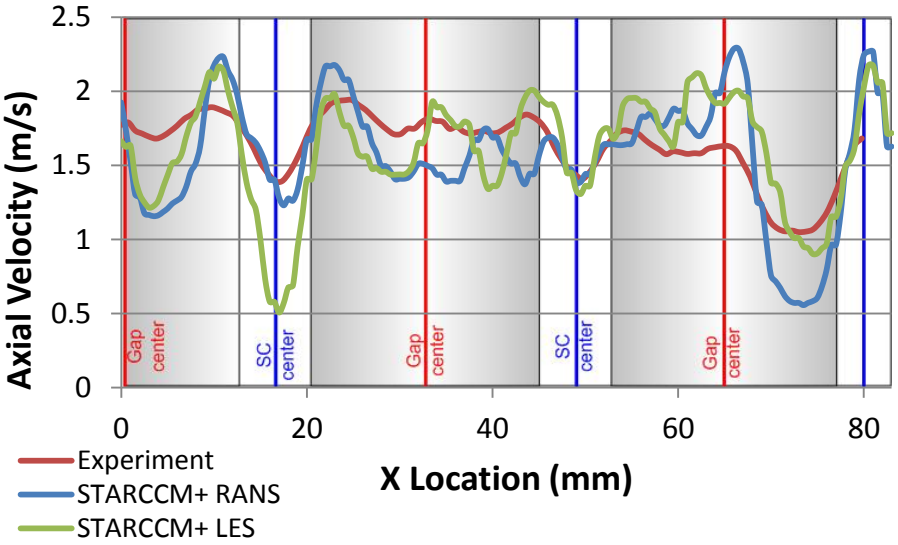

Figure 52. Selected velocity profile at Y=16.6mm and $0.5D_h$ downstream.

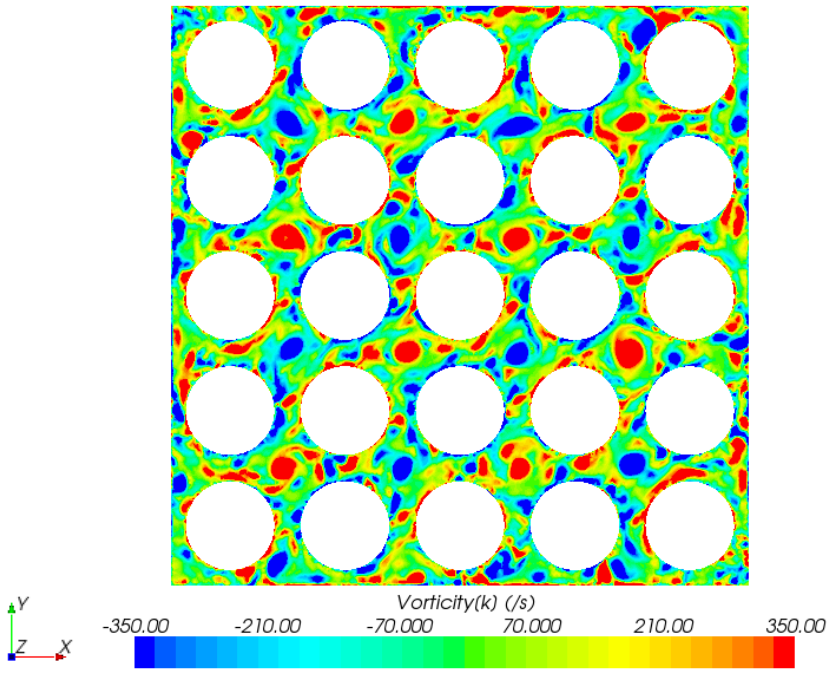

Figure 53. LES instantaneous Z-vorticity contour at $0.5D_h$ downstream.

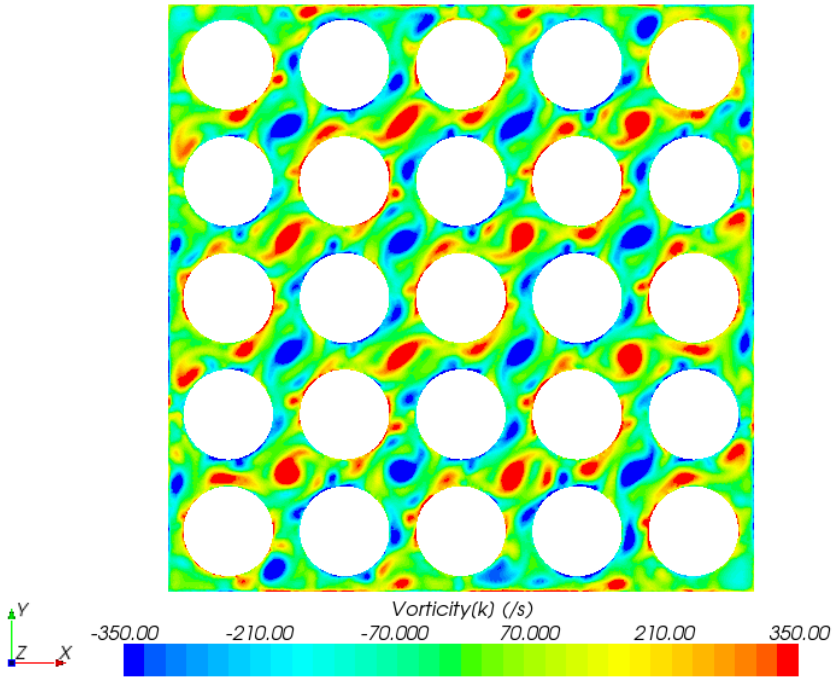

Figure 54. RANS time-average Z-vorticity contour at $0.5D_h$ downstream.

The instantaneous LES results gave the whole view which showed the flow patterns changed massively. The LES results showed small shapes of the vortex and steep velocity gradients in the subchannels. The significantly steep gradients that were observed in Figure 53 attenuated the velocity magnitude dramatically shown in Figure 55 and Figure 56. The velocities were much lower for the LES simulation than the RANS case at the center of the subchannel because of steep velocity gradients. Generally, the simulation results from either RANS or LES approaches captured flow behaviors and patterns. The trends of the velocity profile were predicted well in the simulation with LES approaches.

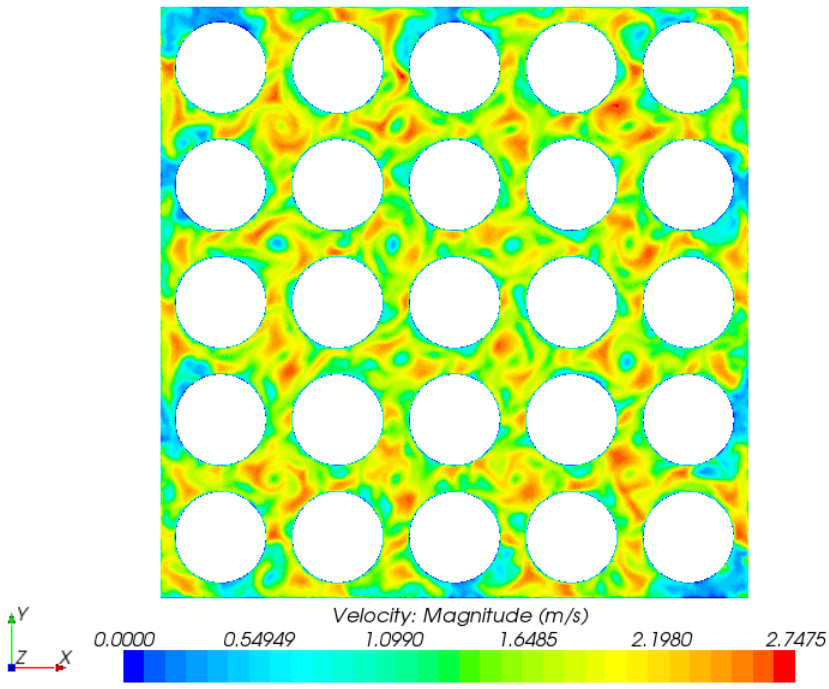

Figure 55. LES instantaneous velocity magnitude contour at $0.5D_h$ downstream.

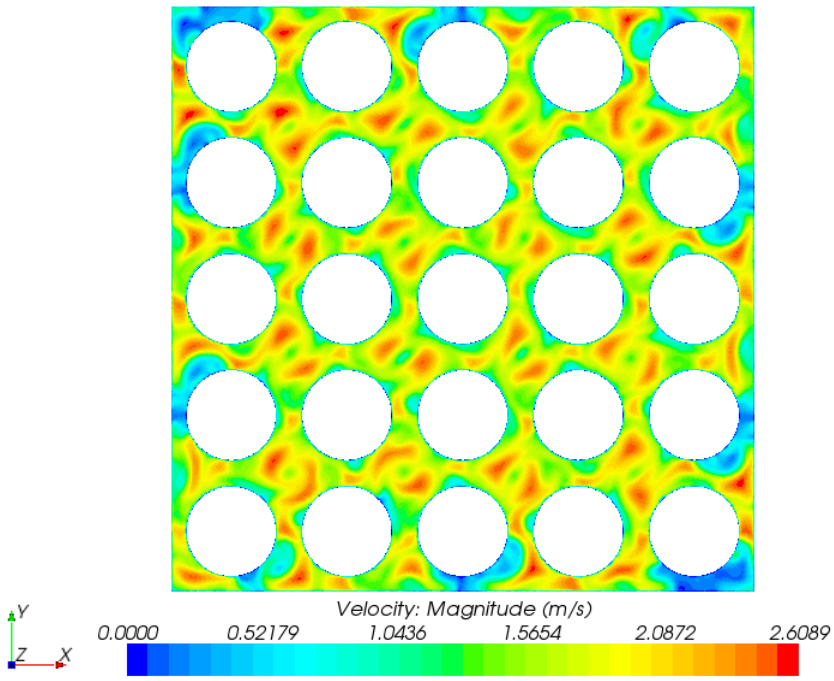

Figure 56. RANS time-average velocity magnitude contour at 0.5D_h downstream.

6.2.2 Swirl type spacer

In this section, the swirl-type spacer was studied. The comparisons between the simulation results and the experimental data were shown from Figure 57 to Figure 68. Similarly, the velocity profiles along with X-axis in three different Y and four different downstream planes were illustrated. From Figure 57 to Figure 68, the simulation results of using the 0.5 mm mesh size were different with those of using the 1.5 mm mesh size. The simulations with 1.5 mm mesh size over predicted the flow velocities in most of the locations. Especially, FLUENT predicted larger discrepancies than the other commercial codes. Even when the finest mesh size of 0.5 mm was implemented for the simulations, STAR-CCM+ was unable to predicted good agreements with the experimental data in

every planes. Especially, STAR-CCM+ showed massive differences at Y=81.3mm (Figure 59) but predicted approximately good agreements (Figure 57 and Figure 58) with the experimental data at the $0.5D_h$ downstream. It was similar to the comparisons of the split-type spacer; the simulations with the 1.5 mm mesh size over predicted flow velocities in three Y locations at the $1.0D_h$ downstream (Figure 60 to Figure 62). However, the cases with the 0.5 mm mesh size showed good predictions than those with larger mesh size. The velocity profiles were hardly captured by three codes, although the finest mesh size (0.5 mm) was used for the simulations at the $4.0D_h$ downstream (Figure 63 to Figure 65). Significant discrepancies were shown in Figure 63 to Figure 65. For example, the RANS and the LES models predicted much lower velocities at the X locations approximately as 18 mm and 50 mm in Figure 63 and Figure 64 where the experimental data presented slightly lower values than the neighbors. FLUENT completely missed the velocity profiles at the $4.0D_h$ downstream (Figure 63 to Figure 65); even the finest mesh size rarely predicted the profiles. At the far downstream ($10.0D_h$), the simulation with the 0.5 mm mesh size (both RANS and LES models) predicted good agreements with the experimental data because of less turbulence caused by the vanes of the spacer (Figure 66 to Figure 68).

Differently, the simulations results of three codes with using the swirl-type spacer predicted better agreements than those with using the split-type spacer for four downstream. Especially, the simulations results of swirl-type spacer showed highly accordance at the $0.5D_h$ downstream than the split-type spacer (Figure 40 to Figure 42 and Figure 57 to Figure 59). The plane location at the $0.5D_h$ downstream was right after

the vanes of the spacer where the flow was redirected. Again, it was difficult to describe which turbulent model was the best or the most appropriate to predict the flow velocities, but generally the 0.5 mm mesh size with RANS or LES models was more appropriate to obtain flow behaviors. Generally, three commercial codes with the coarse mesh size as1.5 mm did not capture the effects caused by the swirl-type vanes. The comparisons between the steady and unsteady simulations were close to each other for most of the predictions and several features were confirmed against experimental work. CFD codes with using the finest mesh size (0.5 mm) calculated the results that had the same trend as the velocity profiles of the experimental data in both split- and swirl-type spacers. The flow profiles right after the spacer is still a difficult topic for the rod bundle problems.

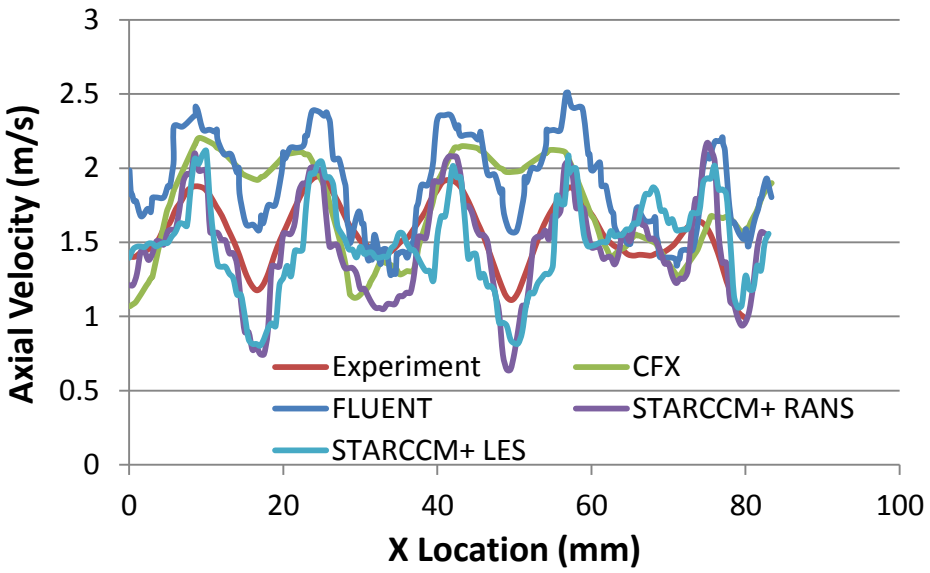

Figure 57. Line probe at the plane of 0.5 D_h downstream, Y=16.6mm, X=0 to 85mm.

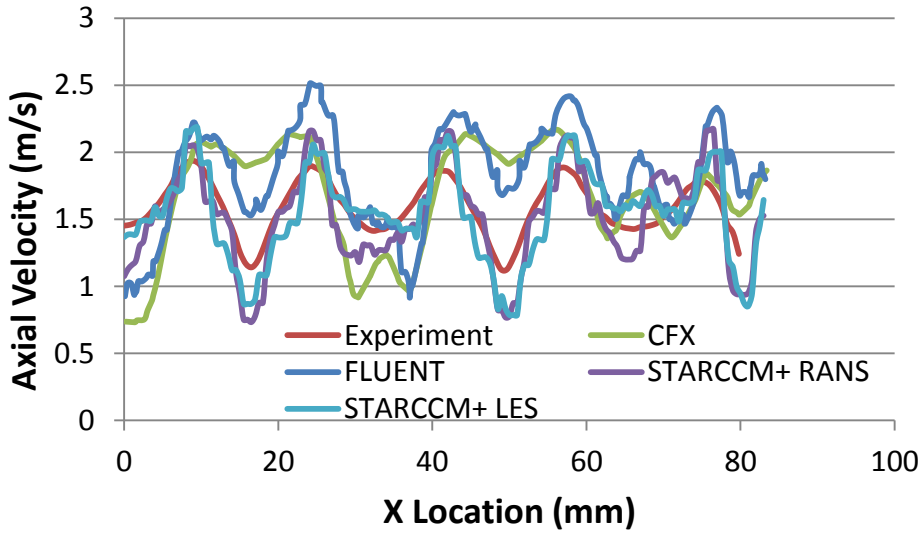

Figure 58. Line probe at the plane of 0.5 D_h downstream, Y=49.7mm, X=0 to 85mm.

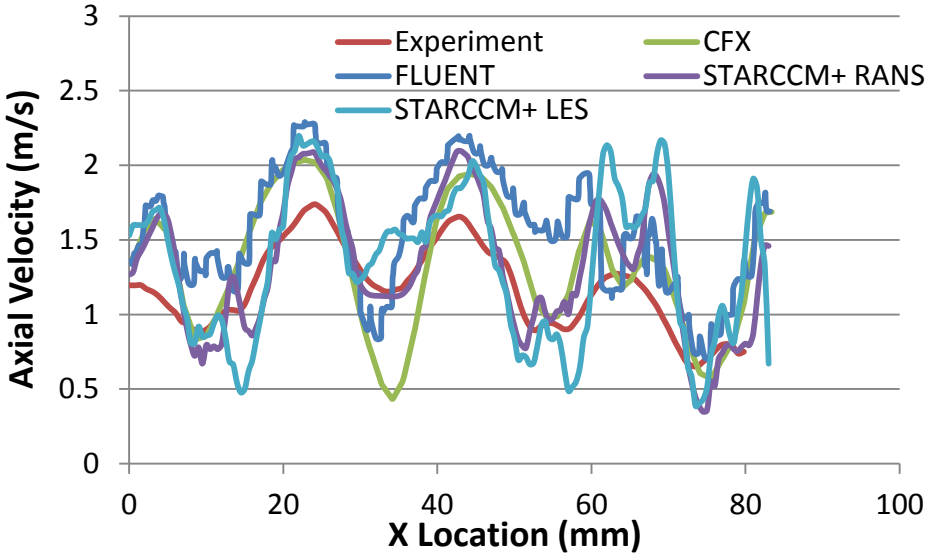

Figure 59. Line probe at the plane of 0.5 D_h downstream, Y=81.3mm, X=0 to 85mm.

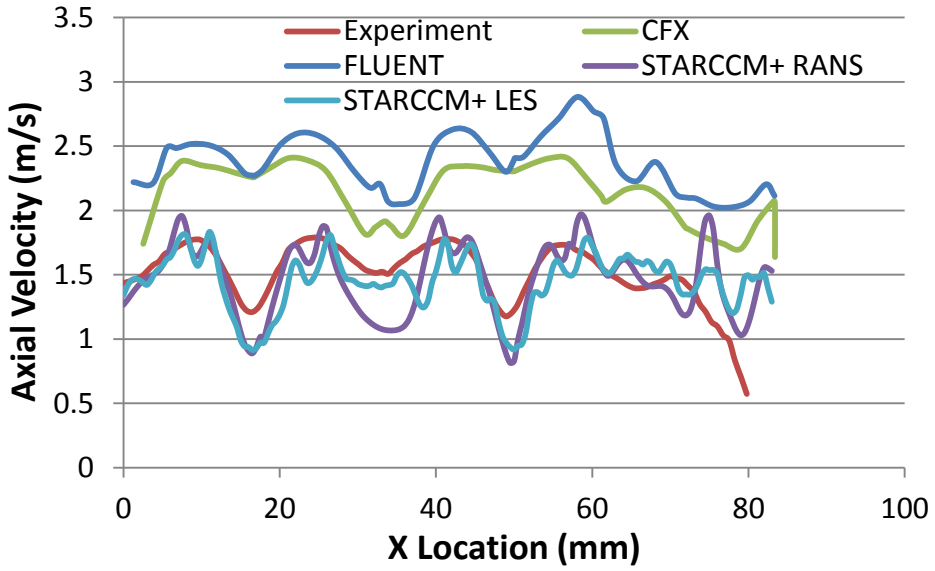

Figure 60. Line probe at the plane of 1.0 D_h downstream, Y=16.6mm, X=0 to 85mm.

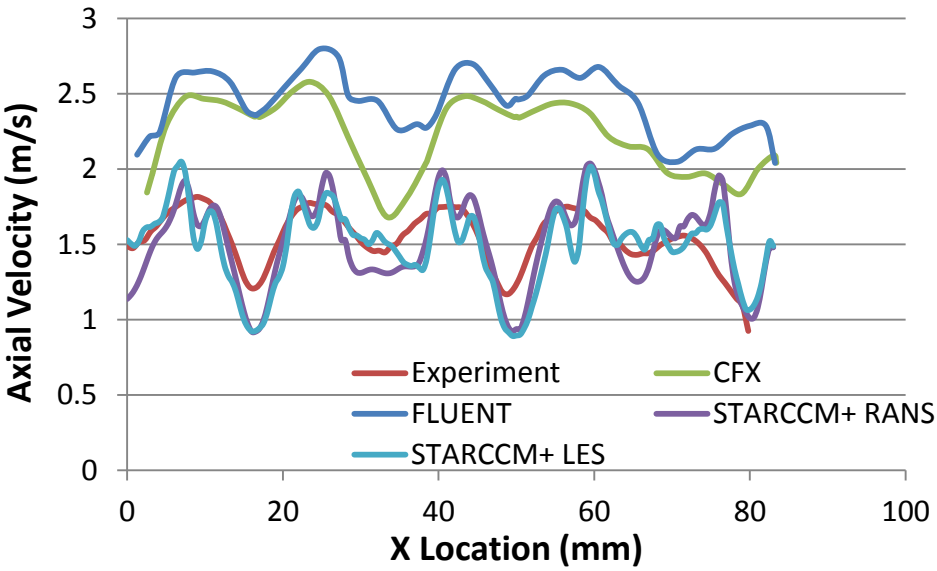

Figure 61. Line probe at the plane of 1.0 D_h downstream, Y=49.7mm, X=0 to 85mm.

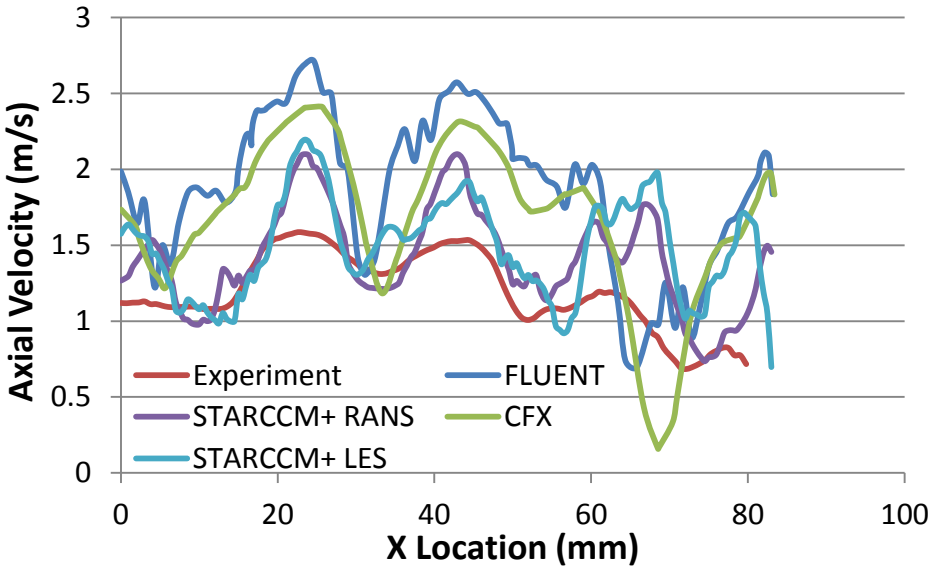

Figure 62. Line probe at the plane of 1.0 D_h downstream, Y=81.3mm, X=0 to 85mm.

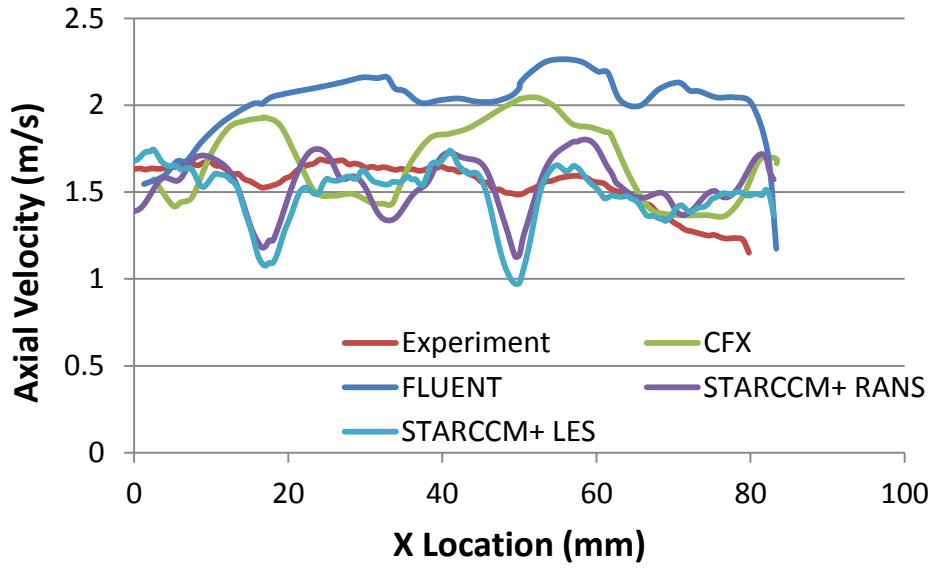

Figure 63. Line probe at the plane of 4.0 D_h downstream, Y=16.6mm, X=0 to 85mm.

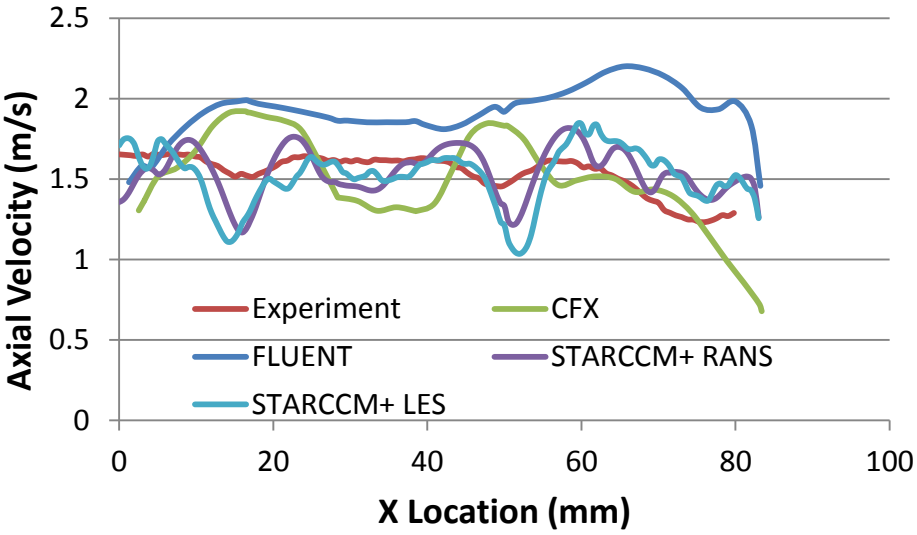

Figure 64. Line probe at the plane of 4.0 D_h downstream, Y=49.7mm, X=0 to 85mm.

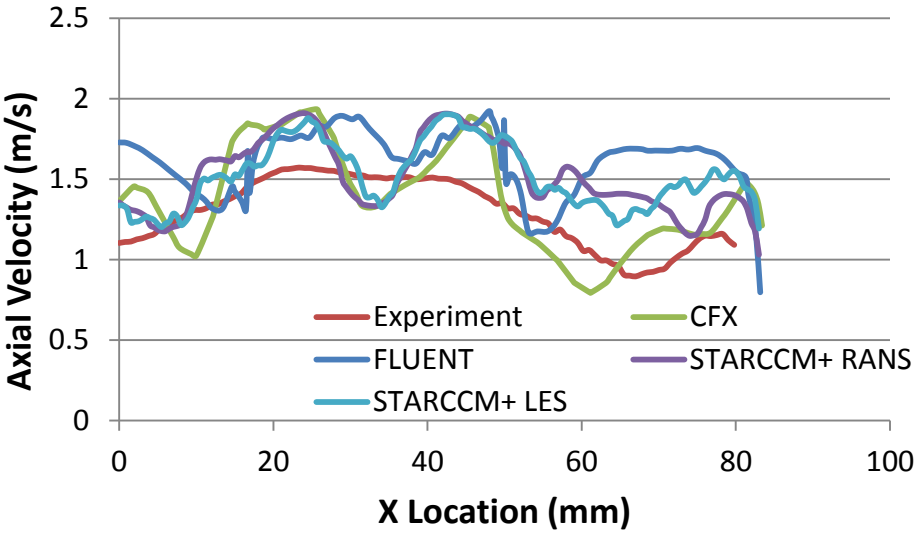

Figure 65. Line probe at the plane of 4.0 D_h downstream, Y=81.3mm, X=0 to 85mm.

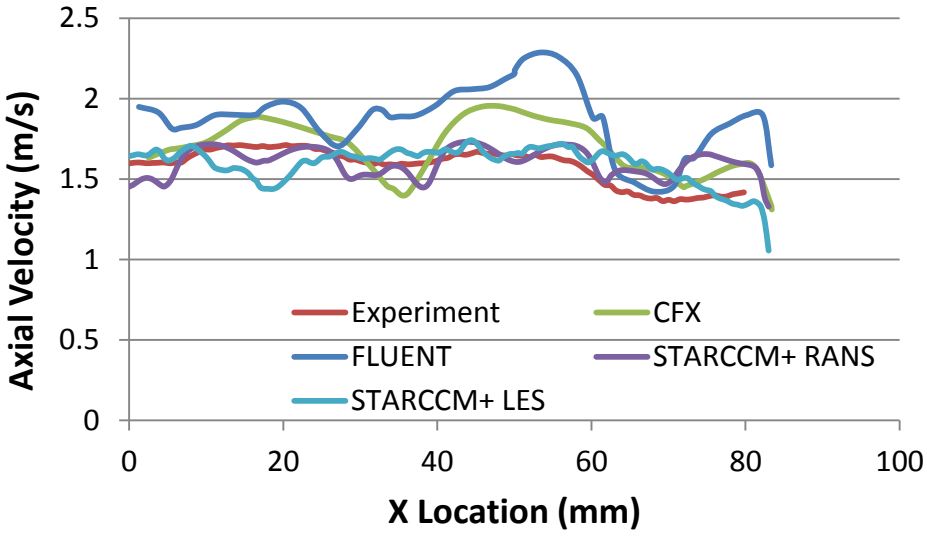

Figure 66. Line probe at the plane of 10.0 D_h downstream, Y=16.6mm, X=0 to 85mm.

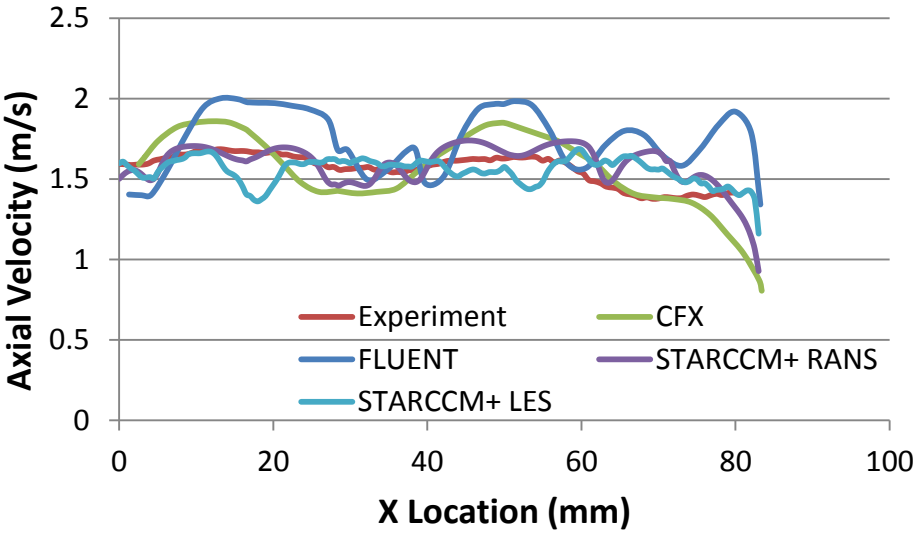

Figure 67. Line probe at the plane of 10.0 D_h downstream, Y=49.7mm, X=0 to 85mm.

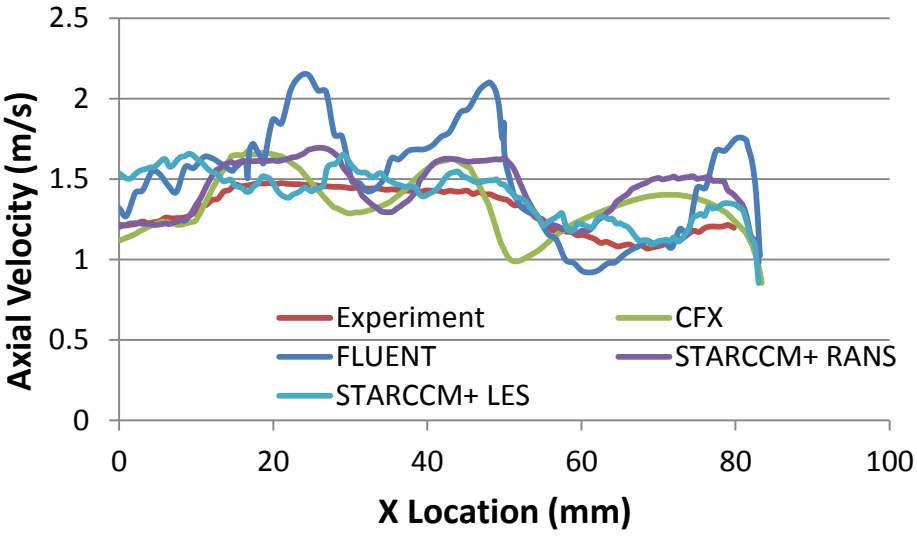

Figure 68. Line probe at the plane of 10.0 D_h downstream, Y=81.3mm, X=0 to 85mm.

6.2.3 POD method analysis

The velocity profiles of the simulations showed significant discrepancies to the experimental data in both split- and swirl-type spacers. POD method was used to study flow features in order to understand these discrepancies. Highly turbulence at the downstream caused by the vanes was considered as the main reason. As a result, the vorticity magnitude profiles were created to examine whether the flow patterns were disturbed. The percentages of the kinetic energy and enstrophy for each eigenvalue are shown in Figure 69 and Figure 70, respectively. The first mode contained 98.5% of the kinetic energy of the flow; the reconstruction of 20 modes and 50 modes contained approximately 99.1% and 99.5% of the kinetic energy of the flow, respectively.

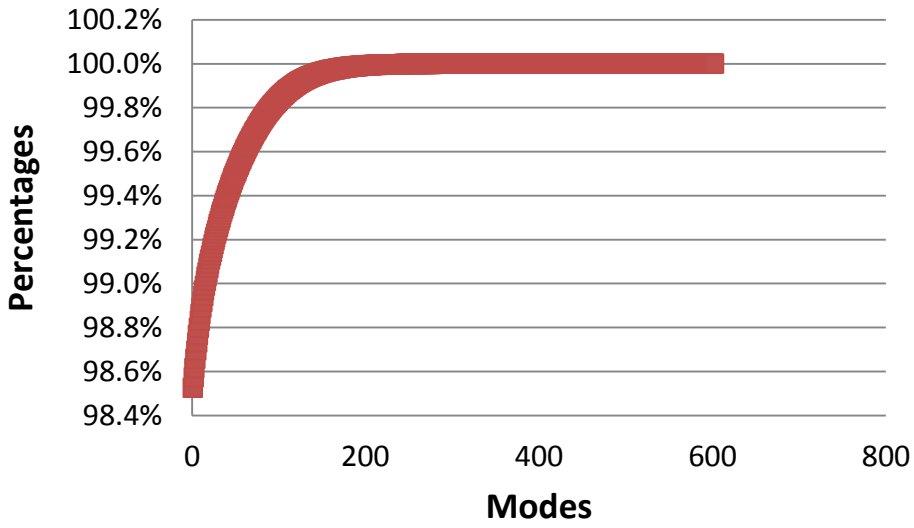

(a)

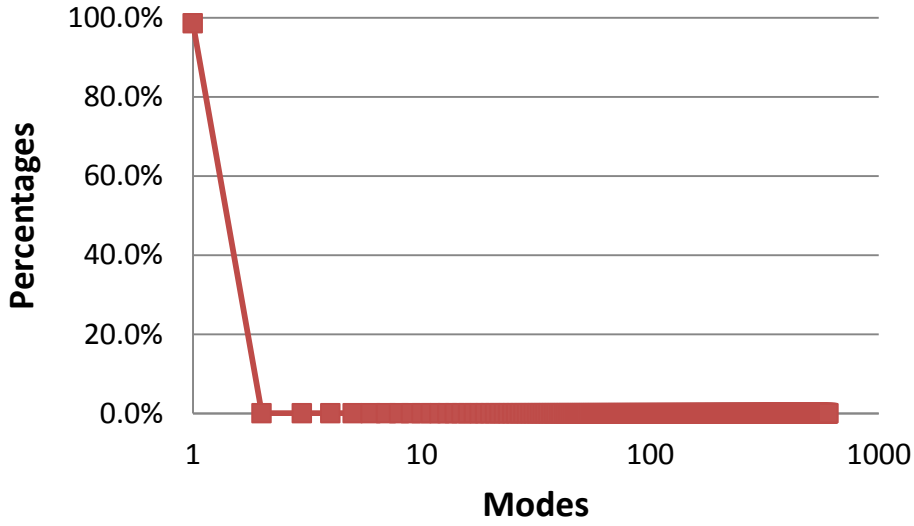

(b)

Figure 69. The percentage of total kinetic energy in each mode: (a) percentage for the accumulation; (b) percentage for each mode. The first mode contained 98.5% of the kinetic energy of the flow. 20 mode contains the 99.1% and 50 modes contain 99.5%.

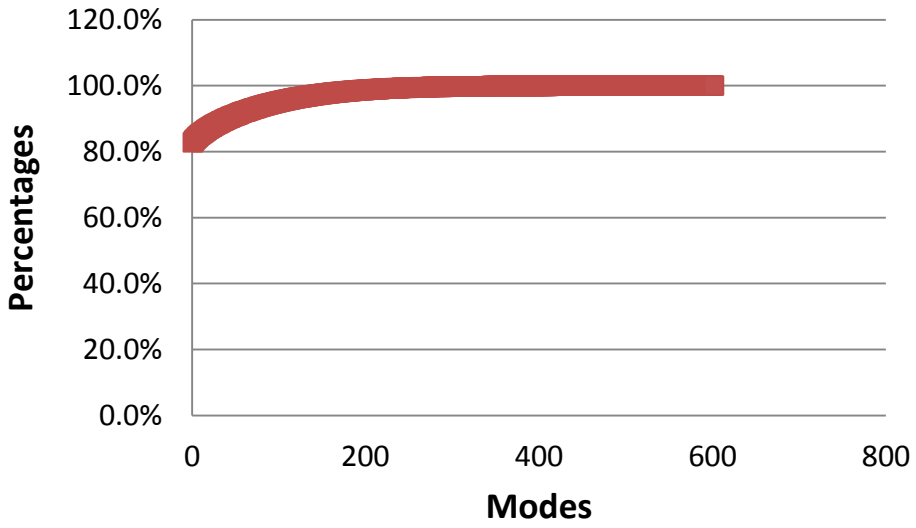

(a)

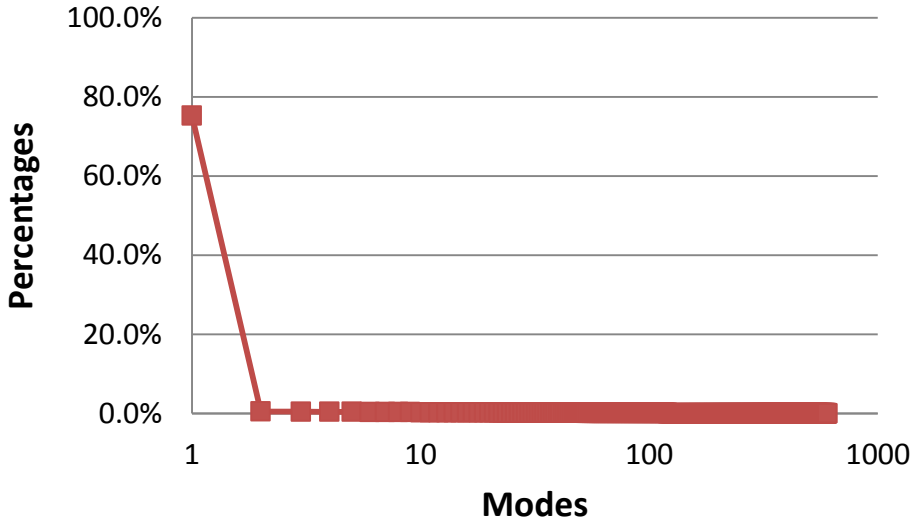

(b)

Figure 70. The percentage of total enstrophy in each mode: (a) percentage for the accumulation; (b) percentage for each mode. The first mode contained 75.2% of the kinetic energy of the flow. 20 mode contains the 81.4% and 50 modes contain 87.1%.

This shows that the first mode as the mean flow contains most of the flow information. The vorticity magnitude contours for the 200^{th} and the 300^{th} snapshots at the first plane (Y = 16.6 mm) are shown in Figure 71 and Figure 72, respectively. The X and the Z locations are along with the lateral and the axial directions, respectively. The X location of 0.049 m is approximately the center of the subchannel in the flow where the X of 0.033 m and 0.065 m are the center of the gaps that were defined as the position between two rods. The original LES results contained all information with large and small scales in the plot. The reconstruction of using 50 modes filtered the small scales information and showed clearly the main vortices. A massive vortex appeared at the center of the subchannel for the length as a minimum of 50 mm.

In the POD snapshot method, the contours changes with different time steps. Figure 71 and Figure 72 show slight difference between two time steps for the POD reconstructions, but the evolution of vortices are not presented in the plots. Only the reconstructions can capture difference of the flow patterns. Moreover, another vortex was obviously observed for the reconstruction with 50 modes at X = 33 mm (the center of the rod) and Z = 50 mm in Figure 71 and Figure 72. The positions as Z = 0.0435 mm and 0.189 mm in Figure 71and Figure 72 were the locations for the $4.0D_h$ and $10.0D_h$ downstream. Using 20 modes filtered more scales of the original signals and gave much more significant flow patterns.

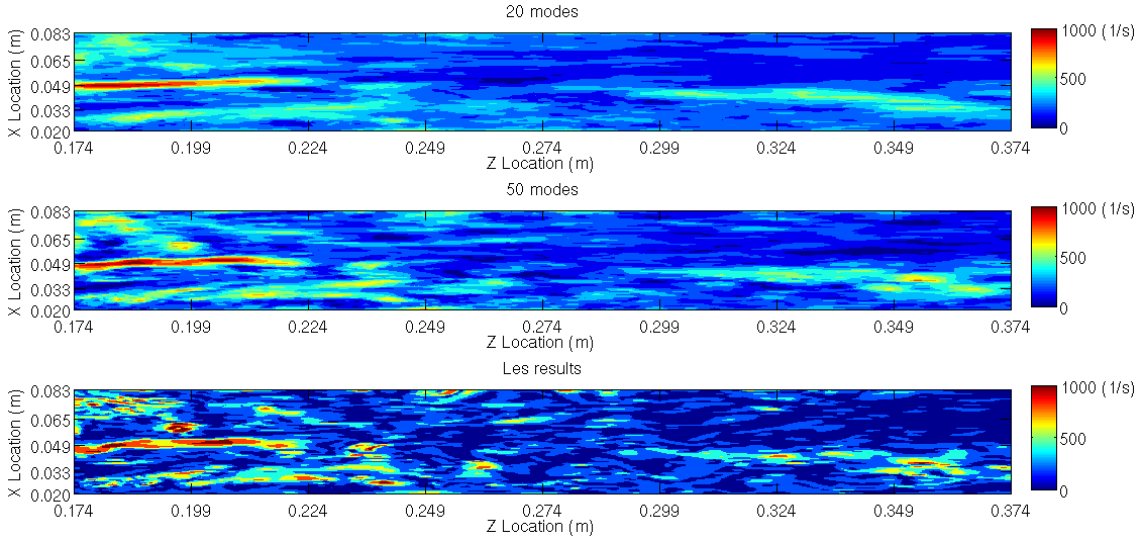

Figure 71. Vorticity magnitude contour of the 200th snapshot at the plane as Y=16.6mm, X=20mm to 83mm, and Z=174mm to 374mm downstream: (up) 20 modes reconstruction; (center) 50 modes reconstruction; (down) original LES results.

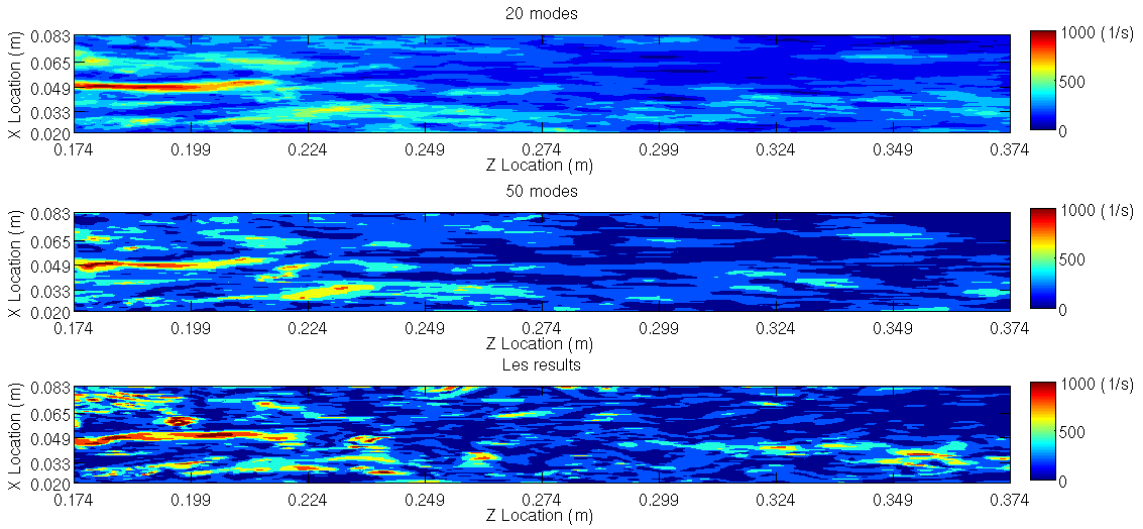

Figure 72. Vorticity magnitude contour of the 300th snapshot at the plane as Y=16.6mm, X=20mm to 83mm, and Z=174mm to 374mm downstream: (up) 20 modes reconstruction; (center) 50 modes reconstruction; (down) original LES results.

For the reconstruction with 20 modes, the highly turbulence was seen at the center of the subchannel. Minor vortices compared to the main vortex were observed at the center of the rods (X = 33 mm and 65 mm). These large vortices were regarded as coming from the effects of the vanes of the spacers and affecting the velocity profiles. The minor vortices appeared at the $4.0D_h$ downstream directly influenced the velocity distribution as shown in Figure 46. The RANS and LES simulations predicted smaller velocities at the positions as X = 27 mm and 67 mm. The velocity profiles of RANS and LES results in Figure 49 showed significant discrepancies at the X positions between approximately 20 mm to 50 mm where the intermediate vortices are located in Figure 71.

Similarly, Figure 73 can be used to compare with the velocity profiles in Figure 47 and Figure 50. Figure 74 is utilized to compare with Figure 48 and Figure 51. Significant vortices are seen at the center of the subchannel in Figure 73. Figure 74 did not show significant flow features but the different vorticity magnitudes.

6.2.4 Wavelet analysis

The wavelet analysis was implemented to decompose the flow fields obtained from CFD calculations. Similarly, the position at the center of the subchannel was chosen for the wavelet analysis. The Morlet mother function was applied for the 1D continuous transform. The CWT results with the corresponding velocity magnitude profiles are shown in Figure 75. For three different locations, the 1D Morlet CWT showed similar results that the dominant frequency was approximately 2.6 Hz with a secondary dominant frequency as 4 Hz.

Also, the numbers of the modes from 32 to 1024 were implemented for the 1D Morlet CWT shown in Figure 76. Similarly, the more modes were used for the decomposition, the smaller dominant frequency was obtained. Approximately the dominant frequency of 8 Hz was seen in the CWT with 128 modes. The approximately 6 Hz as the dominant frequency became the secondary frequency presented in the results of using 256 modes where the dominant frequency was presented as approximately 4 Hz. Interestingly, when 1024 modes were selected for the 1D continuous transform, the frequency of 2 Hz became the secondary dominant frequency in the result of using 1024 modes where the dominant frequency was approximately 0.8 Hz.

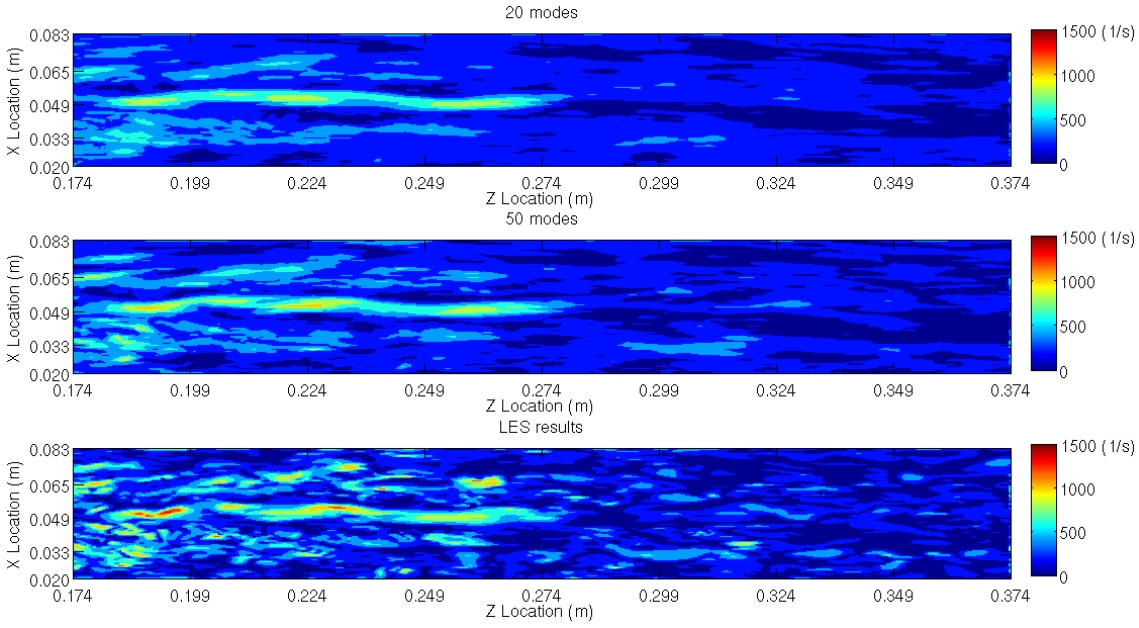

Figure 73. Vorticity magnitude contours at the plane of Y=49.7mm, X=20mm to 83mm, and Z=174mm to 374mm downstream: (up) 20 modes reconstruction; (center) 50 modes reconstruction; (down) original LES results.

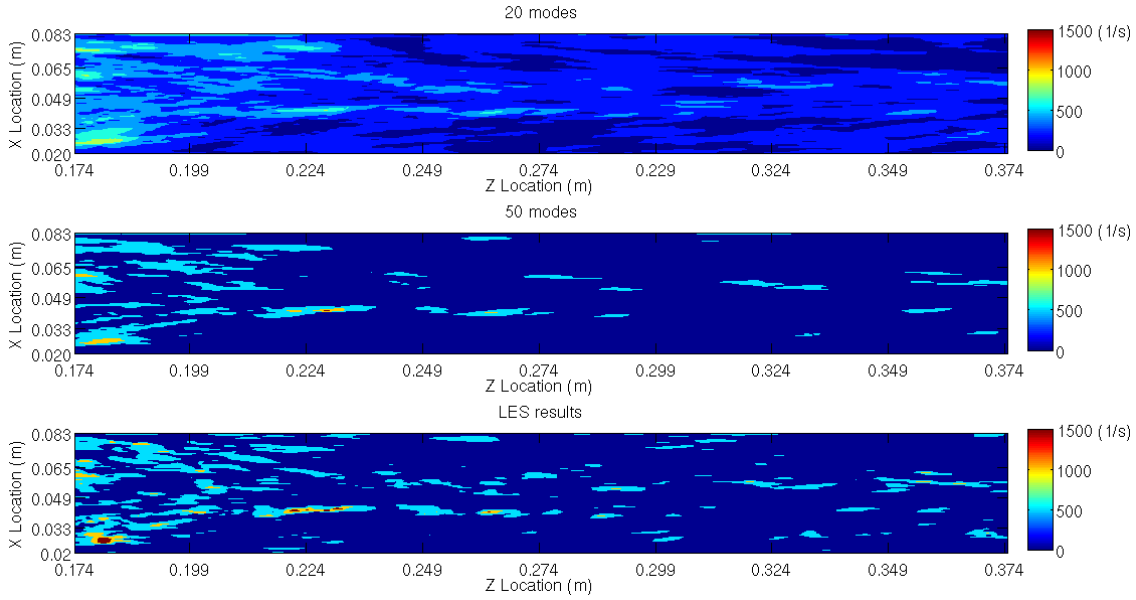

Figure 74. Vorticity magnitude contours at the plane of Y=81.3mm, X=20mm to 83mm, and Z=174mm to 374mm downstream: (up) 20 modes reconstruction; (center) 50 modes reconstruction; (down) original LES results.

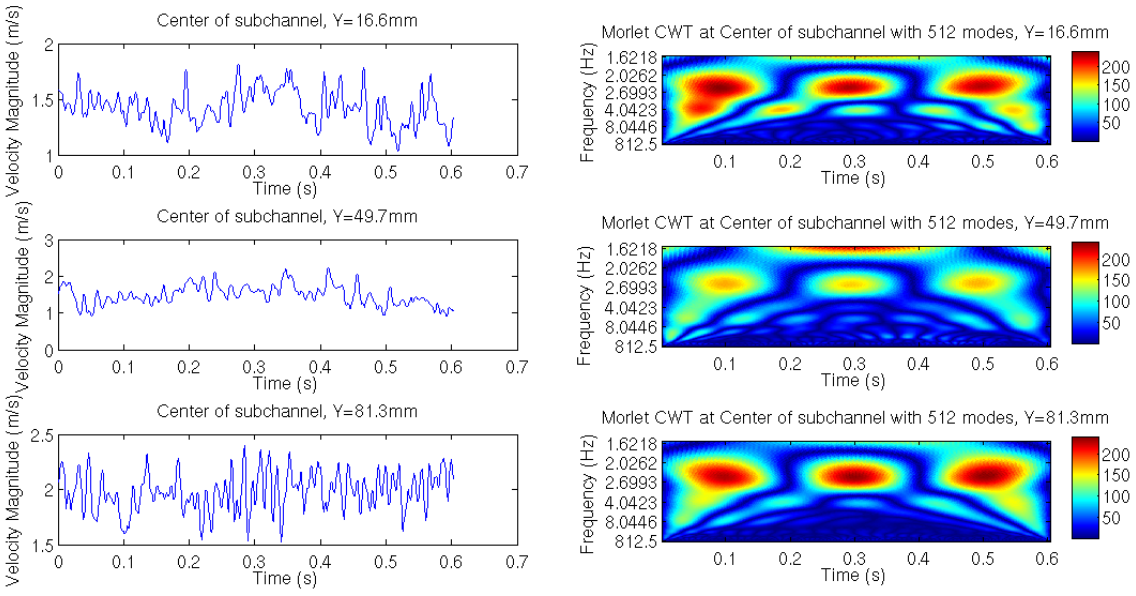

Figure 75. Instantaneous velocity magnitude signals of the positions at the center of the subchannel for three Y location and their 1D continuous transform with using Morlet mother wavelet with 512 modes.

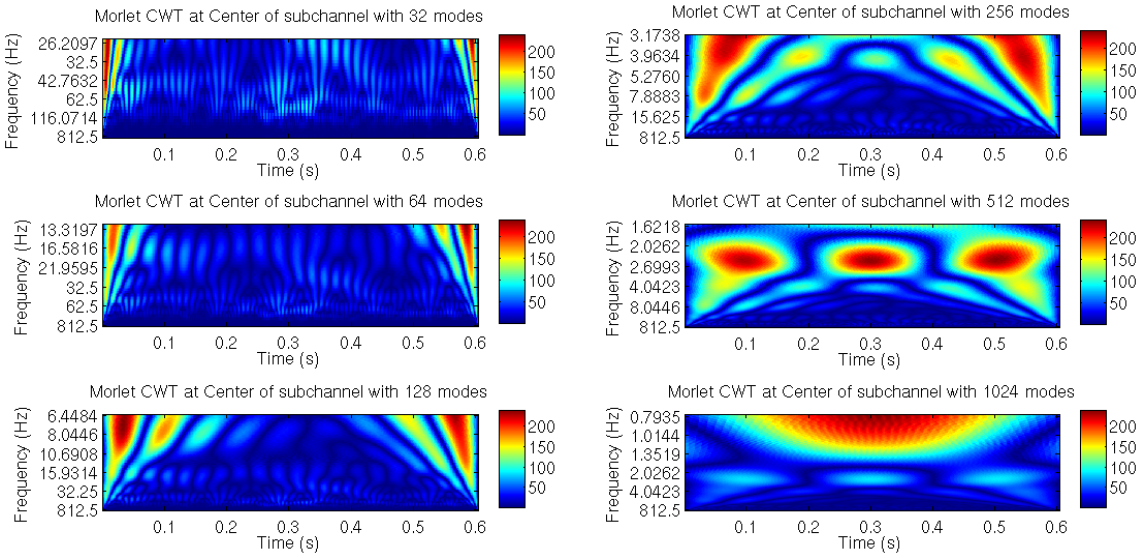

Figure 76. 1D Morlet CWT for the position at the center of the subchannel at Y=81.3mm with different number of modes from 32 to 1024.

CHAPTER VII

CONCLUSION

7.1 Section 1 – Air Ingress Phenomenon

The Richardson extrapolation presented that the 0.7 mm mesh size had the relative errors within 1% for the grid independent study. For the simulations with the 0.7 mm mesh size, the RANS model showed good agreements with the LES approaches. The relative difference between the two turbulent models was approximately 3.32% for the inner pipe and 0.5% for the outer pipe. The moving valve scenarios with a constant speed for total 0.534s decreased the maximum wave front velocities of 24% and 18% for the inner and the outer pipes, respectively. The assumption of the moving valve with a constant speed would be approximately appropriate if the first 0.534s were not highly interesting. The simulation results showed very good agreements with the experimental data, and the relative errors were within 2.4%. The pipe length which was used to mimic the break distance to the reactor enhanced the maximum wave front velocity approximately within 18% for the scenarios between the pipes of 0.38m and 1m.

The POD method can find important components to reconstruct the signal. For the first few modes, it was able to obtain most of the information and the trend of the original signal. Not every mode is required since the last modes are insignificant. Once the modes increase enough, the reconstruction will be similar to the original results. In this study, the first eigenvalue contains the 85.4% of the kinetic energy of the flow. The remaining eigenvalues are regarded as turbulent kinetic energies. 1D Morlet wavelet

analysis gave the dominant frequency as approximately 2.4 Hz. This value was close to the calculation of using the buoyancy frequency which gave the value of approximately 2.34 Hz. The CWT results with 512 modes or 1024 modes confirmed this frequency between times 1.2 s and 1.85 s in Figure 36.

Generally, the wavelet analysis has much better performance than the POD method in the air-ingress phenomenon which is a transient problem. The previous literatures done by the scientists and researchers were studied in the steady stratified flows. The POD method showed less information in a strongly transient problem. Based on this study, when the fluid pair in a real condition is used, the time for the intrusion of heavy fluids is predictable.

7.2 Section 2 – OECD Bundle Benchmark Problem

The highly turbulence occurred by the vanes of the spacers were rarely captured by the CFD codes in this dissertation. As long as the plane was far away downstream from the spacer, CFD codes showed well predictions in both type spacers. From the comparisons with the results of the split-type to the swirl-type spacers, CFD codes showed better predictions for the later type than the former type. It was expected that the simulations with the 0.5 mm mesh size predicted better results than those with the 1.5 mm mesh size. However, the scenarios with 1.5 mm mesh size at some locations showed better calculations than the cases with the finest mesh size. Among the simulations with the finest mesh size, the RANS and the LES models presented similar results. At some locations, the RANS model gave better predictions, and *vice versa*. Three different codes provided similar calculations with the same mesh size for the split-type spacer. CFX and

STAR-CCM+ performed better simulation results than the FLUENT in the swirl-type spacer.

The simulations with using the coarse mesh size of 1.5 mm did not matched with the experimental data. Especially, the trend of the velocity profile was missed. The velocity magnitudes at the center of the subchannels were low in the experiments, and this behavior was captured in the simulations with the finest mesh size (0.5 mm). Even though the calculations showed significant discrepancies with the experimental data, the simulations captured the trend of velocity profiles. The low velocity magnitudes appeared at the positions where the large vortices located, e.g., the center of the subchannels. The highly turbulence was shown in the downstream that was very close to the vanes ($0.5D_h$ and $1.0D_h$). The large vortices influenced the distance in the flow more than 50 mm. For the very far downstream ($10D_h$), the simulation results showed better agreements with the experimental data. The dominant frequency in the flow was regarded as 2.3 Hz with a secondary dominant frequency of 4 Hz and a much minor frequency of 6 Hz in the rod bundle problem.

REFERENCES

1. U.S. DOE Nuclear Energy Research Advisory Committee and the Generation IV International Forum, 2002, "A Technical Roadmap for Generation IV Nuclear Energy Systems," Generation IV International Forum.
2. "Generation IV Nuclear Energy Systems: Ten Year Program Plan", March 2005, Office of Advanced Nuclear Research, DOE Office of Nuclear Energy, Science, and Technology, U.S. DOE (2005).
3. "Next Generation Nuclear Plant Methods Technical Program Plan," INL/EXT-06-11804, January, INL U.S. (2007).
4. N. E. Todreas, M. S. Kazimi, "Nuclear Systems I," Taylor & Francis Group, NY, (1990).
5. T. B. Benjamin, "Gravity currents and related phenomena," *Journal of Fluid Mechanics,* **Vol. 31 part 2**, pp. 209-248, (1968).
6. J. E. Simpson, "Effects of the lower boundary on the head of a gravity current," *Journal of Fluid Mechanics,* **Vol. 61**, pp. 731-751, (1972).
7. R. E. Britter and J. E. Simpson, "Experiments on the dynamics of a gravity current head," *Journal of Fluid Mechanics,* **Vol. 88**, pp. 223-240, (1978).
8. J. E. Simpson and R. E. Britter, "The dynamics of the head of a gravity current advancing over a horizontal surface," *Journal of Fluid Mechanics,* **Vol. 94, part 3**, pp. 477-495, (1979).
9. R. E. Britter and P. F. Linden, "The motion of the front of a gravity current

travelling down an incline," *Journal of Fluid Mechanics*, **Vol. 99, part. 3**, pp. 531-543, (1980).

10. H. E. Huppert and J. E. Simpson, "The slumping of gravity currents," *Journal of Fluid Mechanics,* **Vol. 99**, pp. 785–799, (1980).
11. C. H. Gibson, "Fossil temperature, salinity, and vorticity in the ocean," *Elsevier Oceanography Series*, **Vol. 28**, pp. 221-257, (1980).
12. C. H. Gibson, "Buoyancy effects in turbulent mixing: sampling turbulence in the stratified ocean," *AIAA,* **Vol. 19, No. 11**, pp. 1394-1400, (1981).
13. D. L. Wilkinson, "Motion of air cavities in long horizontal ducts," *Journal of Fluid Mechanics,* **Vol. 118**, pp. 109–122, (1982).
14. G. C. Gardner and I. G. Crow, "The motion of large bubbles in horizontal channels," *Journal of Fluid Mechanics,* **Vol. 43**, pp. 247–255, (1970).
15. J. W. Rottman and J. E. Simpson, "Gravity currents produced by instantaneous releases of a heavy fluid in a rectangular channel," *Journal of Fluid Mechanics,* **Vol. 135**, pp. 95–110, (1983).
16. C. A. G. Webster, "An experimental study of turbulence in a density-stratified shear flow," *Journal of Fluid Mechanics,* **Vol. 19**, pp. 221-245, (1964).
17. J. T. Lin and G. J. Binder, "Simulation of mountain lee waves in a wind tunnel," College of Engineering, Colorado State University, *Rep. No.* CER67-88JTL-6JB24, (1967).
18. R. S. Scotti, "An experimental study of a stratified free shear layer," College of Engineering, University of California, Berkerly, *Rep. No.* AS-69-1 (1969).

19. R. S. Scotti and G. M. Corcos, "An experiment on the stability of small disturbances in a stratified free shear layer," *Journal of Fluid Mechanics*, **Vol. 52, part 3**, pp. 499-528, (1972).
20. Y. H. Pao, "Measurements of internal waves and turbulence in two-dimensional stratified shear flows," *Boundary Layer Met*eorology, **Vol. 5**, pp. 177-193, (1973).
21. R. E. Lange, "Decay of turbulence in stratified salt water," Ph.D. thesis, University of California, San Diego, (1974).
22. T. D. Dickey and G. L. Mellor, "Decaying turbulence in neutral and stratified fluids," *Journal of Fluid Mechanics,* **Vol. 99, part 1**, pp. 13-31, (1980).
23. D. C. Stillinger, M. J. Head, K. N. Helland and C. W. Van Atta, "A close-loop gravity-driven water channel for density-stratified shear flows," *Journal of Fluid Mechanics*, **Vol. 131**, pp. 73-89, (1983).
24. H. P. Grobelbauer, T. K. Fannelop and R. E. Britter, "The propagation of intrusion fronts of high density ratios," *Journal of Fluid Mechanics*, **Vol. 250**, pp. 669-687, (1993).
25. D. Barnea and Y. Taitel, "Kelvin-Helmholtz stability criteria for stratified flow: viscous versus non-viscous (inviscid) approaches," *Int. J. Multiphase flow*, **Vol. 19, No. 4,** pp. 639-649, (1993).
26. C. Hartel, E. Meiburg and F. Necker, "Analysis and direct numerical simulation of the flow at a gravity-current head. Part 1 Flow topology and front speed for slip and no-slip boundaries," *Journal of Fluid Mechanics*, **Vol. 418**, pp. 189-212, (2000).
27. J. O. Shin, S. B. Dalziel, and P. F. Linden, "Gravity currents produced by lock

exchange," *Journal of Fluid Mechanics,* **Vol. 521**, pp. 1–34. (2004).

28. H.Y. Gu and L.J. Guo,"Stability of stratified gas-liquid flow in horizontal and near horizontal pipes," *Chin. J. Eng.*, **Vol. 15(5),** pp. 619-625, (2007).
29. D. D. Stretch, J. W. Rottman, S. K. Venayagamoorthy, K. K. Nomura, and C. R. Rehmann, "Mixing efficiency in decaying stably stratified turbulence," *Dynamics of Atmospheres and Oceans*, **Vol. 49 (1)**, pp. 25-36, (2010).
30. R. J. Lowe, J. W. Rottman and P. F. Linden, "The non-Boussinesq lock-exchange problem. Part 1. Theory and experiments," *Journal of Fluid Mechanics*, **Vol. 537**, pp. 101-124, (2005).
31. V. K. Birman, J. E. Martin and E. Meiburg, "The non-Boussinesq lock-exchange problem. Part 2. High-resolution simulations," *Journal of Fluid Mechanics*, **Vol. 537**, pp. 125-144, (2005).
32. C. H. Oh, R. L. Moore, B. J. Merrill, and D. A. Petti, "Air ingress analyses on a high temperature gas-cooled reactor," INEEL/CON-01-00581, Nov. (2001).
33. C. H. Oh, E. S. Kim, H. S. Kang, H. C. NO, and N. Z. Cho, "Experimental Validation of Stratified Flow Phenomena, Graphite Oxidation, and Mitigation Strategies of Air Ingress Accidents," INL/EXT-08-14840, Idaho National Laboratory, U.S., Dec. (2009).
34. IAEA, "Heat transport and afterheat removal for gas cooled reactors under accident conditions," IAEA-TECDOC-1163, (2000).
35. C. H. Oh, C. Davis, L. Siefken, R. Moore, H. NO, J. Kim, G. C. Park, J. Lee, and W. Martin, "Development of safety analysis codes and experimental validation for a

very high temperature gas-cooled reactor," Final Report, INL/EXT-06-01362, Idaho National Laboratory. U.S., (2006).

36. C. H. Oh and E. S. Kim, "Validations of CFD code for density-gradient driven air ingress stratified flow," ICONE 18, May (2008).
37. C. H. Oh and E. S. Kim, "Air ingress analysis: computational fluid dynamic models," IHTC14-23083, Aug. (2010).
38. GENERAL ATOMICS 1996, "Gas turbine-modular helium reactor (GT-MHR) Conceptual design description report," GA-A910720, Project (1996).
39. J. Hartley, "Double ended guillotine break in a prismatic block VHTR lower plenum air ingress scenario" MS thesis, Texas A&M University, (2011).
40. S.K. Chang, S. Kim, and C.H. Song, "OECD/NEA─KAERI rod bundle CFD benchmark exercise test," Proceeding of CFD4NRS-4 Workshop, Daejeon Republic of Korea, Sep. 10-12, (2012).
41. A. DeStordeur, "Drag coefficients for fuel element spacers," *Nucleonics* **Vol. 19 (6)**, pp. 74–79, (1961).
42. G. Melese and R. Katz, "Thermal and Flow Design of Helium-Cooled Reactors," American Nuclear Society, La Grange Park IL, (1984).
43. S.C. Yao, L.E. Hochreiter, W.J. Leech, "Heat transfer augmentation in rod bundles near grid spacers," *ASME*, **Vol. 104**, pp. 76-78, (1982).
44. K. Rehme, "Pressure Drop Correlation for Fuel Element Spacers," *Nuclear Technology*, **Vol. 17,** pp. 15-23, Jan. (1973).
45. K. Rehme, "Simple Method of Predicting Friction Factors of Turbulent Flow in

Non-circular Channels," *Int. J. Heat Mass Transfer*, **Vol. 16**, pp. 931-950, (1973).

46. K. Rehme, "Pressure drop of spacer grids in smooth and roughened rod bundles," *Nuclear Technology*, **Vol. 13**, pp. 314-317, (1977).
47. M. Schikorr, E. Bubelis, L. Mansani, and K. Litfin, "Propsal for pressure drop prediction for a fuel bundle with grid spacers using Rehme pressure drop correlations," *Nuclear Engineering and Design,* **Vol. 240**, pp. 1830-1842, (2010).
48. K. Ikeda, Y. Makino, M. Hoshi, "Single-phase CFD applicability for estimating fluid hot-spot locations in a 5 X 5 fuel rod bundle," *Nuclear Engineering and Design,* **Vol. 236**, pp. 1149-1154, (2006).
49. M. A. Navarro and A. A.C. Santos, "Evalutiona of a numeric procedure for flow simulation of a 5X5 PWR rod bundle with a mixing vane spacer," *Progress in Nuclear Energy,* **Vol. 53,** pp. 1190-1196, (2011).
50. C.M. Lee and Y.D. Choi, "Comparison of thermo-hydraulic performances of large scale vortex flow (LSVF) and small vortex flow (SSVF) mixing vanes in 17X17 nuclear rod bundle," *Nuclear Engineering and Design,* **Vol. 237**, pp. 2322-2331, (2007).
51. X.Z., Cui and K.Y. Kim, "Three-dimensional analysis of turbulent heat transfer and flow through mixing vane in a subchannel of nuclear reactor," *Journal of Nuclear Science and Technology* **Vol. 40**, pp. 719-724, (2003).
52. K.Y. Kim and J.W. Seo, "Shape optimization of a mixing vane in a subchannel of nuclear reactor," *Journal of Nuclear Science and Technology,* **Vol. 41**, pp. 641-644, (2004).

53. K. Y. Kim and J.W. Seo, “Numerical optimization for the design of a spacer grid with mixing vanes in a pressurized water reactor fuel assembly,” *Nuclear Technology,* **Vol. 149**, pp. 62-70, Jan. (2005).
54. T.H. Chun and D.S. Oh, “A pressure drop model for spacer grids with and without flow mixing vanes,” *Journal of Nuclear Science and Technology,* **Vol. 35**, pp. 508-510, (1998).
55. STAR-CCM+ USER GUIDE Version 5.02, CD-adapco, (2009).
56. ANSYS-CFX USER GUIDE Version 13.0, ANSYS Inc., (2010).
57. ANSYS-FLUENT GUIDE Version 13.0, ANSYS Inc., (2010).
58. MATLAB USER GUIDE Version 7.11.0, (R2010b).
59. D.T. Lee and A. Yamamoto, “Wavelet analysis: theory and applications,” *Hewlett-Packard Journal*, pp. 44-54, Dec. (1994).
60. E. Merzari, H. Ninokata, “Large Eddy Simulation and Proper Orthogonal Decomposition of the flow in Annular Channnels.” *Annual Report of the Earth Simulator Center*, **Chapter 3** (April 2007- March 2008).
61. R. J. Adrian, K. T. Christensen, Z.-C. Liu, “Analysis and interpretation of instantaneous turbulent velocity fields,” *Experiment in Fluids,* **Vol. 29**, pp. 275-290, (2000).
62. D. Hilberg, W. Lazik, and H.E. Fiedler, “The application of classical POD and snapshot POD in a turbulent shear layer with periodic structures,” *Applied Scientific Research*, **Vol. 53**, pp. 283-290, (1994).
63. S. B. Pope, “Turbulent Flows,” Cambridge University Press, Cambridge UK (2000).

64. M. Germano, “Turbulence: the filtering approach.” *Journal of Fluid Mechanics*, **Vol. 238**, pp. 325-336, (1992).

65. H.C. Wei, J. Hartley, and Y. A. Hassan, “CFD simulation of air-ingress problem following a double-ended guillotine break in GT-MHR,” American Nuclear Society, La Grange Park IL, (2011).

66. C. J. Roy, “Grid convergence error analysis for mixed-order numerical schemes,” *AIAA*, **Vol. 41, No. 4**, pp. 595-604, (2003).

67. P. J. Roache, “Verification and validation in computational science and engineering,” Hermosa, Albuquerque, NM, Aug. (1998).

68. AIAA, “Guide for the verification and validation of computational fluid dynamics simulations,” AIAA-G-077-1998, Reston VA, Jan. (1998).

69. L. F. Richardson, “The deferred approach to the limit,” *Transactions of the Royal Society of London*, *Series A*, **Vol. 226**, pp. 229–361, (1927).

70. P. J. Roache, “Perspective: A method for uniform reporting of grid refinement studies,” *Journal of Fluids Engineering*, **Vol. 116, No. 3,** pp. 405–413, (1994).